Thermodynamic properties of the actinide oxides solid solutions

A calorimetric study

Sorin-Octavian Vălu

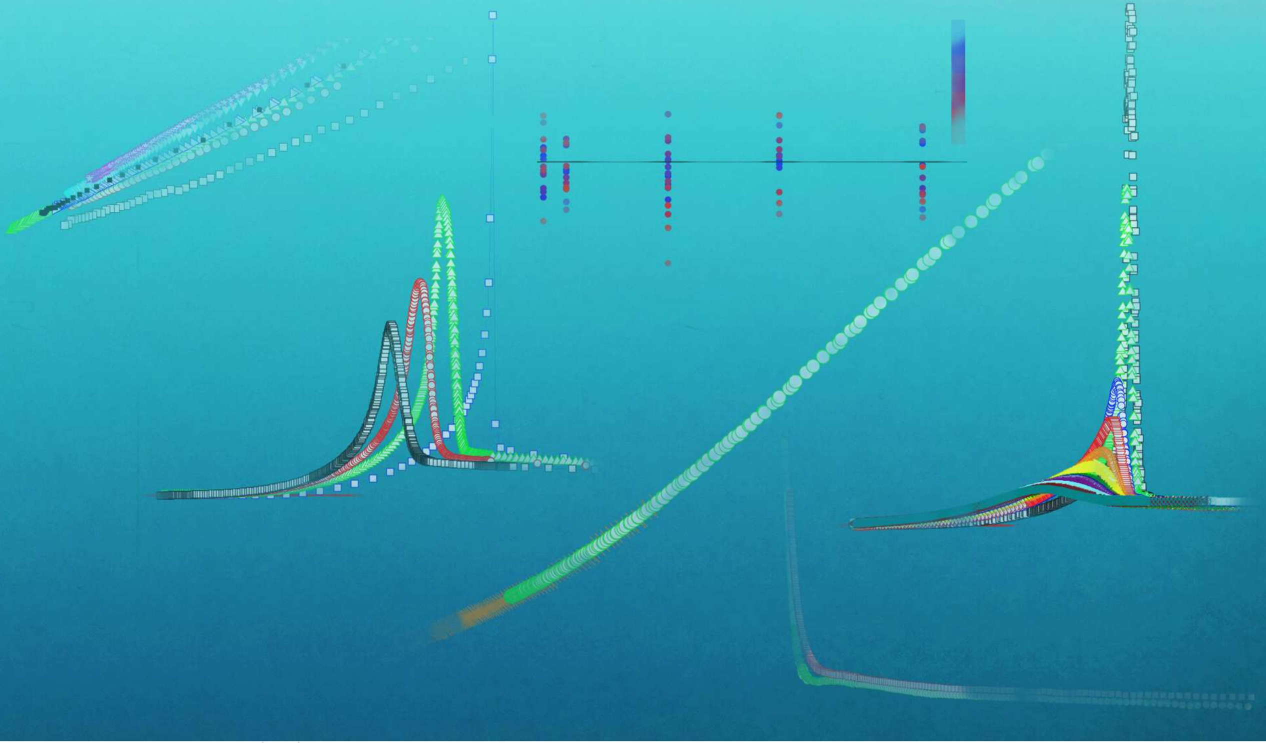

European Commission

TU Delft
Delft University of Technology

Thermodynamic properties of the actinide oxides solid solutions

A calorimetric study

Thermodynamic properties of the actinide oxides solid solutions

A calorimetric study

DISSERTATION

for the purpose of obtaining the degree of doctor
at Delft University of Technology
by the authority of the Rector Magnificus, prof.dr.ir. T.H.J.J. van der Hagen,
chair of the Board for Doctorates,
to be defended publicly on Tuesday, 9^{th} of June 2020 at 12:30

by

Sorin-Octavian VĂLU

MSc Chemistry
Alexandru Ioan Cuza University of Iași, Romania
born in Huși, Romania.

This dissertation has been approved by the promotors.

Prof. dr. R. J. M. Konings
Prof. dr. H. Th. Wolterbeek

Composition of the doctoral committee:

Rector Magnificus,	chairperson
Prof. dr. R. J. M. Konings	Delft University of Technology, promotor
Prof. dr. H. Th. Wolterbeek	Delft University of Technology, promotor
Independent members:	
Prof. dr. P. Dorenbos	Delft University of Technology
Prof. dr. ir. D. Sedmidubský	University of Chemistry and Technology Prague
Dr. C. Guéneau	CEA Saclay, Université Paris Saclay
Dr. A. L. Smith	Delft University of Technology
Dr. ir. A. G. Denkova,	Delft University of Technology
Prof. dr. ir. J. L. Kloosterman,	Delft University of Technology, reserve

Keywords: actinide oxides, enthalpy, heat capacity, calorimetry, thermal diffusivity, magnetic disorder

ISBN 978-94-6384-140-5

The work in this thesis was supported by European Commission in the frame of the program "Training and Mobility of Researchers". The research described in this thesis was performed within a cooperation of the Joint Research Centre Karlsruhe(JRC) of the European Commission, P.O. Box 2340, 76125 Karlsruhe, Germany and the Section Reactor Physics and Nuclear Materials (RPNM) of the Department Radiation Science and Technology, Faculty of Applied Sciences, Delft University of Technology, Melkeweg 15, 2629 JB Delft, The Netherlands. Their cooperation is hereby gratefully acknowledged.

Prediction is very difficult, especially if it's about the future.

Niels Bohr

Contents

1

Introduction

1.1. Nuclear Energy

The world energy consumption is estimated to grow by 28 % between 2015 and 2040 (figure 1.1) with about 2.3 % per year. Nuclear energy is known to be the second fastest-growing energy source, increasing by 1.5 % per year [1].

Since the end of the 20^{th} century, humanity has become aware of the environmental impact and potential long-term consequences of the combustion of fossil fuels for global climate change. Among the carbon-free energy resources, nuclear energy production will play an important role in supplying the necessary electricity for the next decades. Moreover, due to its small contribution to the greenhouse effect, nuclear power is a suitable alternative to fossil fuels for electricity production.

Nuclear energy originates from the splitting of heavy atomic nuclei of uranium and plutonium into two in a process called fission. In a power plant, the fission process is caused by absorption of a neutron and the released heat is used to produce steam, which drives a turbine to generate electricity. Besides heat, the process also releases neutrons, which cause further fissions, allowing a chain reaction to be sustained.

In October 1956 the first commercial nuclear power plant (Calder Hall) began its operation in England and turned attention to the peaceful use of nuclear fission. Since then, research and technological evolution have resulted in different generations and operational designs of nuclear reactors. Today, civil nuclear power supplies more than 10 % of global electricity needs and it is the world's second largest source of low-carbon power with 69 % pressurized water reactors (PWR) and 20 % boiling water reactors (BWR) [2].

In January 2020, 442 commercial reactors were in operation in 30 countries, 53 countries operated 220 civil research reactors. The energy produced by the commercial nuclear reactors is more than three times the total generating capacity of Germany from all sources. About 53 new nuclear power reactors were under construction, over 110 were firmly planned and there were 330 proposals for new reactors in the world [3, 4].

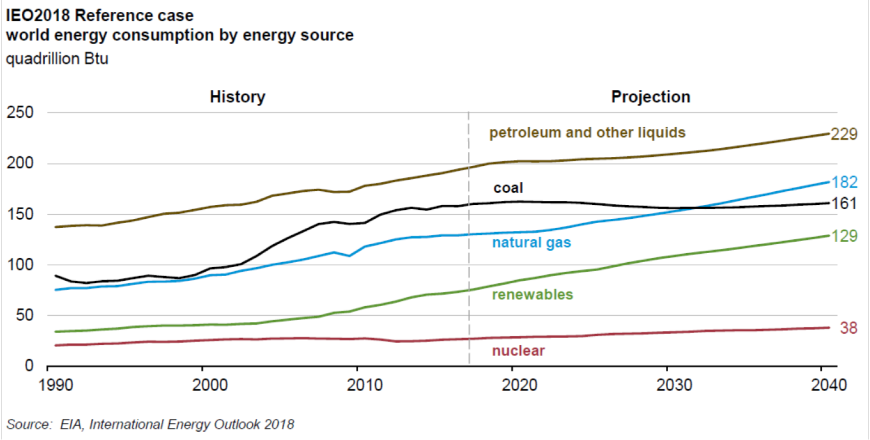

IEO2018 Reference case
world energy consumption by energy source
quadrillion Btu

Source: EIA, International Energy Outlook 2018

Figure 1.1: World total energy consumption, 1990-2040 (quadrillion British thermal units).

In 2018, twelve countries were relying on nuclear power for at least 25 % of their electricity. In France the electricity produced was about 75 % from nuclear source, in Hungary, Slovakia and the Ukraine the share was more than half, while in Belgium, Sweden, Slovenia, Bulgaria, Switzerland, Finland, the Czech Republic and South Korea it was 30 % or more. Beside these, other countries like the USA, the UK, Spain, Romania and Russia rely on nuclear energy production for about 20 % and among countries which do not host nuclear power plants, Italy and Denmark cover almost 10 % of their domestic consumption with imported nuclear power [2].

Because nuclear fission is the most efficient way of producing energy [XX] and nuclear power plants are designed to run long time before refueling, with less maintenance, this technology is a reliable source for the continuous increase of electricity demand. Although nuclear reactors have a good safety record, some concerns make nuclear technology difficult for full public acceptance. The two major fears associated with the civil use of nuclear energy are related to the safety of intermediate and long-term disposal of the radioactive waste and the safe operation of nuclear installations. Particularly, the possible dispersion of radioactive material in the environment during operation, accidents or disposal causes uncertainty regarding the public attitude towards nuclear power.

The most important source of the radioactive material is the fuel which once burned in the reactor can provide a source for radiological events and hazards. Fission products in spent nuclear fuel represent just 3 % of the total volume of waste arising from nuclear generation, but account for 95 % of its radiotoxicity. In addition, spent fuel contains transuranium elements such as Pu, Am and Np, which strongly contribute to the long term radiotoxicity. Solving the waste storage issue could significantly increase support for nuclear energy.

The present work is aimed at providing new experimental results on the behavior of different nuclear fuels from a thermodynamic point of view.

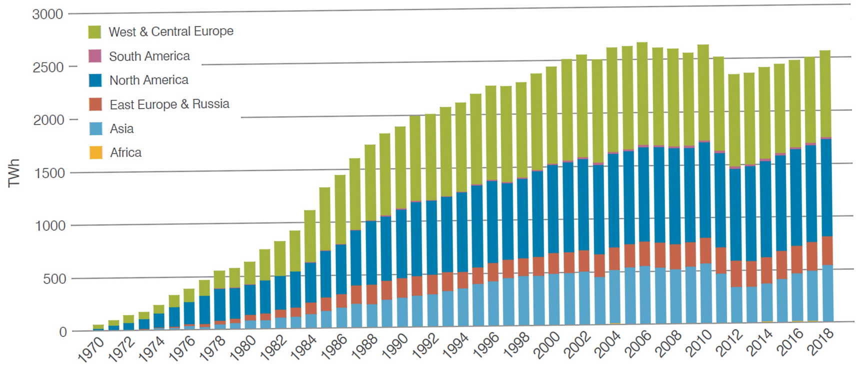

Source: World Nuclear Association and IAEA Power Reactor Information Service (PRIS)

Figure 1.2: Nuclear electricity production worldwide.

1.2. Mixed oxide fuels

Mixed oxide fuel, or MOX fuel, is a combination of the oxides of reprocessed plutonium and natural uranium, reprocessed uranium, or depleted uranium. It can replace the low enriched uranium feed for which most nuclear fission reactors were designed. MOX fuel releases energy from the fission of Pu-239, as well as the U-235 found in uranium fuel. As in UO_2 fuel, also in MOX Pu-239 is created from U-238 in the fuel via nuclear reactions. The balance between consumption and creation of Pu-239 depends on the reactor and fuel type. The use of MOX fuel has two major advantages: to extract energy from plutonium and management of separated plutonium stocks.

In 1962 the first PWR outside the United States came into operation in Belgium and one year later, its BR3 unit became the first thermal reactor to use MOX fuel. Progress with MOX fuel continued and in the 1980s it turned into commercial use. Since then, more than 2000 tonnes of MOX fuel have been assembled and loaded into 44 nuclear reactors (mostly PWR) [5]. Today MOX fuel is producing energy mainly in Europe and Japan and represents about 5 % of the new nuclear fuel worldwide. In Europe there are about 30 reactors in use (Netherlands, Belgium, Switzerland, Germany and France) while another 10 are licensed for MOX. Japan confirmed that 16 out of the 18 nuclear reactors use MOX fuel and in January 2020 Russia began the commercial use of MOX at Beloyarsk. Since these reactors generally use MOX fuel for about one third of their core and this fraction can be increased up to 50 %, other nations like the United Kingdom and China consider that MOX fuel could be an option for recycling their plutonium from spent fuel and using it to produce new MOX fuel [6].

Generally the use of MOX fuel in LWR does not significantly change the parameters of reactor operation. MOX fuel may, however, have some influence on reactor kinetics, reactivity behavior and the fuel-clad interactions in normal operation [7]. By adequate design of the fuel elements and by suitable distribution of MOX fuel elements in the core these effects can be taken into account so that no adverse effects result on reactor control and operation.

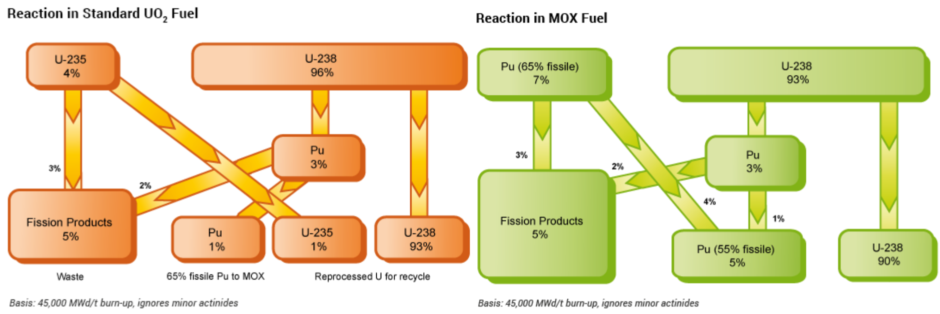

Figure 1.3: UO_2 fuel cycle and MOX fuel cycle.

Moreover, in 2018 the first EPR (European/Evolutionary Pressurised Reactor) was inaugurated in China (Taishan) and in September 2019 the second unit entered into commercial operation. It was expected that by the end of 2019 another 2 countries, France and Finland, would deliver electricity using this reactor-type but due to further system tests and unexpected additional costs both reactors are delayed to 2021 and 2023, respectively [8, 9]. Another 2 units are expected to go into operation in the United Kingdom by 2026 [10]. The EPR is a third-generation nuclear reactor developed by Framatom (formerly Areva) designed to use MOX fuel in 50 % to 100 % of the fuel assemblies [22].

1.3. Thorium fuel

The use of thorium in a nuclear reactor, as a prime energy source, has been in discussion for about half a century, while research continued to be focused on uranium or uranium-plutonium fuels. Giving its attractive benefits, thorium has been reconsidered in recent years and irradiation of various thorium-based fuels has been successfully conducted [23].

Thorium resources are estimated to be about 3 times more abundant than uranium, it provides an alternative of possible nuclear fuel supply with lower amounts of transuranic elements in the waste. Additionally, the use of thorium in most reactor types increases the safety margins so it offers attractive features.

As demonstrated [19–21], the use of thorium-based fuels has already been tested to generate electricity in several reactor types. These early trials were able to use highly-enriched uranium (HEU) as the fissile "driver" component, something that is not considered anymore given the available technology.

Thorium-plutonium mixed oxide is one of the options with the potential advantages of low development cost and high stability as a final waste form. Thorium oxide incorporating about 10 % of finely blended plutonium oxide as a "fissile driver" can be formed in the shape of dense ceramic pellets. The fabrication process is similar to the one of uranium mixed oxide fuels but the thorium-MOX fuel has additional advantages for some nuclear reactor types. The higher thermal conductivity and melting point support larger operating safety margins with no production of new plutonium. Therefore, thorium-plutonium MOX fuels provide an option for reducing civil and military plutonium stocks [24–27].

In-pile performance of $(Th,Pu)O_2$ fuel was evaluated by Somers *et al.* [28] with fuel pellets that were irradiated during four reactor cycles in a PWR at Obrigheim, Germany. The study concluded that the fuel behaviour was at least as good as U-MOX.

Thorium fuel has been tested also in *The Halden Reactor Project*, a test program that was carried out in a research reactor in Norway [11]. The goal of the project was to simulate how such fuel type would operate in a power reactor. The fuel was loaded in April 2013, a second batch in December 2015 and in January 2018 a third round with three new fuel pins was added. Eight pellets for this experiment were made by the European Commission's JRC Karlsruhe in Germany. The irradiation experiment was planned to continue for another five years after which the test results and irradiated fuel would be studied for quantifying the operational performance towards commercializing thorium as a nuclear fuel. Yet, in 2018 it was decided to stop the operation of the Halden Reactor and start its decommissioning [29].

1.4. Transmutation fuel

The high-level waste of reprocessed nuclear fuel contains significant amounts of americium and neptunium. Recycling of these two elements would be possible in the fuel of fast reactors as these transuranium elements can be transformed and fissioned into shorter-lived fission products. Additionally, their inclusion in the fuel would improve the efficiency and reduce the long-term hazard.

This is generally referred to as partitioning and transmutation (P&T). The time during which the waste remains hazardous can be considerably reduced if in addition to the plutonium also minor actinides are removed from the spent fuel and recycled [12]. The long term impact of P&T on nuclear waste could become significant and extensive when the application of a P&T cycle reaches the industrial scale.

The goal of partitioning is the separation of the minor actinides (MA's) from spent nuclear fuel. This separation can be achieved either by a hydro process or by a pyrochemical process [13].

- *Aqueous (hydrometallurgical) partitioning* refers to the process of separation and purification of the materials of interest by solubilisation and extraction from the spent fuel. Such mechanism can start from PUREX (Plutonium and Uranium Refining by Extraction) reprocessing and be adapted to the needs for other actinides, e.g. americium, neptunium and curium.
- *Pyrochemical partitioning* associates all activities that involve high-temperature treatments. This process does not use aqueous solvents but molten salts, liquid metals or gases instead. The spent fuel is treated by appropriate methods (e.g. electrorefining and electrolytic treatments) and run through several stages ending with the recovery of fissile material and separation of MA from fission products.

The term *transmutation* describes the transformation process of long-lived actinides into relatively short-lived fission products by absorption of neutrons followed by decay or a fission reaction. Depending on the fuel cycle and partitioning scenario, different types of reactors must be considered for transmutation purposes.

A large variety of different solid fuel types, with a wide range of chemical constituents, are considered for transmutation. Current studies are mainly focused on fuels that include oxide, carbide, nitride and metallic matrices. From the reactor physics point of view, the MA content of the standard fast reactor (FR) fuel can be increased to 2.5 % neptunium or americium without a major impact on reactor safety [14]. In addition transmutation of high-MA content targets in the blanket of FR is considered.

Mixed oxide fuel is also considered for management of americium from spent fuel. Incorporation of small quantities of americium (up to 5 %) in uranium-plutonium mixed oxide fuel could be used for energy production, or larger amounts in americium bearing blankets ($(U,Am)O_{2-x}$) dedicated to transmutation in fast neutron reactors. In this way significant amounts of americium could be recycled in the perspective of its long term environmental impact. Americium 241 and 243 are long-lived isotopes of the nuclear waste which can be separated from the spent fuel and then fissioned in order to produce short-lived fission products.

Currently, uranium and plutonium are commercially separated through the use of aqueous process, PUREX. While pyroprocessing is still very much at the research and development stage it can offer a promising way for treatment of very strongly irradiated spent fuel. Before transmutation can be introduced on an industrial scale, new fuels or targets will have to be developed that may contain substantial amounts of MA's and be able to withstand high levels of irradiation.

1.5. Fuel behaviour

During irradiation the fuel material suffers significant structural modifications and strong thermal stress due to the high temperatures and the strong temperature gradients. Investigations of the thermophysical properties of mixed oxide fuels are very important for predicting the possible behaviour under normal operational as well as accidental conditions. Experiments on laboratory scale for this type of compounds will allow for further physical models to be developed and to simulate the behaviour on industrial scale before being tested. Thermal conductivity, thermal diffusivity and heat capacity of a nuclear fuel are important because together with the melting temperature they define the margin-to-melting, i.e. the difference between the operating temperature and the temperature at which the first liquid is formed. The normal operating temperature at the center of the fuel in a LWR is around 1500 K, whereas its melting temperature is around 3100 K, resulting in a substantial margin. However, during reactor transients, the temperature can quickly rise. In order to predict the thermal response of the fuel, its properties thus need to be known accurately in a wide temperature range.

1.6. Objective

The goal of this thesis is to understand how the thermodynamic properties such as enthalpy, heat capacity and thermal conductivity of mixed actinide oxide solid solutions depend on crystal chemistry (composition, defect structure) in a wide range of temperatures. Since some of the actinides studied are highly radioactive materials, also the effect of damage by alpha self-radiation has to be taken into account. Emphasis is on the question whether these solutions show deviations from ideal behaviour due to the effects of lattice strain resulting from substitution of isovalent cations of different sizes and defects created by temperature or radiation.

1.7. Thesis outline

The implementation of this project involved detailed investigations of the thermal behavior of materials employed in nuclear fuel. The systems studied for this thesis are binary mixed oxides of the actinide elements (Th,Pu)O_2, (U,Pu)O_2, (Th,U)O_2, (U,Am)O_2. Thermodynamic studies of the actinide oxides and their solid solutions have been performed on low- and high-temperature regimes using different calorimeter types.

This is a topic for which just few experimental data are available or none, due to the many experimental challenges presented by the measurements. In the present investigations, great importance was given to the influence of radiation effects, stoichiometry and oxygen potential on heat treatment. The efficiency of the measuring devices was tested by measuring some end-members (UO_2, ThO_2, PuO_2) and their characteristics were compared with available literature data in the following chapters of this work.

The thesis is divided into eight chapters. The experimental work is presented in Chapters 2-7. Each chapter represents a systematic study of a binary system of actinide oxides and has already been published in a peer-reviewed journal.

The first chapter is dedicated to a short introduction into the nuclear energy, the different fuel-types that can produce energy, the necessity of studying mixed oxides and the importance attributed to their thermodynamic characteristics.

In Chapter 2 a set of experimental data was obtained for the (Th,Pu)O_2 system by measuring the enthalpy increments of five compositions using a drop calorimeter. The obtained experimental values are used to calculate the heat capacity of each individual mixture as a function of temperature. The absence of excess heat capacity of the intermediate compositions is reported in this chapter for the studied temperature interval.

Chapter 3 deals with the experimental investigation of two other mixed oxide systems. Heat capacity of compositions of the (Th,U)O_2 and (U,Pu)O_2 solid solutions were derived based on the experimental data obtained for the measured temperature interval. Our results are compared with available literature data and a good agreement is found. We extrapolate the results to the high temperature using a model that considers the effect of thermal defects and compare to literature and molecular dynamic calculation.

In Chapter 4 the high-temperature heat capacity, thermal diffusivity and thermal conductivity have been obtained for two intermediate compositions of mixed americium and uranium dioxide. This mixture has the big disadvantage of being very radioactive and is also oxygen sensitive, therefore this system had a lot of difficulties in creating the optimum conditions for performing accurate experiments. In agreement with the other oxide systems no substantial deviation from Neumann-Kopp's molar additivity rule has been found regarding the heat capacity whereas thermal diffusivity is strongly affected by the americium content in the mixture.

Continuing the heat capacity measurement series of mixed oxides, Chapter 5 deals with the low-temperature heat capacities of $(U_{1-y},Am_y)O_{2-x}$ solid solution for the two compositions introduced in chapter 4. Studies at low-temperature are likely to reveal more detailed information about the effects of lattice strain due to substitution. As observed for the $(Th,Pu)O_2$ system, the heat capacity results of the intermediate compositions presented in this section deviate also from the ideal trend imputed by the end members. Dealing with a strong α emitter such as americium 241, means that the sample will suffer self-damage. From the fact that the magnetic transition of U^{4+} order is completely absent, lattice disorder created by self-irradiation is considered to influence the final results.

Chapter 6 reports low-temperature heat capacity of the $(Th,Pu)O_2$ system and $^{239}PuO_2$ performed using the hybrid adiabatic relaxation method. In this system no magnetic ordering occurs. The obtained heat capacity of the $(Th,Pu)O_2$ system, over the temperature region 3.6 - 300 K, reveals significant deviations from Neumann-Kopp's molar additivity rule. The five compositions that were chosen for this study, showed a substantial excess in the heat capacity. These results combined with the one of the previous chapter offer a complete analysis of the variation of the heat capacity as a function of composition and temperature for the investigated system.

The low-temperature heat capacity of $(U_{1-y}Th_y)O_2$ and ^{238}Pu-doped UO_2 systems has been measured and discussed in chapter 7. The magnetic transition specific to UO_2 was evaluated as a tendency of thorium substitution ($y = 0.05, 0.09$ and 0.12) and the accumulation of radiation damage due to high alpha emission of ^{238}Pu isotope. With this work, in which a very complex thermodynamic study is published for the first time a clear distinction between the effect of lattice substitution and radiation defects could be made.

The most important findings and an overview of the whole project are summarized in the last chapter, chapter 8.

References

[1] International Energy Outlook 2018, July 2018. http://www.eia.gov/forecasts/ieo/.

[2] https://www.world-nuclear.org/information-library/current-and-future-generation/nuclear-power-in-the-world-today.aspx (January 2020)

[3] https://www.world-nuclear.org/information-library/facts-and-figures/world-nuclear-power-reactors-and-uranium-requireme.aspx (January 2020)

[4] https://nucleus.iaea.org/RRDB/RR/ReactorSearch.aspx

[5] https://www.world-nuclear.org/information-library/nuclear-fuel-cycle/fuel-recycling/mixed-oxide-fuel-mox.aspx (December 2019)

[6] https://www.orano.group/country/china/en/our-stories/mox-recycling-nuclear-energy (February 2020)

[7] Erich R. Merz, Carl E. Walter and Gennady M. Pshakin, Mixed Oxide Fuel (Mox) Exploitation and Destruction in Power Reactors, ISBN 0-7923-3473-6.

[8] https://world-nuclear-news.org/Articles/System-tests-further-delay-Finnish-EPR-start-up (February 2020)

[9] https://world-nuclear-news.org/Articles/EDF-warns-of-added-costs-of-Flamanville-EPR-weld-r (February 2020)

[10] https://en.wikipedia.org/wiki/Hinkley_Point_C_nuclear_power_station (February 2020)

[11] http://www.world-nuclear-news.org/ENF_Thorium_test_begins_2106131.html

[12] W.M. Stacey, Nuclear Reactor Physics, John Wiley & Sons, 2001.

[13] IAEA, Technical Reports Series No. 435, Implications of Partitioning and Transmutation in Radioactive Waste Management, 2004, STI/DOC/010/435 (ISBN:92-0-115104-7).

[14] T. Wakabayashi, K. Takahashi, T. Yanagisawa, Feasibility studies of plutonium and minor actinide burning in fast reactors, Nucl. Technol. 118 (1997) 14.

[15] http://www.westinghousenuclear.com/community/WhatIsNuclearEnergy.shtm

[16] http://www.world-nuclear.org/info/Current-and-Future-Generation/Nuclear-Power-in-the-World-Today/

[17] IAEA, Technical Reports Series No. 425, Country Nuclear Fuel Cycle Profiles, Second Edition, Vienna 2005.

[18] http://theenergylibrary.com/node/392

[19] K.P. Steward, Final Summary Report on the Peach Bottom End-of-Life Program, General Atomics Report GA-A14404, (1978).

[20] W.J. Babyak, L.B. Freeman, H.F. Raab, LWBR: A successful demonstration completed Nuclear News, Sept 1988, 114-116 (1988).

[21] J.C. Clayton, The Shippingport Pressurized Water Reactor and Light Water Breeder Reactor Westinghouse Bettis Atomic Power Laboratory WAPD-T-3007 (October 1993).

[22] J.G. Marques, "Environmental Characteristics of the Current Generation III Nuclear Power Plants" WIREs Energy Environ. 3, 195 (2014).

[23] Comprehensive Nuclear Materials, ISBN 978-0-08-056033-5, Vol. 3, (2012).

[24] INTERNATIONAL ATOMIC ENERGY AGENCY, Potential of Thorium Based Fuel Cycles to Constrain Plutonium and Reduce Long Lived Waste Toxicity, IAEA-TECDOC-1349, IAEA, Vienna (2003).

[25] Guillaume Martin, R. Girieud. Middle-term thorium strategy for PWR fleets. Energy Policy, Elsevier, 2016, 99, pp.147 - 153.

[26] http://www.world-nuclear.org/information-library/current-and-future-generation/thorium.aspx

[27] Chidambaram, R., and C. Ganguly. “Plutonium and Thorium in the Indian Nuclear Programme.” Current Science, vol. 70, no. 1, 1996, pp. 21–35. JSTOR, www.jstor.org/stable/24097470.

[28] https://doi.org/10.1016/j.jnucmat.2013.02.046

[29] https://www.world-nuclear-news.org/Articles/Halden-Reactor-to-be-decommissioned

2

The high temperature heat capacity of the (Th,Pu)O_2 system

The enthalpy increments of the $(Th_{1-y}, Pu_y)O_2$ solid solution with y= 0.03, 0.08, 0.30, 0.54 and 0.85 and the PuO_2 and ThO_2 end-members were measured using drop calorimetry in the temperature range 476-1790 K. The heat capacity was obtained by derivation of the obtained enthalpy data with respect to temperature. The presented results for PuO_2 and ThO_2 are compared with the available literature data whereas the results obtained for $(Th_{1-y},Pu_y)O_2$ solid solutions were compared with the Neumann-Kopp's molar additivity rule to search for possible non-ideal behaviour. This paper presents the first heat capacity data obtained for this system.

This chapter is reprinted with kind permission of Elsevier: *The high temperature heat capacity of the (Th,Pu)O_2 system. O.S. Vălu, O. Beneš, R.J.M. Konings, H. Hein. The Journal of Chemical Thermodynamics 68 (2014) 122-127.*

2.1. Introduction

Studies on oxides and mixed oxides of actinide elements such as thorium, uranium and plutonium are of great interest in nuclear industry since some of the oxides are used or are planned to be used as nuclear fuels in various types of reactors [1].

In the 1960s thorium mixed oxide was introduced as potential fertile material for fast and thermal reactors. It is known that thorium is about three times more abundant than uranium in the Earth's crust [2], thorium dioxide has the highest melting point of all oxides [3] and its thermal conductivity is higher than that of uranium dioxide [4]. Having huge resources of thorium and relatively little uranium, some countries are considering making utilization of thorium for large scale energy production a major goal in their nuclear power programme.

The use of thorium-based fuels offers attractive features, including lower levels of waste generation, lower production of transuranium elements per unit of fission energy and by using it in light water reactors (LWRs) as replacement for uranium, it provides an attractive option for nuclear fuel supply and nevertheless, it offers enormous energy security benefits in the long term.

^{232}Th is not a fissile nuclide, but it can be used as fertile material similar to ^{238}U. Neutron absorbtion by ^{232}Th produces ^{233}Th which decays by beta emission (with a half-life of about 22 minutes) to ^{233}Pa and by further beta decay (with a half-life of 27 days) ^{233}Pa decays to ^{233}U which is an excellent fissile fuel material. Thorium fuels therefore need an external start-up material and one of the options can be plutonium from reprocessing of LWR fuel.

(Th,Pu)O_2 can be used as fuel in pressurized water reactors (PWRs) without making any change in the reactor system and the fuel can be made using existing technology and licensing experience existing for uranium-MOX plants [5]. This type of fuel can be effectively used also to reduce or stabilize plutonium stockpiles because of the high plutonium consumption rate. It is therefore an important and potentially viable technology to contribute to building credible, safe and long term nuclear energy scenarios.

The thermodynamic properties such as enthalpy and heat capacity of these materials are needed for reactor safety calculations. In order to understand the behavior of the nuclear fuel during the irradiation it is mandatory to have clear information about the thermodynamic properties of the fuel material. The number of studies about (Th,Pu)O_2 is limited. The thermal diffusivity and conductivity of PuO_2 and ThO_2 as well as of the mixed oxide (Th,Pu)O_2 (with 3, 8 and 30 wt.% PuO_2) were investigated by Cozzo *et al.* [6]. Bakker *et al.* [7] have suggested a phase diagram (shown in figure 2.1) of the PuO_2 - ThO_2 pseudo-binary system based on the melting point measurements [8] of the ThO_2 - PuO_2 binary compositions and the results obtained by Freshley and Mattys [9] which suggested that ThO_2 and PuO_2 form an ideal solid solution for the whole composition range. Analyzing this phase diagram one can notice that the melting point measurements of the intermediate compositions are lower than the suggested solidus and liquidus line [7] and this may indicate that the ThO_2 - PuO_2 system does not behave ideal. According to some recent studies performed in ITU by De Bruycker *et al.* [10], the melting point of PuO_2 is even higher than those previously observed. Starting from these results, the experiments performed in this study were made to clarify if the ther-

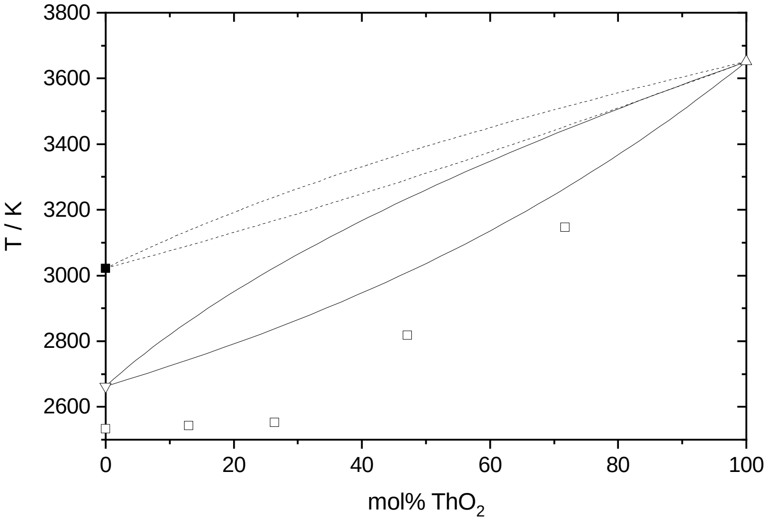

Figure 2.1: Phase diagram of ThO_2 - PuO_2. The solid lines shows the ideal behaviour after Bakker *et al.* [7] and dotted lines shows the ideal behaviour calculated taking into account the new melting point of PuO_2 measured in ITU by De Bruycker *et al.* [10]. □ melting points of $(Th_{1-y},Pu_y)O_2$ [8]; △ melting point of ThO_2 [3]; ▽ melting point of PuO_2 [18].

modynamic quantities of the ThO_2 - PuO_2 solid solution follow ideal behavior or if some excess contributions for enthalpy increments and heat capacity need to be considered.

2.2. Experimental work

2.2.1. Sample preparation

The $Th_{0.97}Pu_{0.03}O_2$, $Th_{0.92}Pu_{0.08}O_2$, $Th_{0.70}Pu_{0.30}O_2$, $Th_{0.46}Pu_{0.54}O_2$ and $Th_{0.15}Pu_{0.85}O_2$ samples used for the enthalpy increment measurements performed in this study were produced at ITU by the sol gel process. For this process the thorium nitrate and plutonium dioxide are dissolved in an acidic solution and, following analysis, are mixed in the appropriate amounts. The solution is mixed with polymers to increase the viscosity and is then dispersed using a rotating cup atomizer. The resulting droplets are collected in an ammonia bath, where a droplet to particle conversion occurs via a gelation process. Following ageing, the beads are washed in water and calcined before being compacted into pellets, which are then sintered at a suitable temperature and in an appropriate atmosphere to give the product pellets. More information about the sample preparation of the mixed oxides with PuO_2 concentrations of 3, 8 and 30 wt.% can be found in the study of Cozzo *et al.* [6], while the concentrations containing 54 and 85 wt.% PuO_2 were produced in a similar way.

2.2.2. Drop calorimeter

The enthalpy increment measurements performed in this study were made with a Setaram Multi Detector High Temperature Calorimeter (MDHTC -96 type) operated in drop mode and adapted for glove box use allowing handling of active samples as described in [11]. For more details about the design we refer to that study. The temperature scale of the calorimeter was calibrated using high purity (⩾ 99.95%) standard materials (In, Zn, Sn, Pb, Al, Ag and Au) with well determined melting points.

2.2.3. Experimental procedure

The samples are introduced in a sample holder, which is positioned on top of the detector. The furnace is programmed to reach the desired temperature at which the heat flow signal is stabilized in 7 hours. After this period the samples are dropped from ambient temperature (precisely measured) into the calorimeter which is programmed to maintain a constant temperature. Each drop is repeated every 25 minutes which has been found to be sufficient time to restabilize the temperature and the heat flow signals. Before and after each sample, a reference material is dropped to determine the sensitivity (signal vs heat ratio) of the detector. As reference material we used small pieces (150-200 mg) of platinum 99.995 %. The system records the energy which is necessary to heat up the sample from the room temperature to the programmed temperature. For all experiments, high purity helium gas was used as carrier gas with the flow rate of 2.8 l/h. Helium was selected for good thermal conductivity reasons.

The sensitivity (s) of the calorimeter is calculated from the heat exchange signal ($\int \phi_R d\tau$) of the standard material according to equation 2.1, where T_a and T_m are the ambient temperature and measured temperatures, m_R and M_R are the mass and the molar mass of the reference material, respectively and $C_{p,R}$(T) is the temperature function of its molar heat capacity.

$$s = \frac{\int \phi_R d\tau}{\int_{T_a}^{T_m} C_{P,R}(T) dT} \cdot \frac{M_R}{m_R} \tag{2.1}$$

The molar enthalpy increment of the measured samples corresponding to heating from ambient temperature to the measurement temperature is calculated according to equation 2.2. The $\int \phi_S d\tau$ term represents the time integral of the heat flow peak of the sample, the sensitivity (s) is taken as an average value of two references, dropped before and after the sample, and m_S and M_S are the reference material mass and molar mass, respectively.

$$\Delta_{T_a}^{T_m} H_m = \frac{\int \phi_S d\tau}{s} \cdot \frac{M_S}{m_S} \tag{2.2}$$

Figure 2.2 shows an example of a measurement sequence performed in this study, for the $Th_{0.92}Pu_{0.08}O_2$ composition, consisting of four drops of samples and five drops of the platinum reference. Each peak of the heat flow signal was integrated individually, obtaining $\int \phi_R d\tau$ and $\int \phi_S d\tau$ terms from equations 2.1 and 2.2.

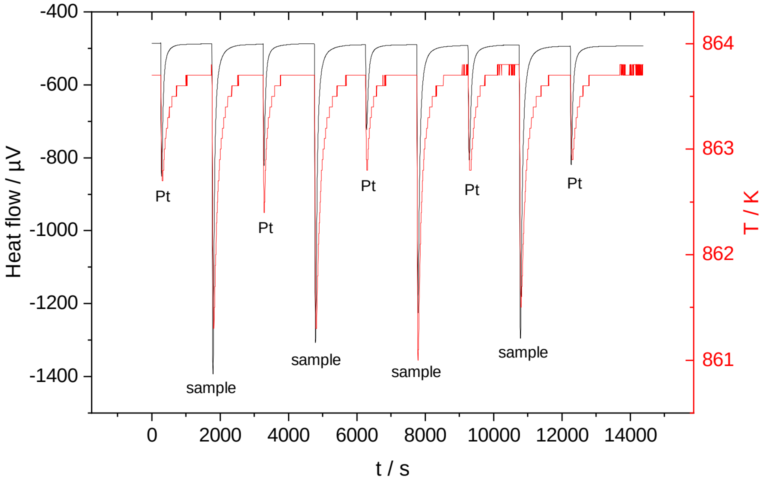

Figure 2.2: An example of measurement performed in this study using the drop calorimeter for the $Th_{0.92}Pu_{0.08}O_2$ composition. The red line is the temperature in the detector and the black line represents the heat flow signal.

Once the enthalpy as a function of temperature is obtained the heat capacity is calculated by derivation of the enthalpy function according to:

$$C_p = \left(\frac{\partial H}{\partial T}\right)_p \tag{2.3}$$

2.3. Results and Discussion

Non ideal heat capacity behavior could be expected from the excess contributions resulting from the lattice strain due to the difference in ionic radius of Pu^{4+} (100 pm) and Th^{4+} (108 pm). For the $(U,Pu)O_2$ system all literature sources present the heat capacity behavior of the intermediate compositions as being ideal, while Agarwal *et al.* [12] presented a comparison of the heat capacity values of solid solution for the $(Th_{1-y},U_y)O_2$ system with variation in the fraction of ThO_2 and showed that for $y < 0.20$ the heat capacity values calculated from their enthalpy increment data are lower than the heat capacity values obtained from Neumann-Kopp's additivity rule. They showed that the difference is increasing with increase in temperature. The same behavior was observed by Springer *et al.* [13] hence, if the lattice strain influences the excess heat capacity due to the difference in the ionic radius of U^{4+} (103 pm) and Th^{4+} (108 pm) then it can be expected that heat capacity of the $(Th_{1-y},Pu_y)O_2$ system should present a more pronounced lattice strain effect.

To investigate this, enthalpy increment measurements of $(Th_{1-y},Pu_y)O_2$ solid solutions with y= 0.03, 0.08, 0.30, 0.54 and 0.85 were performed in the temperature range 476 - 1790 K. In addition the ThO_2 and PuO_2 end-members were measured and compared with the literature data obtaining a good agreement. Measured enthalpy increments of ThO_2 and PuO_2 are given in table 2.1 and a comparison with literature data from [12] and [14], which were obtained on very large quantities (tens of grams), is shown in figure 2.3. The samples weight ranged between 52.2 mg - 145.9 mg for ThO_2 and 56.0 mg - 177.8 mg for PuO_2. Although much smaller amounts are used in this study the agreement and accuracy of the results with the above given references is very good, as well with the assessed values from [15].

Table 2.1: Measured enthalpy increments of the ThO_2 and PuO_2 solid solution and their standard deviations.

ThO_2			PuO_2		
T_m/K	H_{T_m} - $H_{(298.15)}$/(J · mol^{-1})	n	T_m/K	H_{T_m} - $H_{(298.15)}$/(J · mol^{-1})	n
475.9	12264 ± 187	3	578.9	22088 ± 1380	4
578.1	20745 ± 674	3	631.3	27525 ± 910	4
679.0	27252 ± 634	3	680.7	30142 ± 1123	4
779.8	33875 ± 854	3	731.1	33816 ± 1420	4
879.8	42692 ± 71	3	781.7	39422 ± 735	4
980.4	47668 ± 1976	3	831.5	43115 ± 2245	4
1081.0	57614 ± 2077	3	880.0	46097 ± 1102	4
1181.4	68795 ± 3520	3	980.1	58713 ± 4541	4
1282.0	73286 ± 2932	3	1081.1	67086 ± 11149	4
1382.6	84339 ± 2414	3	1181.1	79915 ± 4719	4
1432.9	84716 ± 1207	3	1283.6	84262 ± 7891	4
1533.6	92614 ± 3860	3	1382.4	99902 ± 15377	4
1685.3	105422 ± 10832	3	1483.3	102539 ± 6555	4
1736.1	111709 ± 9970	3	1532.9	111413 ± 22363	4
1786.6	113707 ± 6521	3	1584.1	114777 ± 6468	3
			1634.8	117877 ± 2927	4
			1685.3	125627 ± 2859	2
			1736.7	126243 ± 3400	4

The enthalpy increments of $Th_{0.97}Pu_{0.03}O_2$, $Th_{0.92}Pu_{0.08}O_2$, $Th_{0.70}Pu_{0.30}O_2$, $Th_{0.46}Pu_{0.54}O_2$ and $Th_{0.15}Pu_{0.85}O_2$ were measured on sample weights ranged between 70.5 mg - 170.2 mg, 72.1 mg - 145.5 mg, 23.9 mg - 62.0 mg, 59.9 mg - 166.9 mg and 73.1 mg - 112.4 mg, respectively. The measured enthalpy values are given in tables 2.2, 2.3 and 2.4 and shown in figure 2.4 together with the values estimated by Neumann-Kopp's rule. For each measured temperature the corresponding enthalpy value represents the mean of all performed measurements at that temperature. As can be seen, the enthalpy increment values for the five compositions increase with the PuO_2 content.

In order to check if the measured enthalpies reveal some excess contribution, all experimental values were compared with the ideal values obtained by linear interpolation of the values of the end-members. The comparison is shown in figure 2.5. The deviation from the "0" line of each individual value is in the range of maximum ± 5 kJ/mol, with smaller deviation at lower temperatures and increasing at higher temperatures where the experimental uncertainty is also higher. Having an almost symmetric distribution of $\triangle$ (H_{meas} - H_{NK}) values and an average deviation of ± 2%, which is smaller than the experimental uncertainty, we can conclude that there is no evidence for a lattice strain effect.

The heat capacity functions of the intermediate compositions of the (Th, Pu)O_2 solid solution were obtained using a simultaneous linear regression taking into account all measured enthalpy data and the low temperature heat capacity of

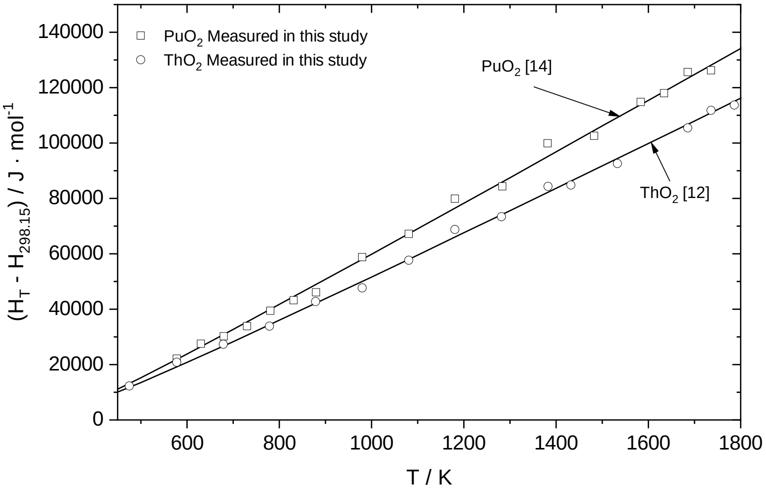

Figure 2.3: Comparison of measured enthalpy increments of ThO_2 and PuO_2 solid solution with literature data values from [12] and [14].

Table 2.2: Measured enthalpy increments of the $Th_{0.97}Pu_{0.03}O_2$ and $Th_{0.92}Pu_{0.08}O_2$ solid solutions and their standard deviations.

$Th_{0.97}Pu_{0.03}O_2$ composition			$Th_{0.92}Pu_{0.08}O_2$ composition		
T_m/K	H_{T_m} - $H_{(298.15)}$ / (J · mol^{-1})	n	T_m/K	H_{T_m} - $H_{(298.15)}$ / (J · mol^{-1})	n
580.2	19834 ± 1044	3	578.1	18891 ± 1001	4
630.5	22417 ± 701	4	679.2	26298 ± 1348	4
681.0	27093 ± 2005	4	880.1	43498 ± 1660	4
731.2	28399 ± 1108	4	980.5	47712 ± 1488	8
781.5	35459 ± 916	4	1081.0	57342 ± 1236	8
831.4	36409 ± 752	4	1180.1	67848 ± 1826	8
983.5	48481 ± 2159	4	1282.0	73323 ± 836	8
1083.4	60644 ± 6951	3	1382.4	79921 ± 1450	4
1179.6	64992 ± 3288	4	1483.4	92708 ± 3452	4
1282.4	73838 ± 6039	4	1583.5	99664 ± 2692	4
1381.5	83033 ± 10088	3	1685.1	106966 ± 5548	8
1482.1	92080 ± 3709	4	1787.0	115658 ± 10045	4
1585.9	98786 ± 6753	3			
1686.6	104006 ± 3285	4			
1788.7	119580 ± 6537	4			

Table 2.3: Measured enthalpy increments of the $Th_{0.70}Pu_{0.30}O_2$ solid solution and their standard deviations.

$Th_{0.70}Pu_{0.30}O_2$ composition		
T_m/K	H_{T_m} - $H_{(298.15)}$ / $(J \cdot mol^{-1})$	n
577.9	18992 ± 489	4
628.1	21296 ± 622	4
678.6	26900 ± 5228	4
728.2	29895 ± 2821	4
779.7	35826 ± 1291	4
830.3	39378 ± 2098	4
879.8	42936 ± 720	4
930.3	47058 ± 3863	3
980.1	51973 ± 739	4
1029.4	56493 ± 2064	4
1129.7	65720 ± 2342	4
1278.9	78596 ± 2317	2
1380.0	84467 ± 1303	4
1480.5	92820 ± 1572	4
1581.8	100014 ± 5365	4
1682.5	105812 ± 9017	4
1732.4	112584 ± 9954	4
1785.4	118829 ± 10411	5

Table 2.4: Measured enthalpy increments of the $Th_{0.46}Pu_{0.54}O_2$ and $Th_{0.15}Pu_{0.85}O_2$ solid solutions and their standard deviations.

$Th_{0.46}Pu_{0.54}O_2$ composition			$Th_{0.15}Pu_{0.85}O_2$ composition		
T_m/K	H_{T_m} - $H_{(298.15)}$ / $(J \cdot mol^{-1})$	n	T_m/K	H_{T_m} - $H_{(298.15)}$ / $(J \cdot mol^{-1})$	n
475.8	12440 ± 225	3	528.7	18408 ± 1424	3
577.8	20539 ± 369	3	579.9	21176 ± 1493	3
679.0	28979 ± 1415	3	681.4	31902 ± 5483	4
779.4	36406 ± 2043	3	782.0	35379 ± 1704	4
880.0	45599 ± 3531	3	882.3	48610 ± 3842	4
980.1	56060 ± 1477	3	983.3	54539 ± 4697	3
1080.9	65391 ± 3869	3	1084.0	64342 ± 3198	4
1181.0	71477 ± 1203	3	1184.9	76820 ± 6215	4
1281.4	81424 ± 2280	3	1286.1	86396 ± 5619	4
1381.9	89869 ± 2186	3	1387.3	91650 ± 4468	4
1482.4	94820 ± 2662	3	1490.2	99948 ± 5502	4
1583.0	105509 ± 10391	3	1591.7	111284 ± 15041	4
1685.2	114314 ± 3387	3	1693.0	123087 ± 12435	4
1786.3	129506 ± 3332	3	1743.7	125848 ± 4593	4

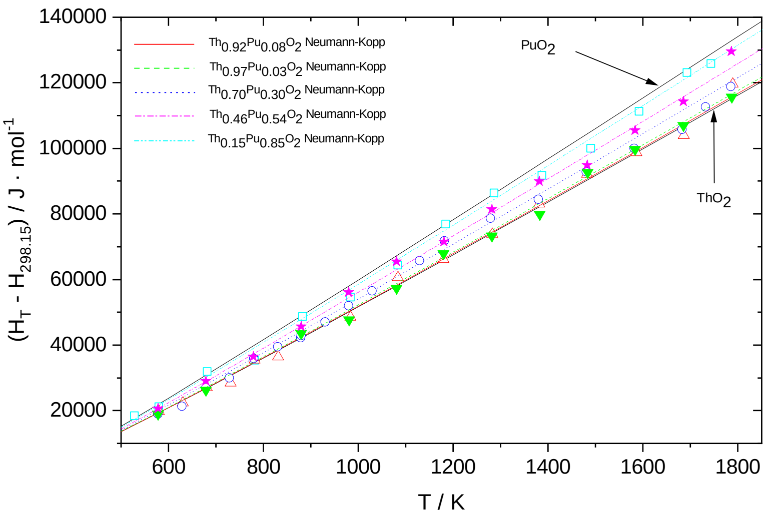

Figure 2.4: The enthalpy increments of the (Th, Pu)O_2 system measured in this study. △ $Th_{0.97}Pu_{0.03}O_2$, ▼ $Th_{0.92}Pu_{0.08}O_2$, ○ $Th_{0.70}Pu_{0.30}O_2$, ★ $Th_{0.46}Pu_{0.54}O_2$ and □ $Th_{0.15}Pu_{0.85}O_2$

.

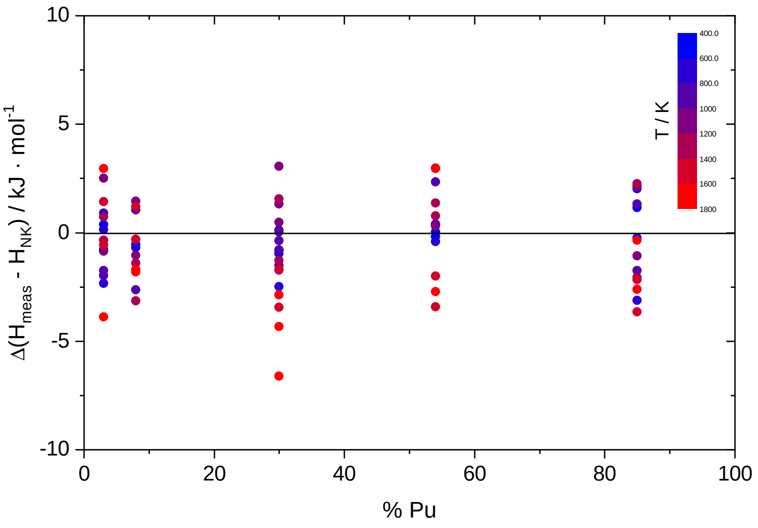

Figure 2.5: $\triangle(H_{meas}$ - $H_{NK})$ values obtained for all five compositions for the specific temperature range.

the intermediate compositions estimated using the Neumann-Kopp's rule and the experimentally obtained heat capacity of the end members measured by Sandenaw [16] and Osborne [17]. A constraint at 298.15 K corresponding to a value of 61.89 J·K^{-1} ·mol^{-1}, 62.12 J·K^{-1}·mol^{-1}, 63.11 J·K^{-1}·mol^{-1}, 64.18 J·K^{-1}·mol^{-1} and 65.58 J·K^{-1}·mol^{-1} for the compositions $Th_{0.97}Pu_{0.03}O_2$, $Th_{0.92}Pu_{0.08}O_2$, $Th_{0.70}Pu_{0.30}O_2$, $Th_{0.46}Pu_{0.54}O_2$ and $Th_{0.15}Pu_{0.85}O_2$, respectively, has been applied. Using a second order Maier-Kelly type polynomial equation, the high temperature heat capacity of the intermediate compositions was described:

$$C_{p,m}/(J \cdot K^{-1} \cdot mol^{-1}) = A + B \cdot (T/K) + C \cdot (T/K)^{-2} \tag{2.4}$$

The values of the constants of the equations obtained for the heat capacity of all measured intermediate (Th,Pu)O$_2$ compositions as well as for PuO$_2$ and ThO$_2$ are given in table 2.5. Temperature variation of the obtained heat capacities are shown in figure 2.6 together with the inset graphs corresponding to $\triangle$(C$_{P,m}$ - C$_{P,NK}$) of each of the intermediate composition.

As explained above, in order to fit the heat capacity values we had to constrain our results to a constant value for each individual composition at T= 298.15 K. Due to this approximation it can be observed that in the $\triangle$(C$_{P,m}$ - C$_{P,NK}$) inset graphs the "0" value corresponds to T= 298.15 K. The results of the thus obtained heat capacity curves indicate that $Th_{0.97}Pu_{0.03}O_2$, $Th_{0.92}Pu_{0.08}O_2$, $Th_{0.70}Pu_{0.30}O_2$ and $Th_{0.15}Pu_{0.85}O_2$ solid solutions lie slightly below the heat capacity computed using Neumann-Kopp's rule and some negative excess heat capacity may appear, while for the $Th_{0.46}Pu_{0.54}O_2$ composition almost perfect match is observed. However, taking into account that our measurements are affected by the experimental uncertainties represented in our graphs as confidence bands and that the heat capacity is not measured direct but obtained by derivation of the enthalpy, we conclude that the obtained heat capacity of the (Th$_{1-y}$,Pu$_y$)O$_2$ solid solution (with y= 0.03, 0.08, 0.30, 0.54 and 0.85) obey the molar additivity rule for the temperature range 476 - 1790 K.

Table 2.5: Constants for the fit equations of the high temperature heat capacity $C_{p,m}/(J \cdot K^{-1} \cdot mol^{-1}) = A + B \cdot (T/K) + C \cdot (T/K)^{-2}$

Solid solution	A	B ·10^{-3}	C ·10^4
ThO$_2$	71.492 ± 4.324	8.0241 ± 5.092	-107.7745 ± 26.0444
$Th_{0.97}Pu_{0.03}O_2$	67.506 ± 8.283	9.9553 ± 8.991	-76.3096 ± 50.5361
$Th_{0.92}Pu_{0.08}O_2$	69.148 ± 11.726	10.2417 ± 12.47	-89.6212 ± 71.4471
$Th_{0.70}Pu_{0.30}O_2$	69.798 ± 7.971	11.9936 ± 8.764	-91.2389 ± 48.4318
$Th_{0.46}Pu_{0.54}O_2$	78.681 ± 6.478	9.2529 ± 7.021	-153.4243 ± 39.5948
$Th_{0.15}Pu_{0.85}O_2$	77.042 ± 13.029	12.945 ± 13.463	-136.2292 ± 81.0658
PuO$_2$	81.948 ± 5.965	11.956 ± 6.804	-171.2313 ± 35.9692

2.4. Summary

As mentioned in the previous sections there are no literature data for the high temperature heat capacity of the (Th,Pu)O$_2$ system. For this reason all our results were val-

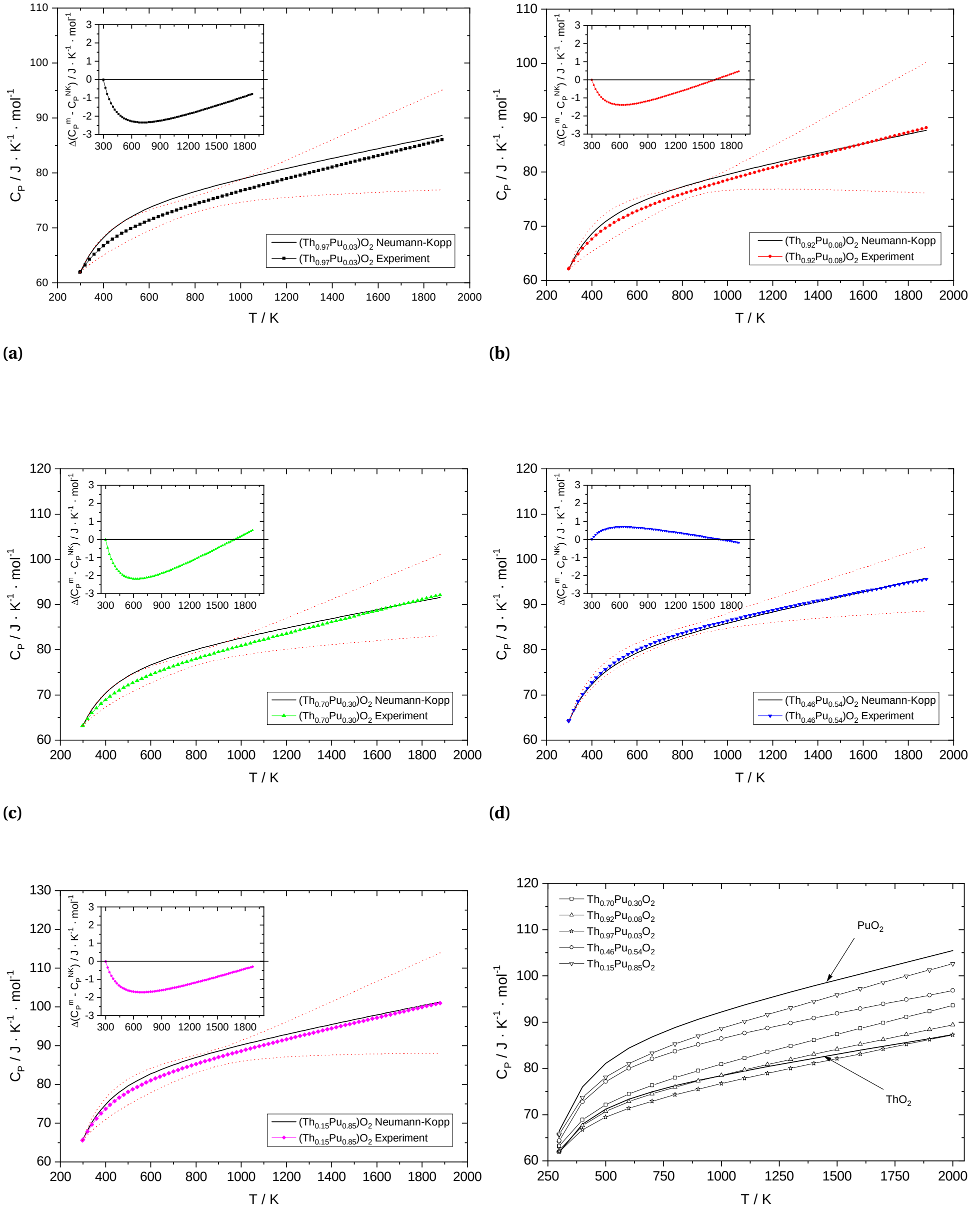

(a)

(b)

(c)

(d)

(e)

(f)

Figure 2.6: Heat capacity functions of the intermediate compositions $Th_{0.97}Pu_{0.03}O_2$, $Th_{0.92}Pu_{0.08}O_2$, $Th_{0.70}Pu_{0.30}O_2$, $Th_{0.46}Pu_{0.54}O_2$ and $Th_{0.15}Pu_{0.85}O_2$ derived from the enthalpy increments obtained by drop calorimetry, plotted together with their confidence bands and computed N-K functions (a-e) and the heat capacity of the ThO_2 and PuO_2 end-members (f).

idated by referring to the thermodynamic properties of the end members, which were very well determined, and to the Neumann-Kopp's molar additivity rule.

The enthalpy increments of the ThO_2 and PuO_2 end-members and (Th,Pu)O_2 solid solutions with 3, 8, 30, 54 and 85 wt.% PuO_2 were measured by drop calorimetry and from these data the heat capacity was derived. The enthalpy increments of ThO_2 and PuO_2 obtained in this study are in good agreement with available literature data. Having these as a proof that our set-up is efficient in obtaining reliable data, with samples of 50 - 200 mg size, we performed enthalpy increment measurements for the intermediate compositions of the system. From the results we conclude that with respect to the experimental uncertainly, the obtained enthalpy and heat capacity obey the molar additivity rule for the temperature range 476-1790 K.

References

[1] C. Ganguly, Development of plutonium-based advanced LMFBR fuels and thoria-based PHWR fuels in India, IAEA-TECDOC 352, (1985) 107-127.

[2] D.R. Lide, Handbook of Chemistry and Physics (86th version), CRC Press Inc., 2005.

[3] C. Ronchi, J.P. Hiernaut, J. Alloy. Compd. 240 (1996) 179-185.

[4] J. Belle, R.M. Berman, Thorium dioxide: properties and nuclear applications, Technical Report DOE/NE-0060, Naval reactors Office, United States Department of Energy, 1984.

[5] Thorium-based nuclear fuel: current status and perspectives, TECDOC-412, IAEA, 1987.

[6] C. Cozzo, D. Staicu, J. Somers, A. Fernandez, R.J.M. Konings, J. Nucl. Mater. 416 (2011) 135-141.

[7] K. Bakker, E.H.P. Cordfunke, R.J.M. Konings, R.P.C. Schram, J. Nucl. Mater. 250 (1997) 1-12.

[8] HW-76300, Quarterly report Ceramics research and development operation, General Electric, 1962.

[9] M.D. Freshley, H.M. Mattys, General Electric Report HW-76449, 1962, p. 11.6.

[10] F. De Bruycker, K. Boboridis, P. Pöml, R. Eloirdi, R.J.M. Konings, D. Manara, J. Nucl. Mater. 416 (2011) 166-172.

[11] O. Beneš, P. Gotcu-Freis, F. Schwörer, R.J.M. Konings, Th. Fanghänel, J. Chem. Thermodynamics 43 (2011) 651-655.

[12] R. Agarwal, R. Prasad, V. Venugopal, J. Nucl. Mater. 322 (2003) 98-110.

[13] J.R. Springer, E.A. Eldridge, N.U. Goodyear, T.R. Wright, J.F. Lagedrox, BMI-X-10210, October 1967.

[14] O.L. Kruger and H. Savage, J. Chem. Phys. 49, 10 (1968) 4540-4544.

[15] R.J.M. Konings, O. Beneš, A. Kovács, D. Manara, D. Sedmidubský, L. Gorokhov, V.S. Iorish, V. Yungman, E. Shenyavskayan and E. Osina, The thermodynamic properties of the f-elements and their compounds. Part II. The Lanthanide and Actinide Oxides, J. Phys. Chem. Ref. Data, 43 (2014)013101.

[16] Th.A. Sandenaw, J. Nucl. Mater. 10, 3 (1963) 165-172.

[17] D.W. Osborne and E.F. Westrum, J. Chem. Phys. 21, 10 (1953) 1884-1887.

[18] E.H.P. Cordfunke, R.J.M. Konings, Thermochemical Data for Reactor Materials and Fission Products, Elsevier, Amsterdam, 1990.

3

The high-temperature heat capacity of the (Th,U)O_2 and (U,Pu)O_2 solid solutions

The enthalpy increment data for the (Th,U)O_2 and (U,Pu)O_2 solid solutions are reviewed and complemented with new experimental data (400-1773 K) and many-body potential model simulations. The results of the review show that from room temperature up to about 2000 K the enthalpy data are in agreement with the additivity rule (Neumann-Kopp) in the whole composition range. Above 2000 K the effect of Oxygen Frenkel Pair (OFP) formation leads to an excess enthalpy (heat capacity) that is modeled using the enthalpy and entropy of OFP formation from the end-members. A good agreement with existing experimental work is observed, and a reasonable agreement with the results of the many-body potential model, which indicate the presence of the diffuse Bredig (superionic) transition that is not found in the experimental enthalpy increment data.

This chapter is reprinted with kind permission of Elsevier: *The high-temperature heat capacity of the (Th,U)O_2 and (U,Pu)O_2 solid solutions. O.S. Vălu, O. Beneš, D. Manara, R.J.M. Konings, M.W.D. Cooper, R.W. Grimes, C. Guéneau. Journal of Nuclear Materials 484 (2017) 1-6.*

3.1. Introduction

The heat capacity of a material is an important thermodynamic property describing the relation between heat and temperature, and is therefore of crucial importance for materials engineering. Heat capacity itself is strongly temperature dependent, and this dependence can be well described by the phonon structure of a solid, which represents the vibrational motions in the crystal as collective oscillations. According to Debye theory, the heat capacity of a perfect crystal is zero at the absolute zero of temperature, since no motion exists, and approaches the Dulong-Petit limit $3NR$ at high temperature, where N is the number of moles of atoms and R is the universal gas constant. In real crystals, however, the effect of electronic contributions and anharmonicity due to lattice imperfections must also be taken into account.

In view of this, the temperature dependence of the heat capacity of refractory ceramic materials can be divided in three regions: (a) the low temperature region in which the heat capacity rapidly rises to reach the Dulong-Petit limit, (b) the intermediate region in which the heat capacity is approximately constant and close to the Dulong-Petit limit, and (c) the high temperature region in which anharmonicity effects due to the contribution of lattice thermal defects cause an excess contribution. As an example, figure 3.1 shows the heat capacity of ThO$_2$, which reaches the Dulong-Petit limit around 500 K and exhibits a strong increase above 2000 K, which has been attributed to Oxygen Frenkel Pair (OFP) formation [1]. The same effects have been observed for other fluorite structured actinide dioxides, such as UO$_2$ and PuO$_2$ [1].

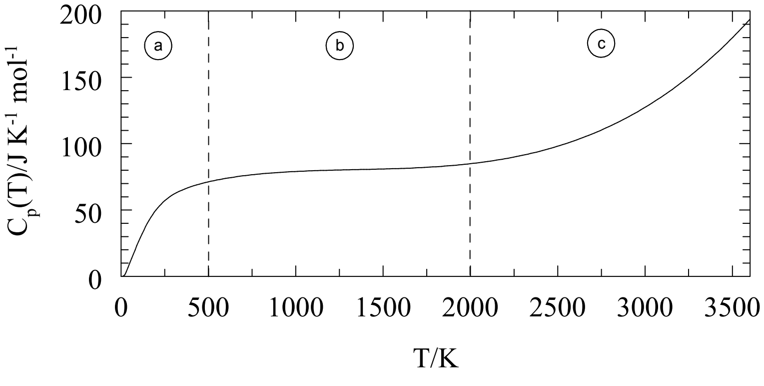

Figure 3.1: The heat capacity of ThO$_2$ from 0 K to the melting point showing the three typical temperature regions: (a) the low temperature region in which the heat capacity rapidly rises to reach the Dulong-Petit limit, (b) the intermediate region in which the heat capacity is approximately constant and close to the Dulong-Petit limit, and (c) the high temperature region in which anharmonicity effects due to the contribution of lattice thermal defects cause an excess contribution. The graph is based on the recommended data by Konings *et al.* [8], obtained by an assessment of experimental enthalpy increment and heat capacity data.

The heat capacity of solid solutions has the same temperature dependence, but due to the mixing of atoms on the lattice sites, the effect of impurity-phonon scattering has to be considered, which and is highly dependent on the differences in the mass and size of the substitutional atoms. This effect was very clearly observed in the solid solutions of the lanthanide phosphates with monazite structure [2], which revealed an increasing excess enthalpy with increasing difference in the ionic radius of the lanthanides. In the absence of such strain effects, the heat capacity of solid solutions can be described well by the Neumann-Kopp rule, which states that it is the weighted average of the end members.

In our studies of the actinide dioxides solutions we are addressing these issues with the goal to obtain a detailed predictive understanding of the heat capacity and other thermodynamic quantities over a wide temperature range. In this paper we will examine the (Th,U)O_2 and (U,Pu)O_2 solid solutions in detail. First we will present enthalpy drop calorimetric measurements to examine whether the mixed oxide solid solution exhibits impurity-phonon scattering (lattice strain) effects or follows the Neumann-Kopp rule, and second we will use the model for the OFP contribution to the heat capacity that we have applied to the actinide dioxides [1], to describe the high temperature heat capacity of the mixed oxide solid solution and compare the results to literature data. Finally comparison will be made to molecular dynamics calculations employing a many-body potential recently developed by Cooper-Rushton-Grimes (CRG) for a range of actinide oxides and their solid solutions [3–5].

3.2. The intermediate temperature region: checking the Neumann-Kopp rule

Enthalpy increments for (Th,U)O_2 samples (about 100 mg) with 20, 40 and 60 mol% uranium were measured using a Setaram MHTC-96 calorimeter operating in drop mode, the maximum operating temperature of which is 1773 K, using a constant gas flow of helium (see [6] for details on the operation and calibration procedures). The standard deviation of the multiple drops at each temperature was between 3 and 6 %. The samples were prepared from aqueous solutions using a gel-supported precipitation route, followed by sintering to produce dense pellets. The U/(Th+U) composition was derived from the analysis of the metal concentrations in the starting solution (thorium nitrate and uranyl nitrate, respectively). The materials were analyses by X-Ray powder diffraction (XRD), confirming that they were single phase materials. The measured lattice parameters (table 3.1) agreed with those expected for these compositions assuming a Vegard's law interpolation between the end-members, consistent with the observations of Hubert *et al.* [7] and the calculations by Cooper *et al.* [4], confirming that the oxygen-to-metal ratio is 1.99 ± 0.01.

The results for the three compositions of the (Th,U)O_2 solid solution have been compared to the results for ideal behaviour (i.e. complying with the molar additivity rule (Neumann-Kopp)), and the difference is shown in figure 3.2. The data for the end-member have been taken form a recent critical review [8]. It is clear that our results are in fair to good agreement with the additivity rule, the difference being on the order of ± 6 %. It should be noted that the absolute error is relatively large, as the difference values are a small number calculated from three much larger numbers (the experimental value and the values for the two end-members), and is not shown in the graphs.

Table 3.1: Characteristics of the samples used for calorimetric measurements.

Sample composition	Synthesis Technique[a]	lattice parameter/nm	O/M	reference
$Th_{0.60}U_{0.20}O_2$	GSP	555.01(2)	1.99 ± 0.01	[12]
$Th_{0.40}U_{0.40}O_2$	GSP	552.43(2)	1.99 ± 0.01	[12]
$Th_{0.20}U_{0.60}O_2$	GSP	549.85(2)	1.99 ± 0.01	[12]
$U_{0.75}Pu_{0.25}O_2$	GSP	545.45(2)	1.99 ± 0.01[b]	[11]
$U_{0.50}Pu_{0.50}O_2$	GSP	543.77(2)	1.99 ± 0.01[b]	[11]
$U_{0.75}Pu_{0.25}O_2$	GSP	541.5(3)	1.99 ± 0.01	[11]
$U_{0.20}Pu_{0.80}O_2$	infiltration	540.77(3)	2.00 ± 0.01	[11]
$U_{0.10}Pu_{0.90}O_2$	infiltration	540.37(2)	2.01 ± 0.01	[11]

[a] *GSP, gel-supported precipitation;*
[b] *Confirmed by XANES analysis [12].*

Enthalpy increments for the compositions $(Th_{0.90}U_{0.10})O_2$, $(Th_{0.50}U_{0.50})O_2$ and $(Th_{0.10}U_{0.90})O_2$ have also been reported by Anthonysamy *et al.* [9] and Kandan *et al.* [10] in the temperature range 400 to 800 K. Their results, analysed in a similar manner, are also shown in figure 3.2 and also reveal no measurable deviation from the additivity rule, the uncertainty being approximately a factor two to three smaller than our results. Thus it is clear that the enthalpy increment and therefore also the heat capacity of the $(Th,U)O_2$ solid solution can be described satisfactorily by the Neumann-Kopp rule in this temperature range, confirming the conclusions from Anthonysamy *et al.* [9] and Kandan *et al.* [10].

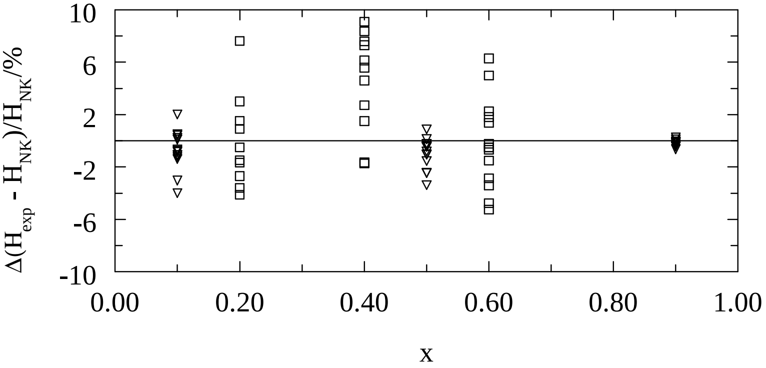

Figure 3.2: The difference between the experimental enthalpy increment data for $(Th_{1-x}U_x)O_2$ and the Neumann-Kopp additivity rule; □, the results of the current study; △ from Anthonysamy *et al.* [9], ▽ the results from Kandan *et al.* [10].

Similarly, a comparison to the Neumann-Kopp additivity rule has been made for the $(U,Pu)O_2$ solid solution. $(U,Pu)O_2$ samples with 25, 50, 75, 80 and 90 mol% plutonium were also prepared using the gel-supported precipitation route and details are

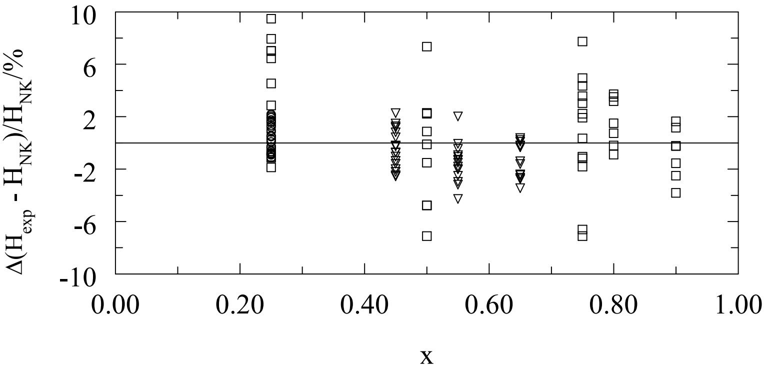

Figure 3.3: The difference between the experimental enthalpy increment data for $(U_{1-x}Pu_x)O_2$ and the Neumann-Kopp additivity rule; □, the results of the current study; ▽ and △ the results from Kandan *et al.* [15, 16]; ○ from Gibby [14].

reported in [11, 12]. The lattice parameters determined by XRD are consistent with Vegards's law [13] and the calculations by Cooper *et al.* [4], and suggest that the oxygen-to-metal ratio is 2.00 ± 0.01 (table 3.1).

The results for the comparison of our results with the molar additivity rule (Neumann-Kopp) for the five compositions measured in this study are shown in figure 3.3 together with those reported by Gibby [14] and Kandan *et al.* [15, 16]. Similar to the (Th,U)O_2 solid solution, we do not find any evidence for deviation from the additivity rule in the experimental values for the (U,Pu)O_2 solid solution. Again, the spread in the our results is a factor of two to three above the other studies.

3.3. The high temperature region: modeling the OFP contribution

In a recent paper [1] we applied the theoretical model proposed by Szwarc [17] to analyse the defect contribution to the high-temperature excess enthalpy of the actinide dioxides above about 2000 K. This model, which is based on the statistical thermodynamic approach developed by Wagner and Schottky [18], describes the excess heat capacity in terms of the energetics of the Oxygen Frenkel pair (OFP) formation, and was preferred to empirical description as for example, used in [19]. The excess heat capacity is given by the equation:

$$C_{p,exc} = \frac{\Delta H_{OFP}^2}{\sqrt{2}\mathbf{R}T^2} \exp\left(\frac{-\Delta H_{OFP}}{2\mathbf{R}T}\right) \exp\left(\frac{\Delta S_{OFP}}{2\mathbf{R}}\right). \tag{3.1}$$

where ΔH_{OFP} and ΔS_{OFP} are the enthalpy and entropy of oxygen Frenkel pair formation, **R** is the universal gas constant, and T is the absolute temperature. By fitting the excess heat capacity for ThO_2, UO_2 and PuO_2, derived from experimental heat capacity and enthalpy increment data, we could derive ΔH_{OFP} and ΔS_{OFP} for these compounds, and the enthalpy values ΔH_{OFP} for were found to be in good agreement with existing literature values from experiments and theoretical data [1, 20]. Particularly a substantial number of Density Functional Theory (DFT) and Molecular Dynamics (MD) studies have reported for UO$_2$ and the recent state-of-the-art DFT/LDA+U [21] and MD [22] studies, not included in the discussion in [1], give further confirmation.

The excess heat capacity caused by OFP formation appeared to start at progressively lower temperature with increasing atomic number of the actinide ion, reflected by a decreasing ΔH_{OFP}. In this analysis the eventual Bredig (superionic) transition in these compounds, related to oxygen Frenkel pair disorder, is neglected because the enthalpy increment data on which our analysis is based, do not reveal evidence for it. This transition has been reported for UO$_2$ by Hiernaut *et al.* [23] and for ThO$_2$ by Ronchi and Hiernaut [24] and has been explained by order-disorder displacement at the anion site, and is thus closely related to OFP formation. We will discuss this further in the next sections.

For the (Th,U)O$_2$ solid solution we have applied an interpolation for the ΔH_{OFP} and ΔS_{OFP} values assuming an ideal mixing behaviour, as shown in the equations below:

$$\Delta H^{ss}_{OFP} = x \times \Delta H^{ThO_2}_{OFP} + (1-x) \times \Delta H^{UO_2}_{OFP} \tag{3.2}$$

$$\Delta S^{ss}_{OFP} = x \times \Delta S^{ThO_2}_{OFP} + (1-x) \times \Delta S^{UO_2}_{OFP} \tag{3.3}$$

The results for three compositions of the (Th$_{1-x}$U$_x$)O$_2$ solution thus obtained from the lattice contributions and the excess contributions from equation 3.1 are shown in figure 3.4, in a plot of the apparent heat capacity of reduced enthalpy increment $\{H°(T) - H°(298.15K)\}/(T - 298.15)$, which is a highly sensitive function. The compositions were chosen such that they can be compared to the experimental enthalpy increment data from 2300 to 3400 K as reported by Fischer *et al.* [25]. To enable this comparison, we have to estimate the lattice heat capacity of the solid solution. This was done by applying the Neumann-Kopp rule to the lattice contributions considered in our work on the actinide dioxides [1], in line with the results presented in the previous section. The agreement for the highest U concentration (Th$_{0.70}$U$_{0.30}$)O$_2$ is excellent, confirming that a consistent model for the end-members and the solid solution has been obtained. This is further confirmed by comparison to the results for the (Th$_{0.85}$U$_{0.15}$)O$_2$ composition for which the enthalpy increments were also measured by Fischer *et al.* [25], also shown in figure 3.4. Unfortunately the experimental results for the (Th$_{0.92}$U$_{0.08}$)O$_2$ composition by Fischer *et al.* do not fit the calculations that well, the values being even below the ThO$_2$ curve, as already noted by the authors [25]. It should be noted that this sample was fabricated in a different laboratory, compared to the other two samples, and the deviation could be explained by an incorrect oxygen-to-metal ratio determination for this case.

Similarly, the reduced enthalpy increment of the (U$_{0.80}$Pu$_{0.20}$)O$_2$ composition has been calculated from the ΔH_{OFP} and ΔS_{OFP} values for the end members and compared to the experimental results by Ogard [26] for samples with stoichiometry O/(U+Pu) = 2.00 and 1.98. Figure 3.5 shows that an excellent agreement exists between the experimental and calculated results in the complete temperature range of the measure-

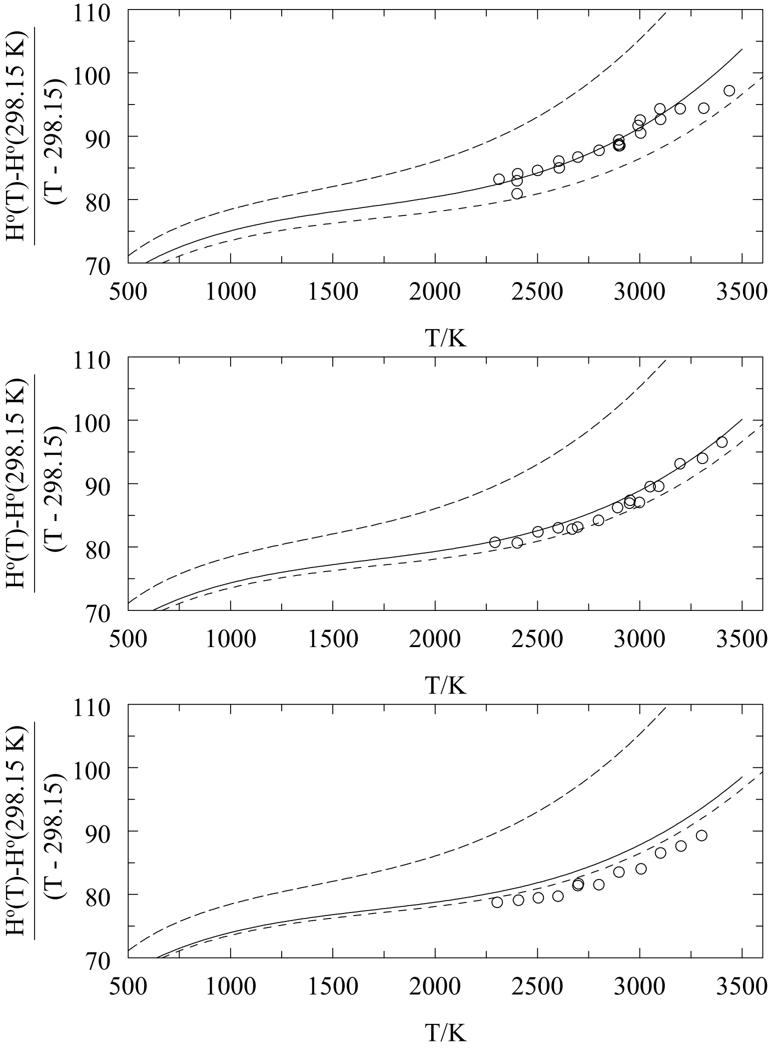

Figure 3.4: The reduced enthalpy increment (in J·K^{-1}·mol^{-1}) of $(Th_{0.70}U_{0.30})O_2$ (top), $(Th_{0.85}U_{0.15})O_2$ (middle) and $(Th_{0.92}U_{0.08})O_2$ (bottom); the solid lines represent the results of the calculation based on the Szwarc model presented in this work; the symbols show the experimental data from Fischer *et al.* [25]; the dashed lines show the curves for the end members ThO_2 and UO_2.

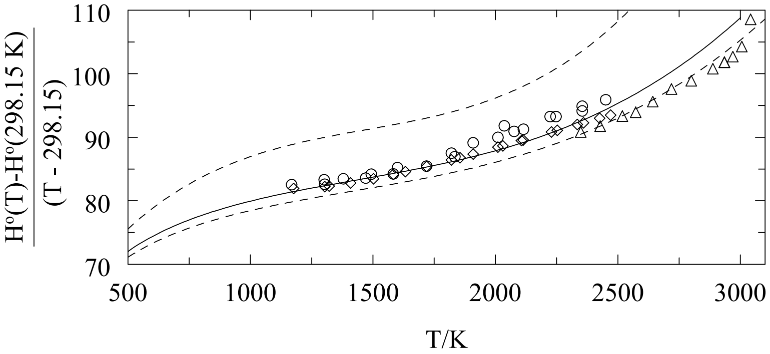

Figure 3.5: The reduced enthalpy increment (in J·K^{-1}·mol^{-1}) of $(U_{0.80}Pu_{0.20})O_2$, the line represents the results of the calculation presented in this work, ○ show the experimental data from Ogard [26] or O/(U+Pu) = 2.00, ⋄ show the experimental data from Ogard [26] for O/(U+Pu) = 1.98 and △ the experimental data from Leibowitz *et al.* [27] for O/(Pu+Pu) = 1.97.

ments, confirming our approach. Also shown are the results by Leibowitz *et al.* [27] for a $(U_{0.80}Pu_{0.20})O_2$ sample with O/(U+Pu) = 1.97, which are slightly lower than those by Ogard. The overall trend in these results may suggests that the energetics of formation and/or annihilation of OFP's in these compounds change with the concentration of the oxygen vacancies in the structure.

This approach yields heat capacity values which are close to those obtained from the NK interpolation to about 2000 K, above that temperature the results obtained by Szwarc's model for oxygen Frenkel pair formation (OPF) are systematically lower, up to 4 J·K^{-1}·mol^{-1} for $(Th_{0.70}U_{0.30})O_2$ and 6 J·K^{-1}·mol^{-1} for $(U_{0.80}Pu_{0.20})O_2$, which is due to the non-linear nature of equation 3.1.

3.4. The high temperature region: comparison to many-body potential model calculations

Cooper-Rushton-Grimes (CRG) [3, 4] developed a many-body potential model for describing a range of thermophysical properties of actinide dioxides and their solid solutions, including heat capacity. It is interesting to compare the enthalpy increment data obtained by that approach to the $(Th_{1-x}U_x)O_2$ and $(U_{0.80}Pu_{0.20})O_2$ compositions extensively discussed in the previous section. Therefore additional molecular dynamics simulations were carried out using the LAMMPS [28] code in conjunction with this many-body potential [3–5]. The model describes pairwise interactions using a conventional short range Buckingham-Morse potential [29, 30] with long range electrostatic forces calculated using the Ewald method [31] with the Particle-Particle Particle-Mesh (PPPM) implementation [32]. In addition to the pairwise description, many-body effects are incorporated using the the embedded atom method (EAM) of Daw and Baskes [33] in a way that modulates the interactions such that each bond becomes progressively weaker as the coordination of a given atom is increased [34]. Consequently, the potential was able to reproduce a wide range to thermophyscial properties from 300 K to 3000 K. The parameters developed for the mixed oxide systems are given in reference [3, 4] for (U,Th)O_2 and [4, 5] (U,Pu)O_2, respectively. Note also that the (U,Pu)O_2 parameters were modified [5] from the original potential set [3] to enable the PuO_2 melting point to be more accurately reproduced. Solid solution structures for $(U_{0.80}Pu_{0.20})O_2$, $(Th_{0.70}U_{0.30})O_2$, $(Th_{0.85}Pu_{0.15})O_2$ and $(Th_{0.92}U_{0.08})O_2$ were generated by randomly assigning U^{4+}, Pu^{4+} and Th^{4+} cations across the 4a Wyckoff sites (fluorite actinide sites) throughout a 10 × 10 × 10 fluorite unit cell. Stoichiometry was maintained throughout, such that the metal to oxygen ratio is always 2. These systems were equilibrated at zero pressures and a range of temperatures for 20 ps in the NPT ensemble using thermostat and barostat relaxation times of 0.1 ps and 0.5 ps respectively. Over the final 4ps of equilibration the enthalpy of the system was averaged. This was repeated for temperatures ranging from 300 K to 3600 K (ThO_2 melting point) at 25 K intervals. For each composition this procedure was repeated for 10 randomly generated structures.

The results, also expressed as reduced enthalpy increment, are shown in figure 3.6 and can be compared to the experimental results in figures 3.4 and 3.5. It can be observed that the computational results for the $(Th_{1-x}U_x)O_2$ solid solution are in reasonable agreement with the experimental results and the estimates based on the OFP model described in the previous section. In the lower temperature range the CRG model slightly overestimates the reduced enthalpy increment, and thus the heat capacity, and in the mid range the agreement is very good, also confirming that the additivity rule (Neumann-Kopp) is followed. The most striking difference occurs in the high temperature region, for which the CRG calculations show an anomaly that is related to the diffuse Bredig transition predicted for all three compositions, which is not present in the OFP model, nor in the experimental enthalpy data.

The same observation is made for the $(U_{0.80}Pu_{0.20})O_2$ solid solution, though the overall agreement is less than for $(Th_{1-x}U_x)O_2$. This may be explained due to the lower PuO_2 reduced enthalpy in the Debye region that was predicted by the CRG potential compared to the experiment. Despite the high temperature Bredig transition predicted by the model for UO_2, PuO_2 and (U,Pu)O_2 [5] it is not sufficient to compensate for the low prediction of reduced enthalpy at intermediate temperatures. Note that in the original CRG paper the PuO_2 heat capacity was predicted to be relatively constant [3], however this is thought to be an artifact of the polynomial form used in the analysis and the later more rigorous investigation using this potential exhibits the Bredig transition [5].

Although figure 3.6 indicates differences between the experiment and MD calculations particularly for the lattice contribution in the Debye region, it shows that in the high temperature regime the onset temperature for excess enthalpy and heat capacity are in qualitative agreement. Addition of U to ThO_2 (see figure 3.6a) reduces the temperature at which excess heat capacity occurs, in line with the results reported in figure 3.4. However, the effect of adding U to ThO_2 is more significant for the MD results than for the analytical model. This can be explained by considering that there exist a wide range of unique oxygen environments in our MD simulations that arise due the random distribution of actinides on the cation sublattice. Consequently, for a given actinide composition there is a probability distribution associated with the OFP energy. These distributions have been examined previously [4, 5], indicating a skew towards OFP energies

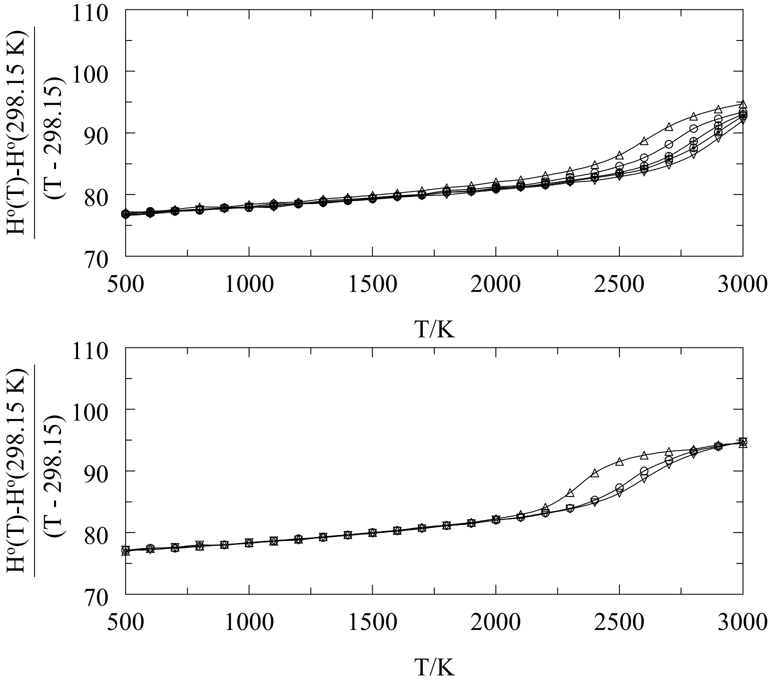

Figure 3.6: The reduced enthalpy increment (in J·K^{-1}·mol^{-1}) of (Th$_{1-x}$U$_x$)O$_2$ for x = 0.08, 0.15 and 0.30 (top) and (U$_{1-x}$Pu$_x$)O$_2$ for x = 0.20 (bottom). The solid lines represents the results of the MD calculations using the CRG potential.

that are lower in the mixed systems than the linear interpolation of the end members. The treatment for the OFP energy in equation 3.1 does not account for this. Nonetheless, without a more detailed examination of cation distribution at the atomic scale it is not clear which approach is best suited to describing real mixed systems. Figure 3.6b shows that additions of Pu to UO_2 also reduce the temperature at which excess heat capacity is predicted by MD. Although the absolute values for reduced enthalpy are not in agreement, this temperature shift for excess enthalpy in $(U_{0.80}Pu_{0.20})O_2$ is in line with the prediction made using the analytical model and the experimental data.

It should be remarked that the OFP concentrations calculated by the analytical Szwarc model and the MD calculations are in fair agreement: the fraction rises up to 0.01 to 0.05 near the melting temperature for the analytical model, depending on the Pu concentration, and up to 0.03 for the MD calculations in the region below the Bredig transition (this transition prevents calculating concentrations at higher temperatures). These values are somewhat lower than those found in high-temperature neutron diffraction studies, which show that the defect concentration increases to 0.15 near the melting [35].

3.5. The pre-melting region: the effect of oxygen point defects

Finally, we checked for the effect of oxygen point defects caused by changes in the composition at very high temperature (pre-melting) related to the reduction of the dioxide to a slight substoichiometric phase. Calculations were performed for $(U_{0.80}Pu_{0.20})O_2$ with the ThermoCalc Software using the database for the U-Pu-O system from the assessment by Guéneau *et al.* [36]. The calculation was simulating the capsule design and dimension from the paper by Ogard [26], for a constant volume corresponding to the free volume and an Ar gas atmosphere (0.33 atm). The calculation showed that equilibrium between the $(U_{0.80}Pu_{0.20})O_2$ sample and the gas phase leads to a very small deviation from the initial stoichiometry at very high temperature ($\delta(O/M) < 0.0025$ at 3000 K for initial $O/(U+Pu) = 2.00$ as shown in figure 3.7, and $\delta(O/M) < 0.0225$ for at 3000 K for initial $O/(U+Pu) = 1.98$), with no significant impact of the related oxygen point defects on the heat capacity. It should be noted here that in an open system, the effect would be more pronounced.

3.6. Discussion and Conclusions

The current analysis can be combined with recent results concerning the heat capacity of the $(Th,Pu)O_2$ solid solution, for which measurements were made in the low-temperature regime (4-300 K) [37] and the intermediate regime (400-1700 K) [38] to obtain a clear picture about in the widest possible temperature range.

The low-temperature heat capacity measurements for the $(Th,Pu)O_2$ solid solution have shown that below 30 K an effect of cation substitution is clearly observable. In absolute sense the heat capacity of the mixed oxide solutions is systematically above that of the end members, in relative sense the excess reaches 50 % of the lattice heat capacity, calculated from the end members by the additivity rule (NK rule) at the lowest

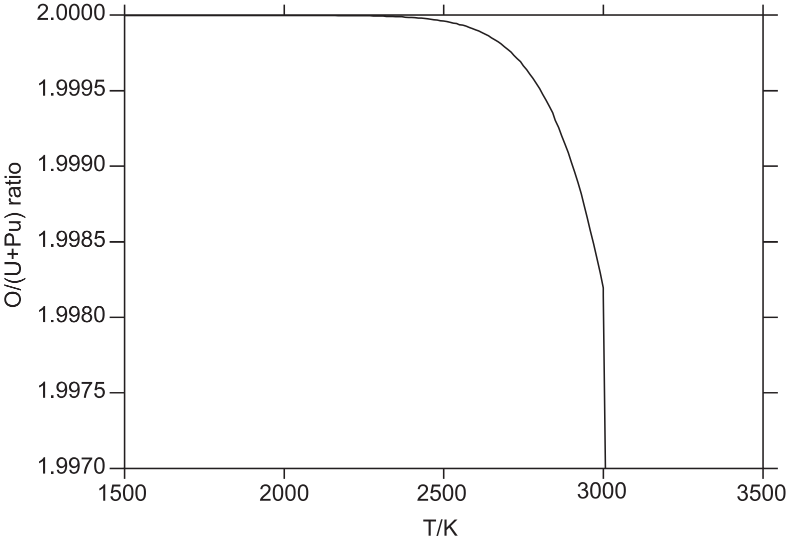

Figure 3.7: The O/(U+Pu) ratio as a function of temperature as obtained from thermodynamic simulation of the drop calorimetric experiment for of $(U_{0.80}Pu_{0.20})O_2$ by Ogard [26].

temperatures and quickly decreases with increasing temperature, approaching values close or just above those obtained from the NK rule. This is caused by cation substitutional disorder in the crystal leading to phonon scattering as a result of lattice strain. This is highly dependent on the differences in the size of the substitutional atoms, which are the largest in(Th,Pu)O$_2$ solid solution when considering actinide dioxides. It is expected to be less pronounced in the (Th,U)O$_2$ and (U,Pu)O$_2$ solid solutions, but experimental data to confirm this are lacking.

In the intermediate temperature range, the experimental enthalpy increments data from literature sources and obtained in our laboratory for (Th,Pu)O$_2$, (Th,U)O$_2$ and (U,Pu)O$_2$ show no deviations from the NK rule and yield heat capacity values close to the Dulong-Petit limit of $6R$.

The available literature data in the high temperature range for enthalpy increments show an excess heat capacity contribution that can be described well by Szwarc's model for OFP in fluorite dioxides. We have shown that by linear interpolation of the enthalpies and entropies of oxygen Frenkel pair formation for the end-members, as derived by us in earlier work [1], the experimental enthalpy data can be described quite accurately. In principle this interpolation yields results that are close to those obtained by the additivity rule, but with more firm physical basis. These data are, however, not in agreement with the results of many-body potential model calculations that clearly show the contribution of the Bredig transition to the enthalpy.

The Bredig (superionic) transition has been reported by Hiernaut *et al.* [23] for UO$_2$ and by Ronchi and Hiernaut [24] for ThO$_2$ and has been explained by order-disorder displacement on the anion site, with the maximum disorder occurring at the transition. Its existence was derived from thermal arrests in cooling curves for laser-heated samples, but was strongly dependent on the gas atmosphere. Neutron scattering measurements by Hutchings [39] gave evidence for thermally induced Frenkel oxygen lattice disorder at temperatures > 2000 K in UO_2 and ThO_2, with the total of defective anions steadily increasing to approximately 30 % at T = 2930 K. A recent synchrotron X-ray study also indicated substantial oxygen disorder in UO_2 in the temperature range of the Bredig transition [40], with increasing U-U distance with temperature, in agreement with lattice expansion, but decreasing U-O distance. The authors found a good agreement with the results of the molecular dynamics study by Yakub *et al.* [41] that showed the Bredig (superionic) transition at around 2700 K.

According to the CRG calculations the enthalpy effect of the Bredig (superionic) transition is substantial, of the order of 30 $\mathrm{kJ{\cdot}mol^{-1}}$ (figures 3.4 and 3.5) and although it is diffuse, the magnitude is such that it should have been detected in the enthalpy increment measurements by [25–27] as an inflection. It could be argued that the during the enthalpy drop measurements the disordered state is quenched and that the measurements do not refer to the ideal crystal but to a disordered end state. This is, however, not likely because in the laser heating measurements by Hiernaut and Ronchi [23, 24] very fast quenching was applied also, faster than the calorimetric measurements, and the energy release of the restructuring to the ordered state was observed as a clear thermal arrest. Our recent measurements performed on laser melting and quenched ThO_2, UO_2, and PuO_2 samples [12, 42–44] show neither a thermal arrest nor quenching of a highly disordered crystal structure, which should be visible by X-ray diffraction and Raman spectroscopy. It is thus not straightforward to reconcile the experimental results.

A possible explanation should be sought in defect types and energetics. It is well known that defect clustering occurs in UO_2 [13] and that the concentration of such clusters increases with temperature, where the mobility of point defects increases. In this context the configurational entropy of point defects and small clusters must also be considered. This quantity has been shown to be surprisingly large in strongly defected solids, leading to significant corrections to the free energies of defect clusters at high temperatures [45]. Another factor is that there does not exist just one OFP energy in the solid solution but rather there are a wide range of possible oxygen environments depending on the local actinide coordination. Moreover, considering the high concentration of defects at high temperatures, a concentration and hence a temperature dependence of the defect formation energies should be considered. In the Szwarc's model this is not accounted for and the OFP energy obtained from that model must be considered as an "effective" energy. We hypothesize here that such energetic differences can lead to a shift of the Bredig (superionic) transition to higher temperature, as a result of which the maximum of the disordering could occur upon melting and not before.

References

[1] R. J. M. Konings and O. Beneš. J. Phys. Chem. Solids 74 (2013) 653–655.

[2] K. Popa, R. J. M. Konings, and T. Geisler. J. Chem. Thermodyn. 39 (2006) 236–239.

[3] M. W. D. Cooper, M. J. D. Rushton, and R. W. Grimes. J. Phys.: Condens. Matter 26 (2014) 105401.

[4] M. W. D. Cooper, S. T. Murphy, P. C. M. Fossati, Michael, J. D. Rushton, and R. W. Grimes. Proc. R. Soc. A 470 (2014) 20140427.

[5] M. W. D. Cooper, S. T. Murphy, M. J. D. Rushdon, and R. W. Grimes. J. Nucl. Mater. 461 (2015) 206–214.

[6] D. Sedmidubský, O. Beneš, and R. J. M. Konings. J. Chem. Thermodyn. 37 (2005) 1098–1103.

[7] S. Hubert, J. Purans, G. Heisbourg, P. Moisy, and N. Dacheux. Inorg. Chem. 45 (2006) 3887–3894.

[8] R. J. M. Konings, O. Beneš, A. Kovács, D. Manara, D. Sedmidubský, L. Gorokhov, V. S. Iorish, and V. Yungman. J. Phys. Chem. Ref. Data 43 (2014) 013101.

[9] S. Anthonysamya, J. Joseph, and P. R. Vasudeva Rao. J. Alloys Comp. 299 (2000) 112–117.

[10] R. Kandan, R. Babu, P. Manikandan, R. Venkata Krishnan, and K. Nagarajan. J. Nucl. Mater. 384 (2009) 231–235.

[11] F. De Bruycker, K. Boboridis, P. Pöml, R. Eloirdi, R.J.M. Konings, and D. Manara. J. Nucl. Mater. 416 (2011) 166–172.

[12] R. Böhler, M. J. Welland, D. Prieur, P. Çakir, T. Vitova, T. Pruessmann, I. Pidchenko, C. Hennig, C. Guéneau, R. J. M. Konings, and D. Manara. J. Nucl. Mater. 448 (2014) 330–339.

[13] C. Guéneau, A. Chartier, and L. Van Brutzel. *Comprehensive Nuclear Materials*, volume 2, Chapter 2.02. R. J. M. Konings and T. Allen and R. Stoller and S. Yamanaka, (Ed.), Elsevier, (2012).

[14] R. L. Gibby. Hanford Engineering Development Laboratory, Technical Report HEDL-TME-73-19, (1973).

[15] R. Kandan, R. Babu, K. Nagarajan, and P. R. Vasudeva Rao. J. Nucl. Mater. 324 (2004) 215–219.

[16] R. Kandan, R. Babu, K. Nagarajan, and P. R. Vasudeva Rao. Thermochim. Acta 472 (2008) 46–49.

[17] R. Szwarc. J. Phys. Chem. Solids 30 (1969) 705–712.

[18] C. Wagner and 163 (193 1); W. Schottky ., Z. phys. Chem. Bll. Z. Phys. Chem. B 11 (1931) 163.

[19] J. K. Fink. J. Nucl. Mater. 279 (2000) 1–18.

[20] R. J. M. Konings and M. Bertolus. *Behaviour and Properties of Nuclear Fuels*, Chapter 6. J. Gibson and W. de Jong, (Ed.), Wliely Publishers, (2017).

[21] E. Vathonne, J. Wiktor, M. Freyss, G. Jomard, and M. Bertolus. J. Phys.: Condens. Matter 26 (2014) 325501.

[22] Raoul Ngayam-Happy, Matthias Krack, and Andreas Pautz. J. Phys.: Condens. Matter 27(45) (2015) 455401.

[23] J. P. Hiernaut, G. J. Hyland, and C. Ronchi. Int. J. Thermophys. 14 (1993) 259–283.

[24] C. Ronchi and J.P. Hiernaut. J. Alloys Comp. 240 (1996) 179–185.

[25] D. F. Fischer, J. K. Fink, L. Leibowitz, and J. Belle. J. Nucl. Mater. 118 (1983) 342–348.

[26] A. E. Ogard and J. A. Leary. In *Thermodynamics of Nuclear Materials 1967*, page 651. International Atomic Energy Agency, Vienna, (1968).

[27] L. Leibowitz, D. F. Fischer, and M. G. Chasanov. J. Nucl. Mater. 42 (1972) 113–116.

[28] S. Plimpton. J. Comp. Phys. 117 (1995) 1–19.

[29] R .A. Buckingham. Proc. Roy. Soc. Lond. A 168 (1938) 264–283.

[30] P. Morse. Phys. Rev. 34 (1929) 57–64.

[31] P. P. Ewald. Ann. Phys. 369 (1921) 253–287.

[32] R. W. Hockney and J. W. Eastwood. *Computer Simulation using Particles.* Adam Hilger, New York, NY, (1988).

[33] M.S. Daw and M.I. Baskes. Phys. Rev. B 29 (1984) 6442–6453.

[34] M. W. D. Cooper. *Atomistic Simulation of Nuclear Fuel.* PhD thesis, Imperial College London, (2015).

[35] K. Clausen, W. Hayes, J. E. Macdonald, and R. Osborn. Phys. Rev. Lett. 52 (1984) 1238–1241.

[36] C. Guéneau, N. Dupin, C. Martial, J. C Dumas, S. Gossé, S. Chatain, B. Sundman, F. De Bruycker, D. Manara, and R.J.M. Konings. J. Nucl. Mater. 419 (2011) 145–167.

[37] S. O. Vălu, O. Beneš, R. J. M. Konings, J. C. Griveau, and E. Colineau. J. Phys. Chem. Solids submitted (2014).

[38] S. O. Vălu, D. Staicu, O. Beneš, R. J. M. Konings, and P. Lajarge. J. Alloys Comps. 614 (2014) 144.

[39] M. T. Hutchings. J. Chem. Soc. Faraday Trans. II 83 (1987) 1083–1103.

[40] L. B. Skinner, C. J. Benmore, J. K. R. Weber, M. A. Williamson, A. Tamalonis, A. Hebden, T. Wiencek, O. L. Alderman, M. Guthrie, Leibowitz, and J. B. Parise. Science 346 (2014) 984–987.

[41] E. Yakub, C. Ronchi, and D. Staicu. J. Chem. Phys. 127 (2007) 094508.

[42] D. Manara, C. Ronchi, and M. Sheindlin. High Temp.-High Press. 35/36 (2003) 25–33.

[43] D. Manara, C. Ronchi, M. Sheindlin, M. Lewis, and M. Brykin. J. Nucl. Mater. 342 (2005) 148–163.

[44] F. De Bruycker, K. Boboridis, D. Manara, P. Pöml, M. Rini, and R. J. M. Konings. Materials Today 13(11) (2010) 52–55.

[45] S. S. Kapur, M. Prasad, J. C. Crocker, and T. Sinno. Phys. Rev. B 72 (2005) 014119.

4

Heat capacity, thermal conductivity and thermal diffusivity of uranium-americium mixed oxides

The enthalpy increments of $(U_{1-y},Am_y)O_{2-x}$ mixed oxides with y= 0.0877 and 0.1895 and x= 0.01-0.03 were measured using drop calorimetry in the temperature range 425-1790 K and the heat capacity was obtained as differential of the obtained enthalpy increments with respect to temperature. The thermal diffusivity was measured using the laser flash technique from 500 to 1550 K. The thermal conductivity was calculated and analyzed from the measured thermal diffusivity, density and heat capacity. Measured enthalpy increments of the $(U_{1-y},Am_y)O_{2-x}$ solid solutions are very close to the end members, indicating no excess contribution. The derived heat capacities for the two intermediate compositions are slightly higher than that of UO_2 and in a good agreement with literature data of AmO_2 up to 1100 K. For the thermal conductivity of $(U, Am)O_{2-x}$ mixed oxides a correlation using the classical phonon transport model in crystal structures is proposed.

This chapter is reprinted with kind permission of Elsevier: *Heat capacity, thermal conductivity and thermal diffusivity of uranium-americium mixed oxides. O.S. Vălu, D. Staicu, O. Beneš, R.J.M. Konings, P. Lajarge. Journal of Alloys and Compounds 614 (2014) 144-150.*

4.1. Introduction

The most abundant transuranium elements found in the high level waste from reprocessed nuclear power reactor fuels are Am and Np. Within the realm of partitioning and transmutation, these long-lived minor actinides and Pu should be recycled in fast reactors, in which they are transmuted to short lived fission products. Thus the long term hazard is alleviated. The solid solution formed by uranium and americium oxides is a possible target for recycling americium in fast neutron reactors. For this reason the synthesis and the thermodynamic properties of the (U,Am)O_{2-x} mixed oxides needs to be investigated.

In order to understand the behavior of nuclear fuel during irradiation it is mandatory to have clear information about the thermodynamic properties of the fuel material in its pristine state. The heat capacity and thermal conductivities of the (U, Am)O_{2-x} solid solution are essential for the reactor design and safety calculations. There is a significant number of publications on the synthesis and characterization of (U,Am)O_{2-x} solid solutions [1–4], but very few thermophysical properties studies [5, 6].

In this work, $(U_{1-y},Am_y)O_{2-x}$ solid solutions with y= 0.0877 and 0.1895 and x= 0.01-0.03 were considered. A high temperature calorimeter operated in drop mode was used for the determination of the enthalpy increments in the 425-1790 K temperature range (shown in figure 4.1). From these results the heat capacity was derived. The thermal diffusivities were measured using the laser flash method in the 500 to 1550 K temperature range, and by combining the results with the heat capacity, the thermal conductivity was obtained. An additional goal of this study was to determine possible excess contributions in these thermodynamic properties, as this will allow developing models that reliably interpolate between measured compositions. Experimental data on the thermodynamic properties of these compounds have never been reported in literature, and the results obtained in this study bring a significant contribution to a better description of the (U,Am)O_{2-x} system and can be used for benchmarking theoretical calculations.

4.2. Experimental work

4.2.1. Sample preparation

Samples of (U,Am)O_{2-x} targets were prepared with two ^{241}Am contents (8.77 and 18.95 mol %) and were characterized by Vespa *et al.* [1]. Porous beads (in this case UO_2) were synthesised by a sol-gel process [7, 8] and which were then introduced into the Minor Actinide handling facility, where they were infiltrated with an Am solution. The Am nitrate solution was prepared by dissolution of the oxide. A key step of the process is the infiltration, and it is essential that the porous beads do not dissolve in the Am nitrate solution. For UO_2 porous beads, however, this can become problematic. Adjustment of the free nitrate concentration of the Am solution was required to hinder the dissolution of the beads and to avoid Am precipitation from solution. Thus, the acid concentration was kept low (< 3M HNO_3) during the dissolution of the Am oxide.

Following infiltration, the beads were dried and then calcined in Ar at 800 °C for 2 hours to convert the Am nitrate to oxide. A single infiltration cycle was used to produce a

Table 4.1: (U,Am)O_{2-x} notations, compositions and fabrication data.

Notation	Nominal composition Am/(U+Am)(mol%)	Actual composition[a] Am/(U+Am)(mol%)	Sintering under Ar/H_2	Disk density (% TD[b])
AM10	10	8.77	1650°C, 8 h, 1500 ppm H_2O	87
AM20	20	18.95	1650°C, 24 h, 2400 ppm H_2O	93

[a] *Composition measured by calorimetry [9];*
[b] *TD = theoretical density, determined from gravimetry and geometry.*

sample with ~10 mol% Am. For the higher 20 mol% Am content, the infiltration and calcination steps were repeated once. After the calcination step, the beads were compacted into disks in a bi-directional press, and sintered under humidified Ar/H_2 atmosphere at 1650 °C for 8 and 24 hours, for the 10 and 20 mol% samples, respectively. The density of the 20 mol% sample was 93 % of the theoretical density (%TD), whereas for the 10 mol% Am concentration, sintered disks reached a value of 87 % of TD.

After production, the actual Am content was determined by a calorimetric method [9] measuring the decay heat of ^{241}Am, the results of which are provided in table 4.1. More information about the sample preparation of the uranium-americium mixed oxides can be found in the study of Vespa *et al.* [1]. The notations defined in table 4.1 were used in the text and graphs.

4.2.2. Experimental procedure

Drop calorimetery

The enthalpy increment measurements performed in this study were made with a Setaram Multi Detector High Temperature Calorimeter (MDHTC - 96 type) operated in a drop mode. The temperature scale of the calorimeter was calibrated using high purity (≥ 99.95 %) standard materials (In, Zn, Sn, Pb, Al, Ag and Au). In order to measure active samples, the calorimeter was implanted in a glove-box keeping most of the electrical parts outside in order to minimize the nuclear waste after the operational lifetime of the calorimeter [10] and more importantly easing repairs during its operation.

The samples, as solid fragments, are introduced in a sample holder which is positioned on top of the detector. The furnace is programmed to reach the desired temperature at which the measured heat flow signal is stabilized during 7 hours. After this period the samples are dropped from ambient temperature into the calorimeter which is programmed to maintain a constant temperature. Each drop is repeated every 25 minutes which was sufficient to restabilize the temperature and the heat flow signals. Before and after each sample, a reference material is dropped to determine the sensitivity (signal vs heat ratio) of the detector. As reference material we used small pieces (150-200 mg) of platinum 99.995 %. The system records the energy which is necessary to heat up the sample from the room temperature to the programmed temperature. The details of the instrument were described in our previous study [11] to which we refer for more details.

Thermal Diffusivity

The thermal diffusivity measurements were carried out using a shielded laser flash device [12]. The samples were discs with a thickness of about 1.5 mm, and with a diameter of 5 mm. The faces were checked to ensure that they were plane parallel, without defects. The samples were heated to the measurement temperature in a high frequency furnace, in the temperature range from 500 to 1550 K. The thermal diffusivity measurements were performed under a static atmosphere of 10^{-3} mbar of nitrogen initially containing 0.1 % of oxygen. This atmosphere is usually used to avoid reduction of $(U,Pu)O_2$ samples, without any oxidation of the UO_2 phase present in the samples. Preliminary tests consisting of oxygen potential determinations before and after the thermal diffusivity measurements have shown that under these conditions the oxygen content of fresh stoichiometric UO_2 and $(U,Pu)O_2$ fuels was not modified, enabling us to conclude that this arrangement would be suitable for the $(U,Am)O_{2-x}$ too.

The measured thermogram at each temperature was carefully inspected to ensure that heat transfer conditions were standard. The precision of the individual thermal diffusivity measurements was always better than 2 %, and the overall accuracy is about 5 %, due to sample thickness variations.

4.3. Results and discussion

4.3.1. Enthalpy increment measurements

Enthalpy increment measurements of ceramic $(U_{1-y}Am_y)O_{2-x}$ with y= 0.0877 and 0.1895 were performed in the temperature range 425 - 1765 K. In addition the UO_2 end-member was measured and compared with literature data, obtaining a good agreement. The measured enthalpy increments of UO_2 are given in table 4.2, while enthalpy increments of AM10 and AM20 are listed in tables 4.3 and 4.4 respectively. The samples weight ranged between 46.6 and 142.9 mg for the 10 % Am content sample, 43.7 mg - 94.2 mg for the 20 % Am content sample and 107.6 mg - 157.2 mg for UO_2, respectively. For all experiments, high purity helium gas was used as carrier gas with a flow rate of 2.8 l/h. Helium was selected for its good thermal conductivity. Figure 4.1 shows all measured enthalpy increments and compared with literature data of the end members UO_2 from Konings *et al.* [13] and AmO_2 from Nishi *et al.* [14]. For each measured temperature the corresponding enthalpy increment value represents the mean of all performed measurements at that temperature.

The experimental enthalpy increment values of both intermediate compositions were least square fitted into an Maier-Kelly empirical temperature relationship with a constraint, H_T - $H_{298.15}$ = 0 at T= 298.15, using Origin software. The enthalpy increment fits are shown in figure 4.2.

Figure 4.1 shows a comparison of the obtained enthalpy increments of the UO_2, AM10 and AM20 intermediate compositions together with the enthalpy equations of AmO_2 obtained by Nishi *et al.* [14] and UO_2 assessed by Konings *et al.* [13] from all available literature. Even if Nishi's study only reaches 1100 K we observed that our results match with the AmO_2 values and follow the curve of the UO_2 up to 1800 K. From this

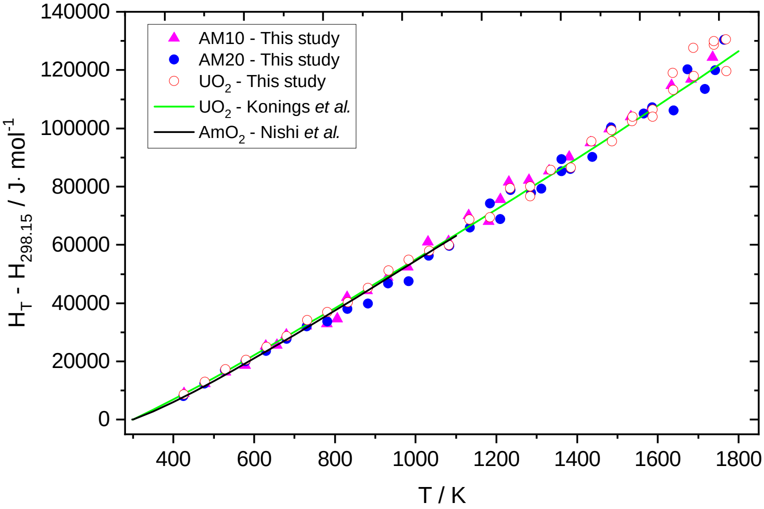

Figure 4.1: The enthalpy increments of the UO_2 end-member, AM10 and AM20 intermediate compositions measured in this study together with enthalpy equations of AmO_2 obtained by Nishi *et al.* [14] and UO_2 assessed by Konings *et al.* [13].

comparison it is difficult to distinguish an independent behaviour of one single component and we conclude that the enthalpy of UO_2 and AmO_2 are very similar for the temperature range 300 - 1800 K. Furthermore, the obtained enthalpy increments of the two intermediate compositions follow the same trend as the end members, indicating no excess contribution to the enthalpy.

To confirm the exact composition of the measured samples, X-ray diffraction measurements were performed at room temperature and the lattice parameters were obtained by Rietveld refinement of the experimental diffraction pattern using a Pseudo-Voigt profile function in the WinPlotr program within the FullProf Suite. The obtained lattice parameters are listed in table 4.5 in which they are compared with the cell parameter values obtained by Vespa *et al.* [1] on fresh sintered samples. In that study the O/M was determined from XRD and XANES measurement. The former gave O/M= 1.977 for AM10 and 1.970 for AM20. The XANES results were O/M= 1.96 for AM10 and 1.93 for AM20.

The powder X-ray diffraction analysis, performed before the enthalpy experiments, revealed a slight increase compared to as-prepared material which we attribute to radiation damage, but after the heat treatment up to about 1780 K in the calorimeter the lattice parameter decreased substantially, close to Vegard's law. Based on this info we assume that the O/M of the measured samples was in the range 1.99 - 1.97, i.e. close to stoichiometry. Oxidation can occur due to the presence of oxygen (∼ 1 ppm) in the flowing gas during the experiment. The partial pressure calculated from the total amount of oxygen present in the experimental chamber at high temperature is enough for changing the stoichiometry of the sample.

The heat capacity functions which describe the two intermediate compositions

Table 4.2: Measured enthalpy increments of the UO_2 and their standard deviations.

T_m / K	H_{T_m} - $H_{(298.15)}$ / $kJ \cdot mol^{-1}$	T_m / K	H_{T_m} - $H_{(298.15)}$ / $kJ \cdot mol^{-1}$
426.7	8.60 ± 0.66	1284.6	80.05 ± 2.22
478.3	12.90 ± 1.23	1335.3	85.61 ± 1.78
529.5	17.18 ± 1.03	1385.5	86.43 ± 2.68
580.3	20.54 ± 0.79	1436.4	95.44 ± 3.02
631.0	24.93 ± 2.10	1486.1	99.30 ± 4.59
681.3	28.58 ± 2.11	1486.4	95.57 ± 5.99
731.9	34.06 ± 3.06	1536.8	102.45 ± 9.30
782.1	36.91 ± 1.45	1537.5	104.00 ± 6.73
832.2	40.26 ± 1.69	1587.2	106.42 ± 10.66
882.4	45.11 ± 0.79	1587.4	103.98 ± 2.72
933.2	51.10 ± 3.27	1637.7	118.92 ± 3.92
982.8	54.89 ± 3.47	1638.7	113.11 ± 7.53
1033.5	57.83 ± 3.73	1688.5	127.56 ± 10.78
1083.2	59.93 ± 3.40	1689.2	117.87 ± 7.06
1133.9	68.71 ± 3.46	1739.1	128.71 ± 17.91
1184.3	69.48 ± 1.62	1739.8	129.82 ± 7.68
1234.6	79.33 ± 5.86	1769.4	130.42 ± 5.13
1284.6	76.70 ± 1.16	1770.4	119.64 ± 6.08

Table 4.3: Measured enthalpy increments of the $U_{0.9123}Am_{0.0877}O_{2-x}$ solid solution and their standard deviations.

T_m / K	H_{T_m} - $H_{(298.15)}$ / $kJ \cdot mol^{-1}$	T_m / K	H_{T_m} - $H_{(298.15)}$ / $kJ \cdot mol^{-1}$
426.0	8.99 ± 0.35	1081.1	61.09 ± 1.85
477.8	12.31 ± 0.27	1131.1	70.02 ± 0.71
529.2	16.26 ± 0.17	1180.8	68.05 ± 2.64
578.2	18.60 ± 0.47	1210.1	75.54 ± 5.71
629.1	25.30 ± 1.05	1230.8	81.55 ± 2.24
656.9	25.60 ± 1.75	1280.8	82.10 ± 6.10
679.5	29.12 ± 0.10	1330.9	85.42 ± 2.43
729.9	32.09 ± 2.00	1380.9	90.17 ± 3.18
780.3	32.96 ± 2.35	1433.4	94.98 ± 8.58
805.4	34.63 ± 0.39	1480.8	99.86 ± 1.97
830.4	41.98 ± 3.04	1533.4	104.01 ± 7.42
880.6	44.27 ± 2.66	1581.2	106.21 ± 6.35
930.7	48.89 ± 4.05	1633.9	114.63 ± 6.49
980.9	52.36 ± 3.50	1682.9	116.81 ± 6.16
1031.1	60.95 ± 4.21	1735.6	124.30 ± 15.76

Table 4.4: Measured enthalpy increments of the $U_{0.8105}Am_{0.1895}O_{2-x}$ solid solution and their standard deviations.

T_m / K	H_{T_m} - $H_{(298.15)}$ / kJ · mol^{-1}	T_m / K	H_{T_m} - $H_{(298.15)}$ / kJ · mol^{-1}
425.2	8.01 ± 0.49	1210.0	68.83 ± 3.60
476.7	12.33 ± 1.14	1235.2	78.85 ± 1.20
527.9	16.91 ± 1.09	1286.2	77.81 ± 4.79
579.1	20.05 ± 0.85	1311.6	79.24 ± 6.00
629.6	23.56 ± 0.23	1362.3	85.22 ± 14.29
680.7	27.73 ± 2.58	1362.2	89.38 ± 5.28
730.8	32.00 ± 2.00	1384.1	86.02 ± 3.90
781.5	33.62 ± 1.56	1437.9	90.08 ± 7.33
831.7	37.96 ± 1.22	1485.0	100.26 ± 10.34
882.1	39.74 ± 0.10	1565.5	105.07 ± 4.51
932.6	46.65 ± 3.07	1586.5	107.11 ± 8.11
983.1	47.41 ± 2.41	1639.8	106.17 ± 8.48
1033.5	56.22 ± 3.62	1673.8	120.13 ± 15.50
1084.1	59.57 ± 1.67	1717.4	113.49 ± 10.45
1135.1	65.91 ± 2.01	1743.0	119.82 ± 14.36
1184.9	74.16 ± 2.53	1764.5	130.28 ± 11.92

Table 4.5: $(U,Am)O_{2-x}$ lattice parameters. The uncertainty of measured lattice parameters are given in parentheses.

Samples Am concentration (mol% metal)	Vegard's Law a (Å)	Vespa *et al.* a (Å)	This study[a] a (Å)	This study[b] a (Å)
8.77	5.461	5.468	5.477(2)	5.463(2)
18.95	5.452	5.461	5.469(3)	5.454(3)

[a] *Measurements performed on the samples before heat treatment in the calorimeter;*
[b] *Measurements performed on the samples after heat treatment in the calorimeter.*

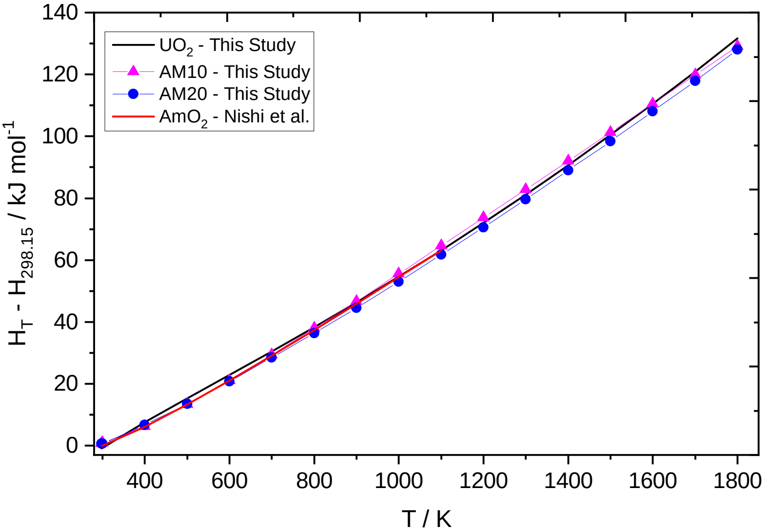

Figure 4.2: Comparison of enthalpy equations of the UO_2 end-member, AM10 and AM20 solid solutions, obtained from the measurements performed in this study, with literature data for AmO_2 [14].

of the $(U,Am)O_{2-x}$ solid solution were obtained using a simultaneous linear regression taking into account all measured enthalpy increments data of each set of experiments, by applying a constraint at 298.15 K to a value of 63.66 $J{\cdot}K^{-1}{\cdot}mol^{-1}$ for AM10 and 63.73 $J{\cdot}K^{-1}{\cdot}mol^{-1}$ for AM20, respectively. Equations 4.2 and 4.3 represent the high temperature heat capacities of the intermediate compositions obtained in this study. In a similar way, the heat capacity function of UO_2 (equation 4.1) was obtained with a constraint corresponding to a value of 63.60 $J{\cdot}K^{-1}{\cdot}mol^{-1}$ at 298.15 K.

$$\text{UO}_2: \quad C_{p,m}/(J\cdot K^{-1}\cdot mol^{-1}) = 72.214 + 14.5847\cdot 10^{-3}\cdot (T/K) - 1.152296\cdot 10^{6}\cdot (T/K)^{-2} \tag{4.1}$$

$$\text{AM10}: \quad C_{p,m}/(J\cdot K^{-1}\cdot mol^{-1}) = 74.172 + 14.6010\cdot 10^{-3}\cdot (T/K) - 1.321384\cdot 10^{6}\cdot (T/K)^{-2} \tag{4.2}$$

$$\text{AM20}: \quad C_{p,m}/(J\cdot K^{-1}\cdot mol^{-1}) = 62.367 + 23.0544\cdot 10^{-3}\cdot (T/K) - 0.489837\cdot 10^{6}\cdot (T/K)^{-2} \tag{4.3}$$

As other heat capacity data have not been reported for any $(U,Am)O_2$ solid solution compositions, the results of our study are compared in figure 4.3 with heat capacity of the end members, UO_2 obtained in this study and AmO_2 by Nishi *et al.* [14]. It is clear that the heat capacity curves obtained in this work are slightly higher than that of UO_2. The AmO_2 curve, based on the enthalpy increment measurements by Nishi *et al.*, is limited to 1100 K. The agreement is good up to this temperature, above the curve by Nishi is significantly lower. This is probably due to the absence of data to adequately describe the high temperature behaviour. Our enthalpy increment results suggest that the heat capacity curve of AmO_2 should be close to that of UO_2. It should be realised that the extrapolation of Nishi's enthalpy increment data to high temperature is strongly dependent on the fitting (type of polynomial, boundary conditions). This is demonstrated by an alternative curve for AmO_2 that was obtained by constraining the fit to an estimated heat capacity at T = 298.15 K, considering that the value in the curve by Nishi *et al.* is unrealistically low. We therefore must conclude that the heat capacity of AmO_2 is highly uncertain beyond the range for which Nishi *et al.* made the measurements. The extrapolation suggested by Nishi *et al.* seems not to be in agreement with the current data for $(U,Am)O_{2-x}$ when applying the Neumann-Kopp's additivity rule, as evidenced by the enthalpy increment of these two compositions. To be in line with that, the heat capacity of AmO_2 should be close to that of UO_2, or even slightly above.

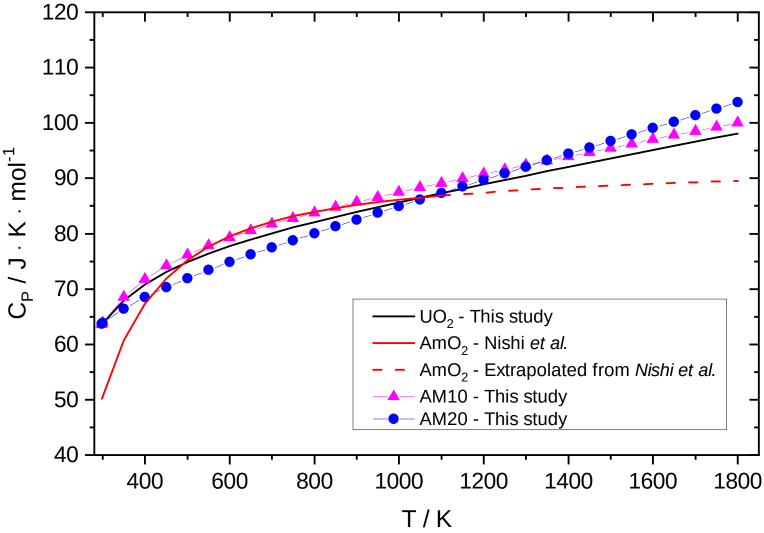

Figure 4.3: Heat capacity functions of the intermediate compositions AM10 and AM20 solid solution, together with the heat capacity functions of the end members UO_2 obtained in this study and AmO_2 from Nishi *et al.* [14].

4.3.2. Thermal Diffusivity

When performing thermal diffusivity measurements, one has to take into account that the high α activity of the sample could affect the material properties by inducing the auto-irradiation of the material. Auto-irradiation could lead to well-known phenomena at the structural scale such as amorphization, allotropic transitions, lattice parameter expansion, defect formation and pellet swelling at the macroscopic scale [15]. For this reason a heat treatment was used to anneal auto-irradiation damage. XRD analysis has confirmed that the heat treatment had changed the lattice parameters, close to the values obtained by Vegard's law suggesting that the sample returned to the near stoichiometric composition.

The laser-flash measurements were done about 500 days after the end of the fabrication process. For each sample, two consecutive measurement runs were performed, during increasing and decreasing temperature regimes. During the first measurement run, a strong recovery of the thermal diffusivity was observed, linked to the annealing of auto-irradiation damage. The second measurement run, results immediately after the previous, did not show any change in thermal diffusivity, proving that no significant change of stoichiometry occurred. The second run was used to confirm the final value of the thermal diffusivity after annealing.

The thermal diffusivity for the AM10 sample was found higher than for the AM20 sample, both during annealing, as well as after annealing. The experimental data are listed in table 4.6 and 4.7 and shown together in figure 4.4.

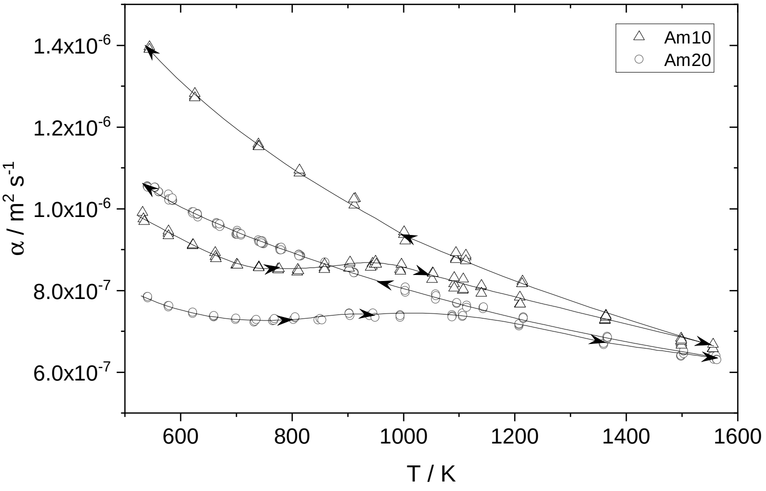

Figure 4.4: Thermal diffusivity of the (U,Am)O_{2-x} samples measured in this study.

4.3.3. Determination of thermal conductivity

The thermal conductivity (λ) was deduced from the measured thermal diffusivity (α), specific heat capacity (C_p) and density (ρ) according to equation 4.4.

$$\lambda = \alpha \cdot \rho \cdot C_p \tag{4.4}$$

The heat capacity of the AM10 and AM20 samples were obtained from equations 4.2 and 4.3. The thermal conductivity was converted to 95 % TD using the formula

Table 4.6: Thermal diffusivity values of the AM10 sample.

T_m / K	α / $m^2 \cdot s^{-1}$	T_m / K	α / $m^2 \cdot s^{-1}$	T_m / K	α / $m^2 \cdot s^{-1}$
On heating		941.4	8.56 x 10^{-7}	1498.6	6.75 x 10^{-7}
532.0	9.91 x 10^{-7}	948.3	8.64 x 10^{-7}	1499.0	6.79 x 10^{-7}
533.7	9.75 x 10^{-7}	950.3	8.72 x 10^{-7}	1363.6	7.39 x 10^{-7}
535.2	9.68 x 10^{-7}	951.5	8.64 x 10^{-7}	1363.5	7.34 x 10^{-7}
578.7	9.40 x 10^{-7}	993.9	8.51 x 10^{-7}	1363.4	7.37 x 10^{-7}
578.2	9.45 x 10^{-7}	995.2	8.47 x 10^{-7}	1213.4	8.17 x 10^{-7}
578.5	9.33 x 10^{-7}	996.2	8.64 x 10^{-7}	1213.3	8.23 x 10^{-7}
621.9	9.10 x 10^{-7}	1051.3	8.27 x 10^{-7}	1213.2	8.16 x 10^{-7}
622.2	9.12 x 10^{-7}	1052.7	8.43 x 10^{-7}	1094.2	8.79 x 10^{-7}
622.9	9.12 x 10^{-7}	1053.1	8.41 x 10^{-7}	1094.2	8.75 x 10^{-7}
662.1	8.92 x 10^{-7}	1106.3	8.00 x 10^{-7}	1094.2	8.92 x 10^{-7}
663.3	8.83 x 10^{-7}	1107.1	8.02 x 10^{-7}	1112.1	8.82 x 10^{-7}
663.7	8.78 x 10^{-7}	1107.7	8.28 x 10^{-7}	1112.0	8.86 x 10^{-7}
700.4	8.62 x 10^{-7}	1091.2	8.17 x 10^{-7}	1112.0	8.73 x 10^{-7}
701.1	8.64 x 10^{-7}	1091.2	8.31 x 10^{-7}	1003.7	9.21 x 10^{-7}
702.2	8.62 x 10^{-7}	1091.5	8.06 x 10^{-7}	1001.5	9.37 x 10^{-7}
740.8	8.58 x 10^{-7}	1139.5	8.09 x 10^{-7}	1000.9	9.44 x 10^{-7}
740.7	8.57 x 10^{-7}	1139.9	8.12 x 10^{-7}	913.5	1.03 x 10^{-6}
740.7	8.55 x 10^{-7}	1140.2	7.93 x 10^{-7}	911.9	1.01 x 10^{-6}
774.6	8.52 x 10^{-7}	1208.8	7.67 x 10^{-7}	911.1	1.02 x 10^{-6}
775.8	8.51 x 10^{-7}	1209.4	7.84 x 10^{-7}	815.3	1.09 x 10^{-6}
776.8	8.53 x 10^{-7}	1209.7	7.66 x 10^{-7}	813.5	1.09 x 10^{-6}
809.5	8.45 x 10^{-7}	1361.5	7.27 x 10^{-7}	813.4	1.09 x 10^{-6}
810.3	8.51 x 10^{-7}	1361.7	7.27 x 10^{-7}	739.8	1.16 x 10^{-6}
811.9	8.48 x 10^{-7}	1361.9	7.29 x 10^{-7}	740.0	1.15 x 10^{-6}
858.7	8.56 x 10^{-7}	1498.3	6.75 x 10^{-7}	740.2	1.15 x 10^{-6}
858.5	8.64 x 10^{-7}	1499.0	6.71 x 10^{-7}	625.6	1.28 x 10^{-6}
858.6	8.52 x 10^{-7}	1499.0	6.66 x 10^{-7}	625.6	1.28 x 10^{-6}
902.4	8.54 x 10^{-7}	1555.1	6.58 x 10^{-7}	625.6	1.27 x 10^{-6}
903.3	8.65 x 10^{-7}	1555.6	6.57 x 10^{-7}	544.4	1.39 x 10^{-6}
904.3	8.70 x 10^{-7}	1555.8	6.69 x 10^{-7}	544.1	1.40 x 10^{-6}
944.4	8.67 x 10^{-7}	On cooling		543.9	1.39 x 10^{-6}
944.1	8.59 x 10^{-7}	1498.1	6.84 x 10^{-7}		

Table 4.7: Thermal diffusivity values of the AM20 sample.

T_m / K	α / $m^2 \cdot s^{-1}$	T_m / K	α / $m^2 \cdot s^{-1}$	T_m / K	α / $m^2 \cdot s^{-1}$
On heating		1498.5	6.41 x 10^{-7}	748.9	9.14 x 10^{-7}
540.6	7.85 x 10^{-7}	1553.1	6.40 x 10^{-7}	747.5	9.14 x 10^{-7}
541.2	7.82 x 10^{-7}	1554.8	6.38 x 10^{-7}	746.3	9.21 x 10^{-7}
541.4	7.84 x 10^{-7}	1557.3	6.31 x 10^{-7}	745.6	9.16 x 10^{-7}
577.8	7.62 x 10^{-7}	On cooling		745.2	9.20 x 10^{-7}
578.3	7.60 x 10^{-7}	1563.0	6.30 x 10^{-7}	744.9	9.16 x 10^{-7}
578.7	7.63 x 10^{-7}	1562.0	6.31 x 10^{-7}	741.7	9.20 x 10^{-7}
621.5	7.43 x 10^{-7}	1561.3	6.40 x 10^{-7}	740.8	9.19 x 10^{-7}
621.6	7.47 x 10^{-7}	1503.1	6.52 x 10^{-7}	740.0	9.23 x 10^{-7}
621.9	7.47 x 10^{-7}	1502.9	6.51 x 10^{-7}	708.9	9.38 x 10^{-7}
660.2	7.35 x 10^{-7}	1502.8	6.45 x 10^{-7}	708.7	9.35 x 10^{-7}
659.3	7.36 x 10^{-7}	1366.2	6.85 x 10^{-7}	708.4	9.36 x 10^{-7}
660.0	7.38 x 10^{-7}	1366.1	6.84 x 10^{-7}	702.7	9.41 x 10^{-7}
698.6	7.28 x 10^{-7}	1366.0	6.82 x 10^{-7}	701.9	9.37 x 10^{-7}
698.8	7.28 x 10^{-7}	1366.0	6.81 x 10^{-7}	701.8	9.42 x 10^{-7}
699.1	7.32 x 10^{-7}	1366.0	6.87 x 10^{-7}	701.4	9.46 x 10^{-7}
732.2	7.23 x 10^{-7}	1365.7	6.87 x 10^{-7}	700.8	9.37 x 10^{-7}
733.2	7.24 x 10^{-7}	1215.5	7.35 x 10^{-7}	699.7	9.37 x 10^{-7}
736.0	7.29 x 10^{-7}	1215.3	7.30 x 10^{-7}	671.2	9.58 x 10^{-7}
765.4	7.26 x 10^{-7}	1215.1	7.32 x 10^{-7}	670.8	9.56 x 10^{-7}
767.4	7.26 x 10^{-7}	1144.0	7.59 x 10^{-7}	670.2	9.62 x 10^{-7}
768.6	7.31 x 10^{-7}	1143.3	7.55 x 10^{-7}	664.9	9.64 x 10^{-7}
802.2	7.29 x 10^{-7}	1142.9	7.58 x 10^{-7}	664.6	9.66 x 10^{-7}
805.7	7.33 x 10^{-7}	1113.5	7.63 x 10^{-7}	664.4	9.61 x 10^{-7}
806.0	7.35 x 10^{-7}	1113.4	7.58 x 10^{-7}	630.8	9.79 x 10^{-7}
846.9	7.28 x 10^{-7}	1095.5	7.68 x 10^{-7}	630.7	9.86 x 10^{-7}
850.8	7.31 x 10^{-7}	1095.5	7.70 x 10^{-7}	630.6	9.85 x 10^{-7}
853.7	7.28 x 10^{-7}	1058.3	7.87 x 10^{-7}	630.4	9.88 x 10^{-7}
903.8	7.38 x 10^{-7}	1058.1	7.79 x 10^{-7}	630.4	9.86 x 10^{-7}
903.0	7.44 x 10^{-7}	1057.8	7.91 x 10^{-7}	629.9	9.87 x 10^{-7}
902.7	7.43 x 10^{-7}	1003.8	7.95 x 10^{-7}	623.0	9.92 x 10^{-7}
939.0	7.38 x 10^{-7}	1003.1	8.07 x 10^{-7}	622.2	9.89 x 10^{-7}
945.5	7.45 x 10^{-7}	1002.6	8.00 x 10^{-7}	621.1	9.92 x 10^{-7}
948.9	7.34 x 10^{-7}	912.1	8.44 x 10^{-7}	585.8	1.02 x 10^{-6}
993.9	7.33 x 10^{-7}	911.6	8.43 x 10^{-7}	585.6	1.02 x 10^{-6}
994.5	7.40 x 10^{-7}	911.0	8.42 x 10^{-7}	585.3	1.03 x 10^{-6}
994.2	7.38 x 10^{-7}	859.5	8.69 x 10^{-7}	579.7	1.02 x 10^{-6}
1106.2	7.36 x 10^{-7}	858.8	8.65 x 10^{-7}	579.4	1.02 x 10^{-6}
1106.2	7.44 x 10^{-7}	858.5	8.58 x 10^{-7}	579.2	1.02 x 10^{-6}
1106.5	7.38 x 10^{-7}	815.9	8.85 x 10^{-7}	579.1	1.02 x 10^{-6}
1087.5	7.40 x 10^{-7}	815.6	8.84 x 10^{-7}	579.0	1.02 x 10^{-6}
1087.9	7.37 x 10^{-7}	814.8	8.84 x 10^{-7}	578.6	1.03 x 10^{-6}
1087.5	7.35 x 10^{-7}	812.4	8.88 x 10^{-7}	561.3	1.04 x 10^{-6}
1207.2	7.12 x 10^{-7}	812.4	8.84 x 10^{-7}	560.8	1.04 x 10^{-6}
1207.2	7.16 x 10^{-7}	811.9	8.87 x 10^{-7}	554.0	1.05 x 10^{-6}
1207.5	7.18 x 10^{-7}	782.0	9.00 x 10^{-7}	553.9	1.05 x 10^{-6}
1359.1	6.69 x 10^{-7}	781.1	9.05 x 10^{-7}	553.6	1.05 x 10^{-6}
1359.4	6.67 x 10^{-7}	780.4	8.99 x 10^{-7}	540.9	1.05 x 10^{-6}
1359.4	6.70 x 10^{-7}	779.2	9.04 x 10^{-7}	540.6	1.05 x 10^{-6}
1497.6	6.40 x 10^{-7}	778.6	8.99 x 10^{-7}	540.5	1.06 x 10^{-6}
1498.0	6.39 x 10^{-7}	777.8	9.04 x 10^{-7}		

of Brandt and Neuer as recommended by Fink [16] for UO_2 which is highly suited for polycrystalline ceramics. Taking into account the relative uncertainties on the thermal diffusivity (5 %), specific heat (4 %) and density (3 %), the relative uncertainty on the thermal conductivity over the whole temperature range is about 12 %.

As observed for the thermal diffusivity, the thermal conductivity for the AM10 sample was found higher than for the AM20 sample, both during annealing, as well as after annealing. The thermal conductivity curve obtained during annealing is typical for the recovery of radiation damage occurring as the measurement temperature increases, with a thermal conductivity increasing with temperature in the range from 800 to 950 K. As noted above the recovery of auto-irradiation damage compensates the decrease of thermal conductivity linked to the increase of phonon scattering when the temperature increases. During this annealing, the concentration of auto-irradiation created point defects present in the sample decreases progressively.

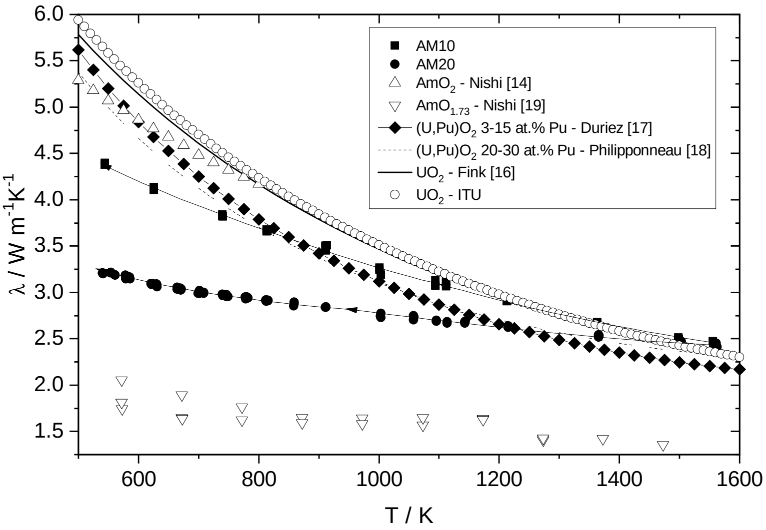

Figure 4.5: Thermal conductivity of the $(U,Am)O_{2-x}$ samples obtained in this study and literature data.

The thermal conductivity results obtained for $(U,Am)O_{2-x}$ after recovery of auto-irradiation damage can be represented by the equations:

$$\lambda_{AM10} = \frac{1}{0.12829 + 0.17901 \cdot 10^{-3} \cdot T} \tag{4.5}$$

$$\lambda_{AM20} = \frac{1}{0.26304 + 0.97229 \cdot 10^{-4} \cdot T} \tag{4.6}$$

The results are compared to literature data for UO_2, $(U,Pu)O_2$ and AmO_2 in figure 4.5. The comparison to UO_2 and $(U,Pu)O_2$ is intended to obtain information on the effect of the Am addition on the thermal conductivity, as this was extensively investigated in the literature for $(U, Pu)O_2$. For UO_2, the recommendation of Fink [16] was used. For $(U, Pu)O_2$, two recommendations were used, depending on the Pu content range: Duriez [17] recommended a single curve for 3 to 15 wt.% Pu and Philipponneau [18] recommended a single curve for 20 to 30 wt.% Pu. For stoichiometric UO_2, a very good agreement is found with the recommendation of Fink and our results, showing that the UO_2 samples remain stoichiometric under the measurement conditions. The data of Nishi *et al.* for AmO_{2-x} [19] and AmO_2 [14] are also shown.

At low temperatures, the AM10 and AM20 samples have a lower thermal conductivity than UO_2, and the values converge at high temperatures. Comparing the values after annealing to pure UO_2 shows that the reduction in thermal conductivity at low temperatures increases almost proportionally to the concentration of Am in the samples, with a decrease of about 20 % for the AM10 sample and about 40 % for the AM20 sample.

For stoichiometric samples, the two recommendations for $(U,Pu)O_2$ give very similar results, while our measurements show a clear difference between the AM10 and AM20 samples. The impact on the thermal conductivity of the introduction of Am in UO_2 is therefore much stronger than for the introduction of Pu. The temperature dependence of the thermal conductivity of the $(U,Am)O_{2-x}$ samples is weaker than for UO_2 and $(U,Pu)O_2$, and the values are lower at low temperatures, and slightly higher at high temperatures. The behaviour at high temperatures can be explained by the higher value of the specific heat of $(U,Am)O_{2-x}$ when compared to UO_2 (figure 4.3) and $(U,Pu)O_2$. At low temperatures, the thermal conductivity of AM20 (figure 4.5) is lower than the recommendations of Duriez and Philipponneau. In the case of AM10 (figure 4.5), the curve follows that of $(U,Pu)O_2$ only in the temperature range from 700 to 1100 K. A reduced temperature dependence of the thermal conductivity was also observed by Nishi for AmO_{2-x}. The thermal conductivity of Nishi for stoichiometric AmO_2 (figure 4.5) is available only in the temperature range from 500 to 800 K. It is higher than our results for AM10, and is close to the $(U,Pu)O_2$ thermal conductivity.

The results obtained in this study are compared (figure 4.6) with current theoretical models to determine if the data are qualitatively consistent with theory. The theoretical model used for this calculation is that presented by Gibby [20], where the thermal conductivity (λ) is represented, in equation 4.7, by the inverted sum of intrinsic lattice thermal resistance ($R_u \cdot T$) which results from phonon-phonon interaction and the thermal resistance (R_i) resulting from phonon-lattice defect interactions.

$$\lambda = \frac{1}{R_i + R_u \cdot T} \tag{4.7}$$

The intrinsic thermal resistance is temperature dependent and can be estimated from basic material properties starting from the Leibfried-Schlömann [21] equation as described in Gibby's paper, obtaining equation 4.8 where X_{AmO_2} and X_{UO_2} are the atomic fractions, a_{AmO_2} and a_{UO_2} represents the lattice parameters and T_{M_1} and T_{M_2} are the melting temperatures of AmO_2 and UO_2, respectively.

$$R_u = \frac{4.4 \cdot 10^{-9} \cdot (X_{AmO_2} \cdot a_{AmO_2} + X_{UO_2} \cdot a_{UO_2}) \cdot (T_{M_1} \cdot X_{AmO_2} + T_{M_2} \cdot X_{UO_2})^{3/2}}{17} \tag{4.8}$$

The meaning of the symbols in this and subsequent equations is explained in table 4.8.

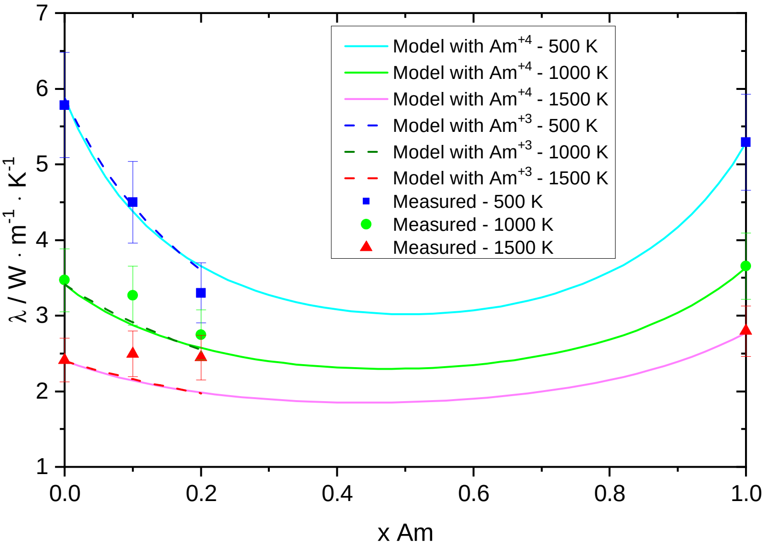

Figure 4.6: Thermal conductivity of (U, Am)O_{2-x} solid solutions as a function of AmO_2 content compared with the theoretical model, corrected for 95 % TD.

The contribution to the thermal resistance of the system is due to the point defects, represented by americium atoms substituted for uranium in a UO_2 lattice, which may interact with phonons. The contribution from lattice defects can be estimated by the following equation:

$$R_i = R_0 + Y \cdot \Gamma \tag{4.9}$$

where R_0 accounts for the thermal resistance resulting from defects caused by impurities (equation 4.10) and $Y \cdot \Gamma$ represents the magnitude of the strain generated in the lattice. Γ describes the scattering cross-section parameter (equation 4.11) where η is an empirical factor, r_{Am} and r_U are the atomic radii for americium and uranium and X_{AmO_2} and X_{UO_2} are the corresponding atomic fractions. In this approach the charge states of uranium and americium are +4.

$$R_0 = 0.1035 \cdot X_{AmO_2} + 0.047 \cdot X_{UO_2} \tag{4.10}$$

$$\Gamma = \frac{X_{AmO_2} \cdot X_{UO_2} \cdot \eta \cdot (r_U - r_{Am})^2}{(X_{AmO_2} \cdot r_{Am} + X_{UO_2} \cdot r_U)^2} \tag{4.11}$$

The value of Y in equation 4.12 is calculated using the following parameters: the adjustable factor (η), an average atomic volume calculated from lattice parameter data ($\bar{V}_0$), the Debye temperature (θ_D), the average phonon velocity (C) and Planck's constant (h).

$$Y = \frac{\eta \cdot \pi^2 \cdot \bar{V}_0 \cdot \theta_D}{3 \cdot C^2 \cdot h} \tag{4.12}$$

Table 4.8: Meaning of the symbols used in the equations which describes the theoretical model.

Symbol	Value	Units	Reference
a_{Am}	5.37	Å	Hurtgen [23] and Chikalla [24]
a_U	5.46	Å	Lebreton *et al.* [25]
T_{M_1}	2448	K	Zhang *et al.* [26]
T_{M_2}	3120	K	Manara *et al.* [27]
η	55	-	-
r_{Am}	9.90 x 10^{-11}	m	Shannon [28]
r_U	1.03 x 10^{-10}	m	Shannon [28]
$\bar{V}_0$	1.36 x 10^{-29}	m^3	Gibby *et al.* [20]
C	4.00 x 10^{+3}	$m \cdot s^{-1}$	Gibby *et al.* [20]
h	6.63 x 10^{-34}	$m^2 \cdot kg \cdot s^{-1}$	-
θ_{AmO_2}	335	K	Lu *et al.* [29]
θ_{UO_2}	398	K	Lu *et al.* [29]

The Debye temperature (θ_D) is assumed to vary linearly with the composition and was calculated using equation 4.13 where θ_{AmO_2} and θ_{UO_2} are the Debye temperatures of the end members of the analyzed system.

$$\theta_D = X_{AmO_2} \cdot \theta_{AmO_2} + X_{UO_2} \cdot \theta_{UO_2} \tag{4.13}$$

Using equation 4.7, the thermal conductivity of (U,Am)O_{2-x} solid solutions was calculated for three different temperatures (500 K, 1000 K and 1500 K). Those computed values are compared with the experimental results in figure 4.6 where the thermal conductivity is shown as a function of americium content. Even if the experimental results at 1500 K are a bit higher than the computed values, equation 4.7 appears to predict the effect of americium content on the thermal conductivity correctly.

The proposed model considers that both uranium and americium have a charge state of +4. XANES measurements on the fabricated samples performed at room temperature showed, however, that the Am valence is closer to +3 [1]. Also Prieur *et al.* have shown that for 15 mol % of Am in (U,Am)O_2, the charge state of Am was +3, with an equal mole fraction of uranium with the charge state +5, ensuring electroneutrality [30]. For that reason we also used the above model with Am^{3+} and U^{5+}, as shown as dashed lines in figure 4.6. In that case all coefficients were assumed to be the same except the atomic radii for americium and uranium ($r_{Am^{3+}}$= 1.12 x 10^{-10} m and $r_{U^{5+}}$= 9.00 x 10^{-11} m), yielding η =13 in equations 4.11 and 4.12, which is significantly lower than for the Am^{4+} case, η= 55.

4.4. Summary

New enthalpy increment values of the $U_{0.9123}Am_{0.0877}O_{2-x}$ and $U_{0.8105}Am_{0.1895}O_{2-x}$ intermediate compositions were reported in this study. Based on the comparison to the enthalpy increments of the pure compounds, no excess contributions were revealed by this study. The experimental values were used for deriving heat capacity functions of the solutions which were correlated with the thermodynamic properties of the end members and indicate no substantial deviation from the Neumann-Kopp's molar additivity rule.

Further, the thermal diffusivity was measured in order to calculate the thermal conductivity. It was observed that the americium concentration has a strong effect on the thermal diffusivity of the uranium-americium mixed oxide. The results show a clear difference between the thermal conductivity of the AM10 and AM20 samples and the temperature dependence of the $(U_{1-y}Am_y)O_{2-x}$ solid solutions with y= 0.0877 and 0.1895 is weaker than for the end-members.

The thermal conductivity results show that this property decreases when Am is introduced in UO_2. Comparison with literature data shows that the impact on the thermal conductivity of the introduction of Am in UO_2 is much stronger than for the introduction of Pu. It can thus be concluded that the effect of the addition of Am can be described by the law of mixtures in case of the the heat capacity but not in case of the thermal diffusivity, because of the higher sensitivity of this transport property to the symmetry and periodicity of the lattice.

In future studies, the effect of composition in a wider range has to be explored further, as well as the effect of the synthesis method (sol-gel versus powder mixing) that may affect the homogeneity at the level of the crystal lattice. It is also mandatory to measure these thermal properties of the AmO_2 end member up to a higher temperature range to obtain a complete set of experimental thermodynamic data.

References

[1] M. Vespa, M. Rini, J. Spino, T. Vitova, J. Somers, J. Nucl. Mater. 421 (2012) 80-88.

[2] D. Prieur, P.M. Martin, A.Jankowiak, E. Gavilan, A.C. Scheinost, N. Herlet, P. Dehaudt, P. Blanchart, Inorg. Chem. 50 (2011) 12437-12445.

[3] D. Prieur, F. Lebreton, P. M. Martin, A. Jankowiak, T. Delahaye, P. Dehaudt, P. Blanchart, J. Eur. Ceram. Soc. 32 (2012) 1585-1591.

[4] F. Lebreton, D. Horlait, T. Delahaye, P. Blanchart, J. Nucl. Mater. 439 (2013) 99-102.

[5] W. Bartscher, C. Sari, J. Nucl. Mater. 118 (1983) 220-223.

[6] C. Suzuki, T. Nishi, M. Nakada, T. Tsuru, M. Akabori, M. Hirata, Y. Kaji, J. Phys. Chem. Solids 74 (2013) 1769-1774.

[7] A. Fernandez, D. Haas, R.J.M. Konings, J. Somers, J. Am. Ceram. Soc. 83 (2002) 694-696.

[8] J. Somers, A. Fernandez, J. Am. Ceram. Soc. 88 (2005) 827-832.

[9] S. Aboushal, P. Van Belle, H. Ottmar, Nucl. Instrum. Methods Phys. Res., Sect. A: Spectrom. Detect. Assoc. Equip. 543 (2005) 608-618.

[10] O. Beneš, P. Gotcu-Freis, F. Schwörer, R.J.M. Konings, Th. Fanghänel, J. Chem. Thermodyn. 43 (2011) 651-655.

[11] O.S. Vălu, O. Beneš, R.J.M. Konings, H. Hein, J. Chem. Thermodyn. 68 (2014) 122-127.

[12] M. Sheindlin, D. Halton, M. Musella, C. Ronchi, Rev. Scient. Instr. 69(3) (1998) 1426-1436.

[13] R.J.M. Konings, O. Beneš, A. Kovács, D. Manara, D. Sedmidubský, L. Gorokhov, V.S. Iorish, V. Yungman, E. Shenyavskayan and E. Osina, The thermodynamic properties of the f-elements and their compounds. Part II. The Lanthanide and Actinide Oxides, J. Phys. Chem. Ref. Data, 43 (2014) 013101-1-013101-95.

[14] T. Nishi, A. Itoh, K. Ichise, Y. Arai, J. Nucl. Mater. 414 (2011) 109-113.

[15] D. Prieur, P.M. Martin, F. Lebreton, T. Delahaye, A. Jankowiak, J.-P. Laval, A.C. Scheinost, P. Dehaudt, P. Blanchart, J. Solid State Chem. 194 (2012) 206-211.

[16] J.K. Fink, J. Nucl. Mater. 279 (2000) 1-18.

[17] C. Duriez, J.P. Alessandri, T. Gervais, Y. Philipponneau, J. Nucl. Mater. 277 (2000) 143-158.

[18] Y. Philipponneau, J. Nucl. Mater. 188 (1992) 194-197.

[19] T. Nishi, M. Takano, A. Itoh, M. Akabori, Y. Arai, J. Nucl. Mater. 373 (2008) 295-298.

[20] R.L. Gibby, J. Nucl. Mater. 38 (1971) 163-177.

[21] G. Leibfried and E. Schlömann, Akad. Wiss. Gottingen, Math.-Physik. KI II-a (1954) 71.

[22] D. Prieur, *Elaboration de combustible à base d'oxydes d'uranium et d'américium: modélisation thermodynamique et propriétés des matériaux*. Thèse de doctorat: matériaux céramiques et traitements de surface, Université de Limoges, 2011.

[23] C. Hurtgen, J. Fuger, Inorg. Nucl. Chem. Lett. 13 (1977) 179-188.

[24] T.D. Chikalla, L.J. Eyring, J. Inorg. Nucl. Chem. 30 (1968) 133-145.

[25] F. Lebreton, R.C. Belin, D. Prieur, T. Delahaye, P. Blanchart, Inorg. Chem. 51 (2012) 9369-9375.

[26] H. Zhang, R.J.M. Konings, M.E. Huntelaar, E.H.P. Cordfunke, J. Nucl. Mater. 250 (1997) 88-95.

[27] D. Manara, C. Ronchi, M. Sheindlin, M. Lewis, M. Brykin, J. Nucl. Mater. 342 (2005) 148-163.

[28] R.D. Shannon, Acta Cryst. A32 (1976) 751.

[29] Y. Lu, Y. Yang, F. Zheng, B.-T. Wanga, P. Zhang, J. Nucl. Mater. 441 (2013) 411-420.

[30] D. Prieur, P. Martin, F. Lebreton, T. Delahaye, D. Banerjee, A.C. Scheinost, A. Jankowiak, J. Nucl. Mater. 434 (2013) 7-16.

5

The low-temperature heat capacity of $(U_{1-y}Am_y)O_{2-x}$ for y= 0.08 and 0.20

The low-temperature heat capacity of $(U_{1-y},Am_y)O_{2-x}$ solid solution with y= 0.0811 and 0.2005 and x= 0.01-0.03 was determined from a minimum of 12.52 K up to 297.1 K and from 9.77 K up to 302.3 K, respectively, using hybrid adiabatic relaxation calorimtry. The low temperature heat capacity results of the investigated system revealed the absence of the magnetic transition specific for UO_2 in the temperature region of 30 K. Since there are no experimental data available for AmO_2 in this temperature region, the results obtained for the intermediate compositions are validated based on the experimental data of UO_2 end-member and the low-temperature heat capacity computation of AmO_2. In the measured temperature interval, excess heat capacity was observed for the two investigated intermediate compositions, which is concluded to be dominated by self-radiation effects at very low temperature.

This chapter is reprinted with kind permission of Elsevier: *The low-temperature heat capacity of* $(U_{1-y}Am_y)O_{2-x}$ *for y = 0.08 and 0.20. O.S. Vălu, O. Beneš, J.-C. Griveau, E. Colineau, R.J.M. Konings. Journal of Nuclear Materials 507 (2018) 126-134.*

5.1. Introduction

The heat capacity, which describes the relation between the heat and temperature of a material, reveals essential information about phase transitions, lattice vibrations, energy excitations and electronic properties of materials. Many thermodynamic studies have been performed on the actinide oxides, but data on heat capacity variation of the mixed oxides solid solution are limited. The experimental deduced thermophysical properties of such complex nuclear materials are necessary for predicting the behaviour of a possible usage as fuel but also for management purposes. Our interest is aimed at the fluorite-type cubic solid solutions of the actinide dioxides and in one of our previous study [1] the heat capacity of the uranium-americium mixed oxide system was investigated in the high temperature range (425-1790 K). In the present work we have focused our investigations on the low-temperature interval and measured the heat capacity of the considered solid solutions. We have measured the heat capacity of (U,Am)O_{2-x} solid solutions with 10 and 20 wt.% AmO_2 in the temperature range from a minimum of 9.77 K to about 300 K using the Quantum Design PPMS. We would like to investigate whether the system behaves similar as (Th,Pu)O_2 studied by us previously [2]. In that system the valence of the cations Th^{4+} and Pu^{4+} in the lattice is identical, in the case of the (U,Am)O_{2-x} system the mixture of the U^{4+}, U^{5+}, Am^{4+} and Am^{3+} cations has to be considered [3].

Moreover, the radioactivity of plutonium is significantly lower and the self-irradiation process does not influence the results as much as americium. Americium is a powerful α emitter, which means that energy is propagated into the environment but also into the material itself creating displacements of the atoms in the lattice. Most of the energy of an α particle emitted is lost by the interaction with electrons and just 1% of the energy is dissipated by elastic collisions which is enough to cause atomic displacements. The high α activity of ^{241}Am induces the self-irradiation of the material that leads to material properties changes. Self-irradiation damage by α-decay process has been reported for $^{241}AmO_2$ [4] but also for (U,Am)O_{2-x} [5–7]. As first effects of self-irradiation, an increase of the lattice distances and presence of helium bubbles have been observed, reflected in numerous properties changes. Taking into account that the lattice parameter expansion of AmO_2 evolves to a maximum in about 100 days [4], and it reaches the half value in just 15 days, the probability that a sample is affected by defects in the lattice is almost a certitude. Even if our samples contain less than 20 % americium a very high specific α activity is present. Thus, two mechanisms, disorder from substitution and self-irradiation, may cause that the heat capacity of the (U,Am)O_{2-x} solid solutions materials may deviate from the trend induced by the end-members and show an excess contribution.

5.2. Experimental work

5.2.1. Sample preparation

The heat capacity measurements performed in this study were done on samples with different AmO_2 concentrations. (U,Am)O_{2-x} targets were prepared with two ^{241}Am

Table 5.1: $(U,Am)O_{2-x}$ notations, compositions and fabrication data.

Notation	Nominal composition Am/(U+Am)(mol%)	Actual composition[a] Am/(U+Am)(mol%)	Sintering under Ar/H_2	Oxygen potential kJ/mol	Disk density (% TD[b])
AM10	10	8.11 ± 0.63	1650°C, 8 h, 1500 ppm H_2O	-391	87
AM20	20	20.05 ± 0.82	1650°C, 24 h, 2400 ppm H_2O	-384	93

[a] *Composition measured by calorimetry [11];*

[b] *TD = theoretical density, determined from gravimetry and geometry.*

contents (8.11 and 20.05 mol%). Porous beads (in this case UO_2) were synthesised by a sol-gel process [8, 9] and then introduced into the Minor Actinide handling facility, where they were infiltrated with an Am solution. For this process uranium nitrate and americium dioxide were used as starting materials. Americium contained ca. 1 wt.% ^{237}Np as impurity from the decay which have no influence on our measurements. The sintering process of the $(U_{1-y},Am_y)O_2$ solid solutions with y= 0.0811 and 0.2005 was done under humidified Ar/H_2 (4% H_2) atmosphere at 1650 °C for 8 and 24 hours which correspond to oxygen potentials of -391 and -384 kJ/mol, respectively. The complete procedure is described in detail in our previous work [1] but also in study of Vespa *et al.* [10].

After production, the actual Am content was determined by a calorimetric method [11] measuring the decay heat of ^{241}Am, the results of which are provided in table 5.1. XANES and XRD experiments have been carried out for the O/M determination on uranium-americium oxides produced under the same conditions [10]. For our study, the powder X-ray diffraction analysis was performed before and after a heat treatment, for annealing purpose, the O/M was calculated and the values of the two compositions were found in the range 1.99-1.97. The notations defined in table 5.1 were used in the text and graphs.

5.2.2. Calorimetry

A PPMS-9 (Physical Property Measurement System, Quantum Design) instrument was used to determine the heat capacity of the two samples that had a relatively small mass (few mg). The technique is based on a hybrid adiabatic relaxation method, and is described in our previous work [2]. Details of our apparatus can be found in Javorský *et al.* [12].

The measurements of AM10 and AM20 samples were made on sample pieces which were wrapped in an appropriate amount of Stycast. Self-heating correction was taken into consideration and the heat capacity of corresponding Stycast amount was measured separately and subtracted, obtaining the uncertainty of the measurements to be 3-5 % for the lower temperature range ($T < 200$ K) and 5-10 % for the higher temperature region ($T > 200$ K).

For the current study, the heat capacity measurements were performed in two temperature ranges in order to reach the lowest temperature possible. For each composition, two samples were prepared with different weights. The materials have been annealed before being used, to remove radiation damage, into a furnace at about 1770

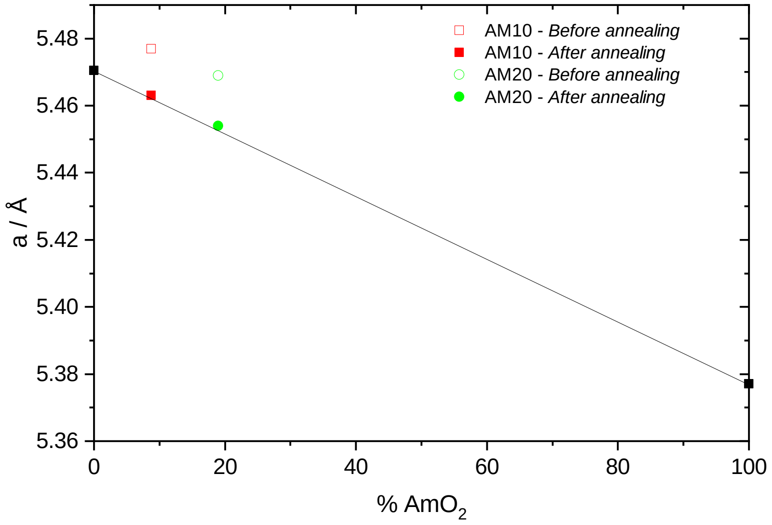

Figure 5.1: Plot of cell parameter values measured of the AM10 and AM20 samples before and after annealing, together with the unit cell parameter of UO_2 and AmO_2 from [13] and [14].

°C for 2 hours under helium gas flow. Cell parameters were obtained before and after the annealing and are shown in figure 5.1 together with end members cell parameters from [13] and [14].

For the very low temperature region a smaller sample was used in order to obtain the lowest value on the temperature scale in view of the self heating effect of Am. From about 30 K up to 300 K the quantity of material was almost doubled to improve the sensitivity of the measurement. In table 5.2 the weights of the sample used for this study are listed together with the temperature range that was covered for each composition.

5.3. Results

The low-temperature heat capacity of $(U_{1-y},Am_y)O_{2-x}$ solid solution with y= 0.0811 and 0.2005 and x= 0.01-0.03 are listed in tables 5.3, 5.4 and 5.5 and are shown in figure 5.2 together with the heat capacity of the UO_2 [17] and computed values for AmO_2. Since the heat capacity of AmO_2 has not been measured below 300 K, we estimated it from the lattice heat capacity of PuO_2, following the same approach presented in our previous study [2]. This implies that the heat capacity of AmO_2 can be described as being the sum of lattice heat capacity (C_{lat}), attributed mainly to the lattice vibrations, and the excess heat capacity (C_{exs}) resulted from the contribution of the 5f electron excitation caused by the crystal field splitting [15], as shown in equation 5.1.

$$C_p = C_{lat} + C_{exs} \tag{5.1}$$

The heat capacity of a mixed oxide material is strongly driven by the properties of the end-members of the solid solution. As can be seen in Figure 5.2 the results for the

Table 5.2: (U,Am)O_{2-x} compositions, weights and temperature intervals.

Composition	Temperature [K]	Weight [mg]
AM10	12.52 - 30.00	6.6
	30.00 - 297.07	13.0
AM20[a]	15.07 - 30.00	6.5
	30.00 - 302.33	22.3
AM20[b]	9.77 - 22.33	2.3

[a] *1st run;*
[b] *2nd run*

$(U_{1-y},Am_y)O_{2-x}$ solid solutions are systematically higher than the end members, except for the region of the magnetic transition in UO_2. From the calculated heat capacity of AmO_2 and the literature data of UO_2 it was possible to interpolate the heat capacity of the mixed oxide using the Neumann-Kopp rule [16], which is shown in figure 5.3 for the two intermediate compositions considered for this study, AM10 and AM20. We refer to the Neumann-Kopp rule because it is the most used technique for estimation of temperature dependence of the heat capacity of mixed oxides.

As previously observed for the (Th,Pu)O_2 fluorite solid solution [2] the excess heat capacity may be due to the cation substitution on the crystal lattice, leading to lattice strain. In the case of mixed uranium americium oxides the substitution is complicated by the presence of U^{5+} and Am^{3+}. XANES studies of the $(U_{1-y},Am_y)O_{2.00}$ solid solution have shown that americium is trivalent with an equal fraction of U^{5+} to keep the charge balanced [3]. This means that U^{4+} (ionic radius 100 pm in eight-coordinated cubic environment) is substituted by U^{5+} (90 pm) and Am^{3+} (109 pm), and not by Am^{4+} (95 pm). Although the average value of the radii is about similar to tat of U^{4+}, it means that the number of ions different from the host is twice the Am concentration, thus leading to a concomitant increase of the lattice stain. Finally lattice disorder, particularly on the anion sublattice, created by the alpha decay of americium [5–7] must be taken into account. These sources must be considered in the analysis of the present low-temperature heat capacity results.

5.3.1. *The low-temperature range (0<(T/K)<50)*

For this temperature interval the two sample compositions were measured down to 12.52 K for AM10 and 15.07 K for AM20. While for the AM10 sample one set of measurements was done, for the AM20 two series of experimental measurements were performed. The first set of results have been obtained from ambient temperature down to a minimum of 15.07 K. Couple of weeks later, in the attempt of lowering the measured temperature and after a new annealing of the material, a quantity of just 2.3 mg sample was successfully measured down to 9.77 K with a very good agreement with the first run

Table 5.3: Low temperature heat capacity values of $U_{0.9189}Am_{0.0811}O_{2-x}$ intermediate composition.

T_m / K	$C_P/(J \cdot mol^{-1} \cdot K^{-1})$	T_m / K	$C_P/(J \cdot mol^{-1} \cdot K^{-1})$	T_m / K	$C_P/(J \cdot mol^{-1} \cdot K^{-1})$	T_m / K	$C_P/(J \cdot mol^{-1} \cdot K^{-1})$	T_m / K	$C_P/(J \cdot mol^{-1} \cdot K^{-1})$
12.52	2.252	13.05	2.477	15.86	3.358	26.83	6.878	60.92	20.079
12.53	2.258	13.06	2.439	15.89	3.331	27.25	7.078	62.01	20.482
12.53	2.253	13.08	2.484	15.99	3.397	27.28	7.043	63.12	20.847
12.54	2.264	13.09	2.446	16.03	3.374	27.70	7.255	64.25	21.252
12.54	2.259	13.11	2.499	16.13	3.437	27.71	7.225	65.41	21.640
12.55	2.269	13.12	2.456	16.17	3.416	28.17	7.443	66.60	22.043
12.56	2.263	13.13	2.507	16.28	3.480	28.20	7.403	67.81	22.469
12.56	2.266	13.15	2.463	16.31	3.463	28.65	7.614	69.04	22.864
12.57	2.279	13.16	2.510	16.43	3.529	28.66	7.581	70.31	23.302
12.58	2.275	13.18	2.476	16.47	3.504	29.13	7.814	71.60	23.745
12.58	2.272	13.19	2.520	16.59	3.576	29.16	7.781	72.92	24.182
12.59	2.328	13.22	2.487	16.62	3.551	29.63	8.011	74.27	24.634
12.59	2.277	13.22	2.532	16.75	3.618	29.64	7.990	75.65	25.090
12.60	2.326	13.25	2.496	16.79	3.598	30.14	8.209	77.06	25.556
12.60	2.324	13.25	2.549	16.92	3.668	30.17	8.186	78.50	26.040
12.60	2.283	13.28	2.504	16.95	3.651	30.65	8.426	79.97	26.521
12.60	2.328	13.29	2.557	17.09	3.719	30.68	8.397	81.48	27.003
12.61	2.283	13.32	2.520	17.12	3.698	31.19	8.642	83.01	27.489
12.61	2.331	13.32	2.569	17.27	3.774	31.21	8.604	84.58	27.990
12.61	2.329	13.36	2.581	17.31	3.749	31.74	8.864	86.18	28.497
12.62	2.288	13.36	2.533	17.45	3.823	31.76	8.826	87.82	28.993
12.62	2.332	13.40	2.591	17.49	3.806	32.30	9.087	89.49	29.498
12.63	2.333	13.40	2.548	17.64	3.882	32.32	9.049	91.20	30.027
12.63	2.288	13.44	2.608	17.68	3.860	32.87	9.329	92.94	30.550
12.63	2.339	13.44	2.563	17.83	3.941	32.89	9.289	94.72	31.060
12.64	2.290	13.48	2.627	17.87	3.923	33.46	9.552	96.53	31.616
12.64	2.340	13.49	2.575	18.04	4.002	33.48	9.519	98.39	32.184
12.65	2.298	13.53	2.631	18.08	3.980	34.05	9.796	100.28	32.770
12.65	2.337	13.53	2.591	18.25	4.061	34.08	9.764	102.22	33.377
12.65	2.344	13.57	2.652	18.29	4.042	34.67	10.042	104.20	33.949
12.66	2.298	13.58	2.607	18.47	4.123	34.69	10.009	106.22	34.548
12.66	2.350	13.62	2.667	18.50	4.104	35.29	10.282	108.28	35.169
12.67	2.304	13.63	2.622	18.69	4.193	35.31	10.252	110.39	35.817
12.67	2.356	13.67	2.685	18.73	4.171	35.93	10.546	112.54	36.460
12.68	2.305	13.68	2.640	18.91	4.260	35.95	10.517	114.74	37.113
12.68	2.348	13.72	2.699	18.95	4.244	36.59	10.818	116.98	37.730
12.69	2.355	13.73	2.658	19.15	4.336	36.60	10.785	119.27	38.415
12.69	2.313	13.77	2.722	19.19	4.313	37.26	11.095	121.61	39.062
12.69	2.355	13.79	2.680	19.39	4.408	37.28	11.064	124.00	39.684
12.70	2.317	13.83	2.741	19.43	4.394	37.94	11.397	126.44	40.377
12.70	2.356	13.84	2.696	19.64	4.487	37.96	11.360	128.94	41.058
12.71	2.363	13.88	2.754	19.68	4.469	38.64	11.683	131.48	41.709
12.71	2.319	13.90	2.708	19.90	4.573	38.66	11.634	134.08	42.346
12.72	2.367	13.97	2.783	19.94	4.551	39.36	11.961	136.74	42.992
12.72	2.313	13.98	2.741	20.16	4.646	39.37	11.926	139.44	43.715
12.73	2.371	14.04	2.800	20.20	4.628	40.08	12.262	142.21	44.402
12.73	2.373	14.05	2.761	20.44	4.738	40.10	12.234	145.02	45.151
12.74	2.329	14.10	2.827	20.47	4.718	40.83	12.578	147.91	45.807
12.74	2.370	14.12	2.784	20.72	4.832	40.85	12.523	150.85	46.404
12.75	2.333	14.17	2.843	20.75	4.805	41.59	12.885	153.86	46.988
12.76	2.383	14.19	2.804	21.00	4.917	41.61	12.836	156.93	47.676
12.76	2.339	14.24	2.869	21.03	4.897	42.37	13.212	160.06	48.421
12.77	2.390	14.26	2.831	21.30	5.012	42.40	13.162	163.25	49.249
12.78	2.337	14.32	2.893	21.34	4.988	43.18	13.504	166.51	50.000
12.78	2.389	14.34	2.856	21.61	5.108	43.20	13.437	169.84	50.631
12.79	2.385	14.39	2.917	21.63	5.087	44.00	13.809	173.24	51.272
12.79	2.344	14.42	2.877	21.91	5.205	44.01	13.755	176.71	51.944
12.80	2.396	14.47	2.940	21.95	5.187	44.84	14.147	180.25	52.641
12.81	2.349	14.50	2.907	22.24	5.323	44.84	14.095	183.87	53.302
12.82	2.403	14.56	2.973	22.26	5.294	45.69	14.439	187.56	53.875
12.83	2.358	14.58	2.934	22.56	5.432	45.70	14.470	191.34	54.534
12.83	2.405	14.65	2.996	22.60	5.412	46.57	14.801	195.18	55.351
12.84	2.362	14.67	2.959	22.91	5.548	46.57	14.756	199.10	56.101
12.84	2.408	14.74	3.028	22.93	5.524	47.45	15.096	203.12	56.749
12.86	2.415	14.76	2.992	23.24	5.663	47.45	15.132	207.20	57.437
12.86	2.366	14.83	3.057	23.28	5.635	48.36	15.457	211.38	57.981
12.87	2.423	14.86	3.023	23.61	5.789	48.36	15.405	215.64	58.678
12.88	2.370	14.93	3.087	23.62	5.760	49.28	15.793	219.98	59.376
12.89	2.424	14.96	3.052	23.96	5.907	49.29	15.750	224.42	60.010
12.90	2.384	15.03	3.115	24.01	5.890	50.23	16.152	228.94	60.580
12.91	2.432	15.06	3.079	24.36	6.051	–	–	233.55	61.097
12.92	2.391	15.13	3.148	24.37	6.011	49.61	15.937	238.29	61.660
12.93	2.434	15.17	3.115	24.72	6.176	50.44	16.242	243.10	62.278
12.94	2.397	15.24	3.176	24.76	6.149	51.29	16.560	248.01	62.913
12.94	2.440	15.27	3.146	25.13	6.321	52.16	16.889	253.02	63.452
12.96	2.405	15.36	3.218	25.14	6.278	53.05	17.214	258.14	63.772
12.97	2.449	15.39	3.183	25.52	6.447	53.95	17.538	263.37	64.335
12.99	2.458	15.48	3.245	25.57	6.429	54.88	17.883	268.70	64.737
12.99	2.409	15.51	3.218	25.95	6.564	55.84	18.221	274.14	65.121
13.01	2.467	15.60	3.283	25.95	6.590	56.80	18.578	279.69	65.519
13.01	2.415	15.63	3.251	26.36	6.745	57.80	18.942	285.11	65.739
13.03	2.471	15.73	3.317	26.40	6.718	58.82	19.313	290.92	66.300
13.04	2.426	15.76	3.291	26.80	6.902	59.86	19.687	297.07	67.320

Table 5.4: Low temperature heat capacity values of $U_{0.7995}Am_{0.2005}O_{2-x}$ intermediate composition, from the first run.

T_m / K	$C_P/(J \cdot mol^{-1} \cdot K^{-1})$	T_m / K	$C_P/(J \cdot mol^{-1} \cdot K^{-1})$	T_m / K	$C_P/(J \cdot mol^{-1} \cdot K^{-1})$	T_m / K	$C_P/(J \cdot mol^{-1} \cdot K^{-1})$	T_m / K	$C_P/(J \cdot mol^{-1} \cdot K^{-1})$
15.07	2.078	16.06	2.308	21.01	3.729	38.03	10.526	95.65	30.056
15.09	2.075	16.09	2.317	21.04	3.738	38.08	10.523	97.32	30.571
15.09	2.079	16.12	2.313	21.22	3.799	38.65	10.753	99.03	31.069
15.10	2.079	16.14	2.324	21.43	3.863	39.15	10.929	100.77	31.635
15.10	2.081	16.18	2.336	21.44	3.870	39.27	11.012	102.55	32.175
15.11	2.079	16.19	2.343	21.67	3.950	39.91	11.257	104.36	32.685
15.12	2.076	16.24	2.349	21.84	3.996	40.26	11.374	106.19	33.203
15.12	2.089	16.25	2.351	21.91	4.026	40.57	11.519	108.09	33.661
15.12	2.083	16.29	2.362	22.15	4.109	41.23	11.786	110.00	34.208
15.13	2.090	16.34	2.374	22.28	4.148	41.42	11.844	111.95	34.779
15.14	2.087	16.35	2.374	22.39	4.202	41.90	12.050	113.94	35.375
15.14	2.094	16.41	2.389	22.66	4.303	42.57	12.299	115.97	35.911
15.15	2.093	16.45	2.402	22.70	4.303	42.64	12.292	118.04	36.473
15.16	2.099	16.47	2.399	22.91	4.397	43.28	12.559	120.15	37.039
15.16	2.095	16.54	2.419	23.18	4.498	43.88	12.749	122.29	37.549
15.18	2.097	16.56	2.430	23.18	4.485	44.00	12.836	124.39	38.143
15.18	2.103	16.60	2.436	23.45	4.597	44.72	13.116	126.62	38.749
15.19	2.097	16.67	2.452	23.64	4.645	45.17	13.239	128.88	39.333
15.20	2.105	16.68	2.456	23.74	4.698	45.47	13.416	131.20	39.901
15.21	2.107	16.74	2.472	24.03	4.803	46.23	13.727	133.56	40.482
15.21	2.107	16.81	2.490	24.16	4.840	46.52	13.809	135.96	41.026
15.23	2.114	16.82	2.492	24.33	4.914	47.00	14.029	138.41	41.713
15.23	2.113	16.89	2.509	24.64	5.044	47.79	14.313	140.91	42.380
15.24	2.110	16.94	2.528	24.69	5.039	47.90	14.308	143.45	42.926
15.25	2.114	16.98	2.528	24.93	5.157	48.60	14.635	146.04	43.560
15.26	2.120	17.06	2.553	25.26	5.276	49.33	14.864	148.69	44.010
15.27	2.112	17.08	2.564	25.28	5.285	49.42	14.929	151.38	44.638
15.28	2.118	17.15	2.576	25.58	5.405	50.26	15.275	154.13	45.229
15.29	2.129	17.24	2.594	25.81	5.471	–	–	156.92	45.860
15.30	2.128	17.24	2.609	25.96	5.551	49.35	14.881	159.76	46.513
15.32	2.128	17.33	2.626	26.25	5.663	50.11	15.179	162.66	47.091
15.32	2.134	17.40	2.651	26.43	5.717	50.91	15.476	165.62	47.653
15.33	2.134	17.43	2.652	26.62	5.799	51.72	15.790	168.63	48.221
15.35	2.147	17.52	2.677	26.97	5.935	52.53	16.087	171.69	48.777
15.36	2.140	17.58	2.690	27.06	5.953	53.36	16.384	174.82	49.409
15.37	2.135	17.63	2.706	27.38	6.098	54.20	16.701	178.00	49.968
15.39	2.142	17.73	2.731	27.71	6.230	55.05	17.019	181.25	50.651
15.39	2.154	17.76	2.745	27.74	6.221	55.94	17.339	184.55	51.190
15.42	2.152	17.84	2.766	28.18	6.432	56.81	17.672	187.91	51.730
15.43	2.159	17.96	2.802	28.41	6.499	57.72	18.002	191.34	52.318
15.44	2.158	17.96	2.788	28.49	6.566	58.66	18.334	194.85	53.004
15.46	2.165	18.08	2.822	28.98	6.764	59.62	18.666	198.41	53.440
15.47	2.172	18.16	2.848	29.15	6.826	60.62	18.991	202.04	54.005
15.48	2.171	18.20	2.856	29.31	6.920	61.62	19.334	205.74	54.572
15.51	2.172	18.32	2.892	29.81	7.127	62.63	19.693	209.51	55.023
15.52	2.180	18.38	2.909	29.84	7.128	63.67	20.034	213.34	55.549
15.53	2.181	18.45	2.937	30.17	7.266	64.72	20.384	217.25	55.681
15.56	2.193	18.59	2.977	30.67	7.488	65.81	20.728	221.24	55.881
15.57	2.194	18.62	2.980	30.67	7.472	66.91	21.105	225.25	56.753
15.59	2.198	18.73	3.017	31.12	7.683	68.03	21.483	229.38	57.568
15.61	2.198	18.87	3.055	31.48	7.790	69.17	21.875	233.59	58.014
15.62	2.204	18.87	3.056	31.59	7.871	70.34	22.257	237.87	58.343
15.64	2.202	19.02	3.102	32.06	8.062	71.52	22.624	242.26	58.720
15.67	2.214	19.13	3.131	32.32	8.135	72.74	23.004	246.72	59.220
15.68	2.209	19.18	3.147	32.55	8.262	73.98	23.392	251.25	59.519
15.71	2.226	19.33	3.190	33.04	8.483	75.23	23.796	255.88	59.825
15.73	2.227	19.41	3.217	33.19	8.526	76.52	24.176	260.58	60.354
15.74	2.229	19.50	3.237	33.55	8.704	77.83	24.557	265.38	60.725
15.78	2.244	19.67	3.284	34.07	8.911	79.17	24.970	270.26	60.679
15.79	2.245	19.70	3.301	34.10	8.886	80.53	25.426	275.22	60.544
15.81	2.247	19.85	3.353	34.60	9.117	81.92	25.807	280.27	59.585
15.85	2.256	20.01	3.402	35.04	9.270	83.33	26.217	285.42	59.651
15.86	2.261	20.02	3.407	35.15	9.341	84.77	26.653	290.67	61.740
15.89	2.265	20.21	3.467	35.70	9.575	86.26	27.087	296.03	63.697
15.93	2.271	20.34	3.507	36.01	9.668	87.75	27.572	302.33	64.248
15.93	2.282	20.40	3.530	36.27	9.806	89.27	28.101		
15.97	2.283	20.60	3.593	36.84	10.045	90.82	28.586		
16.01	2.297	20.68	3.616	37.04	10.098	92.41	29.047		
16.02	2.300	20.80	3.660	37.43	10.279	94.02	29.562		

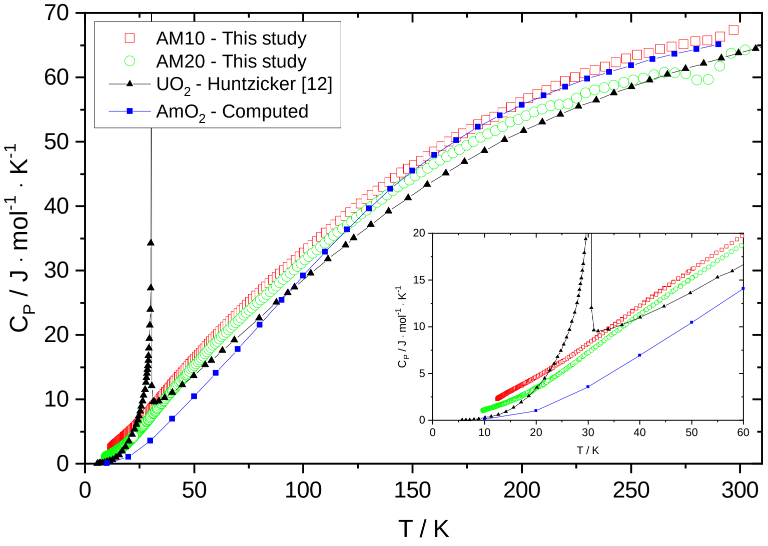

Figure 5.2: Low-temperature heat capacity of the AM10 and AM20 samples, together with the heat capacity data of UO_2 obtained by Huntzicker [17] and the computed curve for AmO_2.

as it is shown in figure 5.4.

In the inset graph of figure 5.2 and figure 5.3 (*a* and *b*) it can be seen that the measured heat capacity of the two intermediate compositions is higher than the heat capacity of the end-members UO_2 and AmO_2, as well as the values obtained from the Neumann-Kopp additivity rule. Because in this temperature region the contribution from the crystal field splitting is practically negligible, the excess heat capacity of the $(U,Am)O_{2-x}$ compositions is most probably due to the changes in the interatomic forces, as result of disorder in the lattice.

Figure 5.5 shows the measured heat capacity of the two intermediate compositions as C_p/T against the squared temperature together with literature data of UO_2 and computed values of AmO_2. It can be seen that an excess heat capacity is present for the AM10 and AM20 compositions, but also that the magnetic transition, observed for UO_2 around 30 K, is not present in our samples despite the high amount of uranium(IV) in the mixture. Moreover, the heat capacity tends not to reach zero at 0 K as it should happen in the case of a perfect crystal, but shows a substantial residual at 0 K. The latter observation is a clear indication for the effect of radiation damage on the crystal lattice due to the alpha decay of americium. The radiation damage, or especially the re-ordering, is a function of the temperature, and especially at these cryogenic temperatures, the kinetics of this process become slow, and thus it is not surprising that we observe this effect in this temperature range. The excess heat capacity observed here is substantially higher than found for $(Th,Pu)O_2$,even considering the presence of Am^{3+} and U^{5+}, and we conclude that the effect of the cationic substitution on the excess vibrational heat capacity is obscured by the effect of radiation-induced disorder.

Based on the experimental results of this temperature interval the heat capacity

Table 5.5: The very low temperature heat capacity values of $U_{0.7995}Am_{0.2005}O_{2-x}$ intermediate composition, from the second run.

T_m / K	$C_P/(J \cdot mol^{-1} \cdot K^{-1})$	T_m / K	$C_P/(J \cdot mol^{-1} \cdot K^{-1})$	T_m / K	$C_P/(J \cdot mol^{-1} \cdot K^{-1})$	T_m / K	$C_P/(J \cdot mol^{-1} \cdot K^{-1})$	T_m / K	$C_P/(J \cdot mol^{-1} \cdot K^{-1})$
9.77	1.044	10.04	1.073	10.67	1.195	12.32	1.483	15.97	2.290
9.78	1.058	10.05	1.096	10.70	1.191	12.40	1.528	15.98	2.224
9.78	1.054	10.05	1.066	10.70	1.200	12.40	1.496	16.14	2.333
9.78	1.044	10.06	1.101	10.73	1.205	12.48	1.539	16.14	2.265
9.79	1.050	10.07	1.068	10.73	1.213	12.48	1.507	16.31	2.373
9.79	1.048	10.08	1.095	10.76	1.217	12.56	1.565	16.32	2.301
9.80	1.055	10.08	1.071	10.77	1.206	12.57	1.521	16.48	2.406
9.81	1.058	10.09	1.096	10.80	1.215	12.65	1.581	16.49	2.340
9.81	1.058	10.09	1.085	10.80	1.223	12.65	1.534	16.66	2.439
9.82	1.057	10.10	1.095	10.83	1.221	12.74	1.593	16.67	2.361
9.83	1.050	10.11	1.081	10.83	1.234	12.74	1.551	16.84	2.476
9.83	1.058	10.12	1.100	10.87	1.248	12.83	1.572	16.85	2.405
9.84	1.064	10.12	1.090	10.87	1.236	12.83	1.610	17.03	2.519
9.85	1.036	10.13	1.095	10.91	1.240	12.92	1.587	17.03	2.436
9.85	1.059	10.13	1.096	10.91	1.237	12.92	1.619	17.22	2.557
9.85	1.027	10.15	1.087	10.95	1.253	13.01	1.611	17.23	2.629
9.85	1.036	10.15	1.106	10.95	1.247	13.01	1.646	17.42	2.602
9.85	1.066	10.16	1.092	10.98	1.254	13.11	1.675	17.43	2.686
9.86	1.038	10.17	1.111	10.99	1.258	13.11	1.624	17.62	2.651
9.86	1.072	10.17	1.088	11.03	1.264	13.21	1.693	17.63	2.730
9.86	1.036	10.19	1.101	11.04	1.253	13.21	1.641	17.82	2.707
9.87	1.046	10.19	1.118	11.05	1.272	13.31	1.706	17.83	2.783
9.87	1.073	10.20	1.109	11.08	1.263	13.32	1.668	18.03	2.757
9.88	1.034	10.20	1.092	11.10	1.274	13.41	1.727	18.04	2.844
9.88	1.075	10.22	1.097	11.13	1.267	13.43	1.685	18.25	2.795
9.88	1.038	10.22	1.118	11.15	1.285	13.53	1.751	18.25	2.888
9.88	1.070	10.24	1.102	11.18	1.270	13.54	1.701	18.47	2.847
9.89	1.051	10.24	1.115	11.19	1.293	13.64	1.765	18.47	2.938
9.89	1.061	10.26	1.110	11.23	1.278	13.64	1.725	18.69	2.889
9.89	1.051	10.26	1.121	11.24	1.297	13.75	1.794	18.69	2.990
9.90	1.038	10.27	1.110	11.27	1.291	13.75	1.738	18.91	2.954
9.90	1.041	10.29	1.129	11.29	1.295	13.86	1.816	18.93	3.045
9.91	1.069	10.29	1.120	11.33	1.286	13.87	1.759	19.13	3.011
9.91	1.045	10.31	1.137	11.34	1.307	13.98	1.839	19.15	3.112
9.91	1.072	10.31	1.121	11.38	1.313	13.98	1.787	19.37	3.274
9.92	1.047	10.33	1.138	11.39	1.313	14.10	1.858	19.38	3.177
9.92	1.068	10.33	1.127	11.44	1.309	14.11	1.807	19.61	3.352
9.93	1.045	10.35	1.141	11.45	1.324	14.22	1.881	19.63	3.258
9.93	1.078	10.35	1.132	11.49	1.322	14.24	1.833	19.86	3.431
9.93	1.056	10.38	1.154	11.50	1.345	14.35	1.915	19.89	3.343
9.94	1.052	10.38	1.133	11.56	1.337	14.37	1.866	20.09	3.403
9.94	1.077	10.40	1.145	11.57	1.352	14.48	1.954	20.11	3.512
9.95	1.054	10.40	1.149	11.69	1.353	14.50	1.896	20.28	3.458
9.95	1.079	10.42	1.142	11.70	1.369	14.62	1.978	20.37	3.576
9.95	1.062	10.43	1.149	11.76	1.368	14.63	1.922	20.63	3.635
9.96	1.048	10.45	1.148	11.76	1.392	14.76	2.007	20.67	3.548
9.96	1.079	10.45	1.159	11.82	1.378	14.76	1.959	20.88	3.618
9.97	1.058	10.47	1.155	11.82	1.406	14.90	2.053	20.90	3.716
9.97	1.084	10.48	1.175	11.88	1.390	14.90	1.993	21.11	3.682
9.98	1.057	10.49	1.158	11.89	1.419	15.04	2.084	21.13	3.803
9.98	1.088	10.51	1.173	11.95	1.406	15.05	2.021	21.40	3.867
9.99	1.062	10.52	1.163	11.96	1.432	15.18	2.117	21.46	3.789
9.99	1.063	10.54	1.172	12.02	1.421	15.19	2.056	21.52	3.827
10.00	1.083	10.55	1.172	12.02	1.450	15.33	2.148	21.73	3.986
10.00	1.061	10.57	1.179	12.09	1.433	15.34	2.096	21.88	4.070
10.01	1.081	10.58	1.175	12.09	1.470	15.48	2.187	21.98	4.097
10.01	1.064	10.60	1.186	12.17	1.482	15.50	2.123	22.06	4.027
10.02	1.089	10.60	1.182	12.17	1.449	15.64	2.217	22.33	4.225
10.02	1.063	10.63	1.196	12.24	1.469	15.66	2.164		
10.03	1.086	10.63	1.193	12.24	1.502	15.80	2.260		
10.03	1.072	10.66	1.201	12.32	1.511	15.82	2.197		

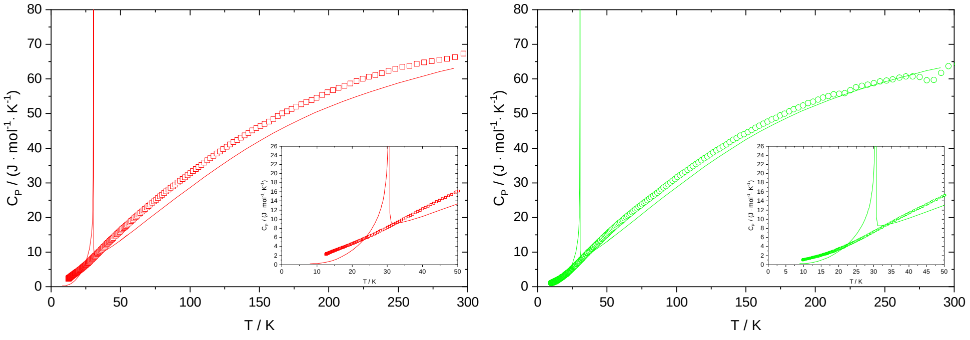

(a) **(b)**

Figure 5.3: The low-temperature heat capacity of the AM10 (□) and AM20 (○) samples studied in this work. The solid lines – and – are the computed Neumann-Kopp heat capacities.

functions were obtained by fitting the heat capacity values with the following polynomial function:

$$C_{p,m}/(J \cdot K^{-1} \cdot mol^{-1}) = A + B \cdot (T/K) + C \cdot (T/K)^2 + D \cdot (T/K)^{-1} \quad (5.2)$$

where A, B, C and D are the equation coefficients which are listed in table 5.6.

Table 5.6: Constants for the polynomial fit equations of the low-temperature heat capacity according to $C_P/(J \cdot mol^{-1} \cdot K^{-1}) = A + B \cdot (T/K) + C \cdot (T/K)^2 + D \cdot (T/K)^{-1}$ and the corresponding values for $C_P(298.15K)$ obtained in this study.

	9.7 < (T/K) < 300				(T/K)= 298.15
Sample	A	B	C ·10^{-4}	D	$C_P(J \cdot mol^{-1} \cdot K^{-1})$
AM10	-5.31776	0.44735	-6.96334	26.53244	66.3
AM20	-6.90775	0.45561	-7.61659	34.62830	61.3

The excess heat capacity in this temperature region, obtained from comparing the measured results with the Neumann-Kopp's additivity rule, is shown in 5.6. In the lowest temperature range close to zero, the magnitude of the excess heat capacity is even more evident when plotting the relative excess heat capacity, as shown in figure 5.7.

5.3.2. The high-temperature range (50<(T/K)<300)

It is clear that for this temperature range the heat capacity of the mixed oxides is consistently above that of the end members, and an important deviation from ideality is present for both compositions, though surprisingly more prominent for the AM10 sample. The excess heat capacity increases continuously with increase of temperature up to a maximum value followed by a slight decrease, in the higher temperature region, for the AM10 sample and a more prominent decrease for AM20 sample. The calculated Schottky contribution from the crystal field splitting of the Am^{4+} ($5f^5$) ion with a 6H5/2

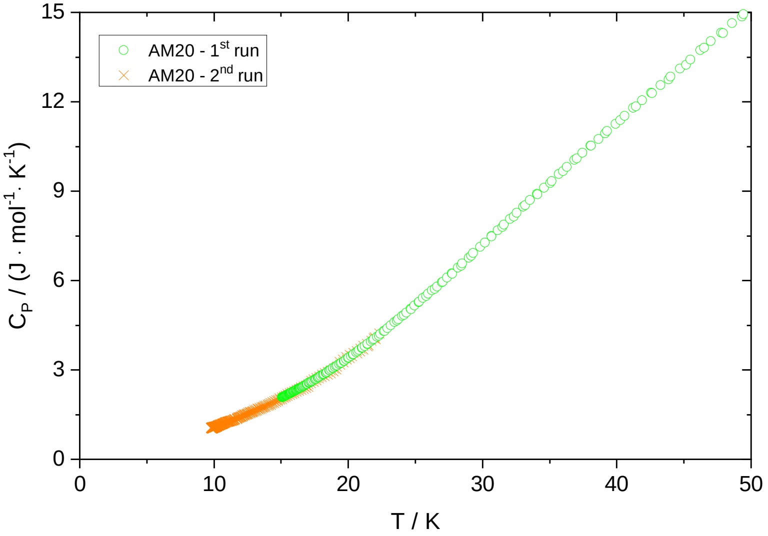

Figure 5.4: Comparison of the measured heat capacity results from the two runs of the AM20 composition.

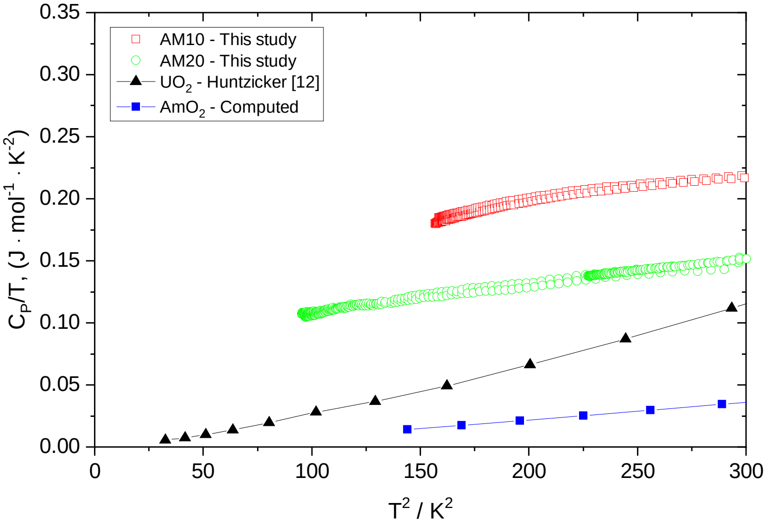

Figure 5.5: Heat capacity over temperature versus squared temperature of the measured samples in comparison with the UO_2 and AmO_2 end-members .

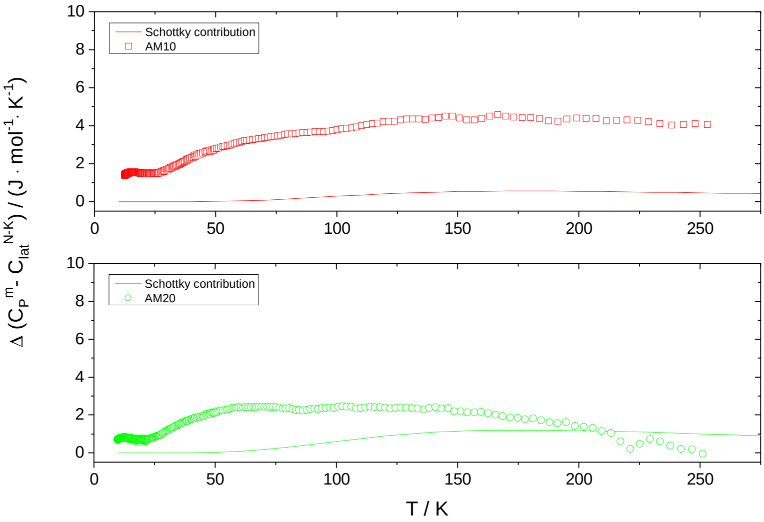

Figure 5.6: Excess heat capacity evolution with temperature; symbols represent the values calculated from the present experimental results and the end-members; solid lines represent the electronic contribution calculated from the crystal field splitting, scaled to the Am concentration.

ground state [15] is small in this temperature range, as shown in figure 5.6. For the case of the presence of Am^{3+} and U^{5+}, the calculation of the Schottky contribution is not so straightforward. Am^{3+} ($5f^6$) has a non degenerate 7F0 ground state, and thus does not yield an excess heat capacity. U^{5+} ($5f^1$) has a 2F5/2 ground state, but the energy between the split doublet and quartet a fluorite cubic environment is poorly known. But it is unlikely that the excess is much larger than for Am^{4+}, since the energy difference is only 328 cm^{-1} for a similar doublet-quartet splitting in that case.

Due to the Stycast encapsulation, the heat capacity values above 250 K show some irregularities, particularly for the AM20 sample, as the result of the reduced resolution resulting from the larger contribution of the Stycast to the total heat capacity, and for this reason the results above this temperature were eliminated from the current analysis. However, when extrapolated to 298.15 K, based on a simultaneous linear regression, the heat capacity values are comparable with the heat capacity values previously obtained in one of our studies [1, 18]. Figure 5.8 shows that the results obtained in this work for $(U_{1-y},Am_y)O_{2-x}$ solid solution with y= 0.0811 and 0.2005 agree very well with the high-temperature data derived from drop calorimetric measurements for the same compositions.

The heat capacity functions which describe the two intermediate compositions, in this temperature range, were obtained by fitting the experimental values with equation 5.2 and the variables are given in table 5.6. Taking into account all high-temperature enthalpy data previously measured [1] and the low-temperature heat capacities measured in this study, the C_p at T= 298.15 K was obtained (table 5.6) for the two intermediate compositions.

As concluded in our previous study, based on low- and high-temperature heat

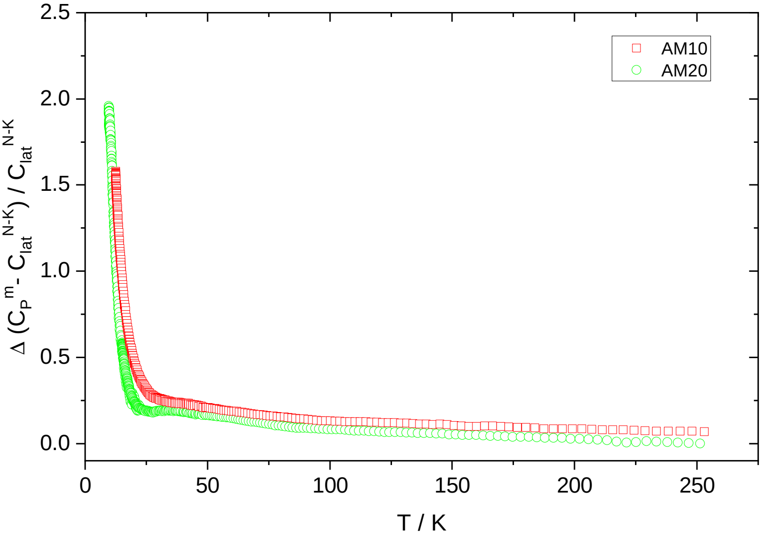

Figure 5.7: The relative excess heat capacity as a function of temperature.

capacity functions, no excess heat capacity is revealed for the high temperature region.

5.4. Discussion and Conclusions

The low-temperature heat capacities of the $(U_{1-y},Am_y)O_{2-x}$ solid solution with y= 0.0811 and 0.2005 have been measured from a minimum of 12.52 and 9.77 K, respectively up to about 300 K and the results have shown that a substantial excess heat capacity is observed in the temperature region below about 30 K, which becomes very pronounced near absolute zero temperature. When we compare these findings to the results of a similar study of the $(Th,Pu)O_2$ solid solution [2], we observe that:

- The relative excess heat capacity is larger in the $(U_{1-y},Am_y)O_{2-x}$ solid solution, reaching values of $\Delta(C_p^m - C_{lat})/C_{lat}$ up to 2, compared to 0.5 for $(Th,Pu)O_2$, whereas the size difference (Am^{3+}/U^{5+} versus U^{4+} and Pu^{4+} versus Th^{4+}) is similar for both cases.

- The residual heat capacity values at 0 K of $(U_{1-y},Am_y)O_{2-x}$ are about 0.10-0.15 mJ K^{-2} mol^{-1}, whereas they are 0 in the case of $(Th,Pu)O_2$.

This indicates that the lattice strain due to cationic substitution on the sublattice alone cannot explain the current results, and that self-radiation effects creating point defects on the anionic lattice must play a role. This is substantiated by the comparison to the heat capacity results of PuO_2, for which the measurements of dioxide of the ^{239}Pu isotope, performed by adiabatic calorimetry, give a substantial residual heat capacity at zero temperature (about 60 mJ K^{-2} mol^{-1}, see figure 2 in [2]), whereas this is absent for

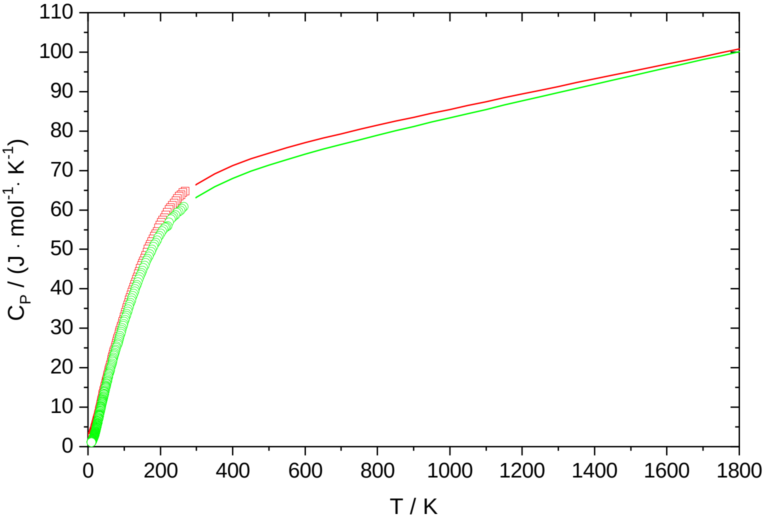

Figure 5.8: Heat capacity of AM10 and AM20 obtained in this study as a function of temperature. Low-temperature data obtained by PPMS and high-temperature data obtained by using the low-temperature heat capacity and the high-temperature enthalpy increment measurements from [1].

the dioxide of the much longer lived ^{242}Pu isotope. On the other hand, using relaxation calorimetry of $^{239}PuO_2$, this effect was not observed [2], which can be attributed to different experimental approaches between adiabatic and relation calorimetry. However, ^{241}Am ($t_{1/2}$ = 432.6 years) decays much faster than ^{239}Pu ($t_{1/2}$ = 24110 years), and time, of course, plays an important role in this.

Self-irradiation effects in actinide dioxides are well studied, and the creation of anionic defects results in an expansion of the lattice, generally described by the equation $\Delta a/a_0 = A(1-e^{-B\lambda t})$, where a is the lattice parameter, a_0 the lattice parameter a time $t = 0$, λ is the decay constant of the actinide isotope, and A and B are constants, A representing the maximum expansion and B the kinetics of creating and recombination of defects. Horlait et al. [7] studied the self-irradiation effects in $(U_{1-y},Am_y)O_{2-x}$ and found a saturation at about $\Delta a/a_0 = 0.27$ or 0.8 vol%. As can be deduced from the equation, the kinetics of the process is fast in the initial time period after $t = 0$, but this period was, however, obscured by slight reoxidation in the work of Horlait. But from the studies of $^{241}AmO_2$ [20] it is clear that the defect accumulation is already substantial after a few days of storage at room temperature. In our case the samples were annealed, but a few days were needed before the actual measurement was started. Moreover, during the measurement the temperature was lowered down to about 10 K in about 40-60 hours. Of course the kinetics of recombination are affected by temperature, resulting in a higher self-radiation damage at the low temperature reached during the measurement. We thus conclude that self-irradiation effect dominates the excess heat capacity at very low temperatures in the current measurement. The differences in the residual heat capacity values at 0 K for the two samples, the magnitude of which not corresponding to the Am content, may be due to the differences in dose accumulated in the time elapsed during the preparation of the measurements.

The antiferromagnetic transition at 30.8 K specific to UO_2 [17] is not present in both measured samples in spite of the relatively low americium concentrations, although the Am^{3+}-U^{5+} charge compensation implies a two times larger ionic substitution. This observation is in line with the results of Klemme *et al.* for the magnetic transition in the $MgAl_2O_4$-$MgCr_2O_4$ solid solution [21], for which the lambda peak was absent at 20 mol% $MgAl_2O_4$ and replaced by a broad Schottky-type anomaly. We can assume a similar effect in the $(U,Am)O_2$ solid solution, and indeed the excess heat capacity above about 30 K is substantial. However, it is likely that this effect is not only due to the Schottky contribution, but includes contributions from radiation-induced disorder and lattice strain effects.

Finally, we conclude from the present results that it is probably impossible to measure heat capacity of AmO_2 reliably, as the current methods are not fast enough to maintain perfectly annealed samples containing significant quantities of the short-lived ^{241}Am.

References

[1] O.S. Vălu, D. Staicu, O. Beneš, R.J.M. Konings, P. Lajarge, J. Alloy Compd. 614 (2014) 144-150.

[2] O.S. Vălu, O. Beneš, R.J.M. Konings, J.-C. Griveau, E. Colineau, J. Phys. Chem. Solids, 86 (2015) 194-206.

[3] F. Lebreton, D. Horlait, R. Caraballo, P. M. Martin, A. C. Scheinost, A. Rossberg, C. Jégou, T. Delahaye, Inorg. Chem. 54 (2015) 9749-9760.

[4] C. Hurtgen, J. Fuger, Inorg. Nucl. Chem. Letters 13 (1977) 179-188.

[5] D. Prieur, A. Jankowiak, D. Roudil, S. Dubois, C. Leorier, N. Herlet, P. Dehaudt, J.-P. Laval, P. Blanchart, J. Nucl. Mater. 411 (2011) 15-19.

[6] D. Prieur, P.M. Martin, F. Lebreton, T. Delahaye, A. Jankowiak, J.-P. Laval, A.C. Scheinost, P. Dehaudt, P. Blanchart, J. Solid State Chem. 194 (2012) 206-211.

[7] D. Horlait, F. Lebreton, P. Roussel, T. Delahaye, Inorg. Chem. 52 (2013) 14196-14204.

[8] A. Fernandez, D. Haas, R.J.M. Konings, J. Somers, J. Am. Ceram. Soc. 83 (2002) 694-696.

[9] J. Somers, A. Fernandez, J. Am. Ceram. Soc. 88 (2005) 827-832.

[10] M. Vespa, M. Rini, J. Spino, T. Vitova, J. Somers, J. Nucl. Mater. 421 (2012) 80-88.

[11] S. Abousahl, P. Van Belle, H. Ottmar, Nucl. Instrum. Methods Phys. Res., Sect. A: Spectrom. Detect. Assoc. Equip. 543 (2005) 608-618.

[12] P. Javorský, F. Wastin, E. Colineau, J. Rebizant, P. Boulet, G. Stewart, J. Nucl. Mater. 344 (2005) 50-55.

[13] F. Grønvold, J. Inorg. Nucl. Chem. 1 (1955) 357.

[14] K. Mendelssohn, E. King, J. Lee, M. Rand, C. Griffin, R. Street, in: A.E. Kay, M.B. Waldron (Eds.), Plutonium (1965) 189-204.

[15] R. J. M. Konings, J. Chem. Thermodyn. 36 (2004) 121-126.

[16] H. Kopp, Phil. Trans. R. Soc. Lond. 155 (1865) 71-202.

[17] J. J. Huntzicker, E. F. Westrum, J. Chem. Thermodyn. 3 (1971) 61-76.

[18] E. Epifano, O. Beneš, O.S. Vălu, J. Zappey, F. Lebreton, P. M. Martin, C. Guéneau, R.J.M. Konings. J. Nucl. Mater. 494 (2017) 95.

[19] D. Prieur, A. Jankowiak, C. Leorier, N. Herlet, L. Donnet, P. Dehaudt, C. Maillard, J.-P. Laval, P. Blanchart, Powder Technology 208 (2011) 553-557.

[20] C. Hurtgen, J. Fuger, Inorg. Nucl. Chem. Lett. 13 (2015) 179-188.

[21] S. Klemme, M. Ahrens, Phys. Chem. Minerals 34 (2007) 59–72.

6

The low-temperature heat capacity of the (Th,Pu)O_2 solid solution

The low-temperature heat capacity of the $(Th_{1-y},Pu_y)O_2$ solid solution with y = 0.03, 0.08, 0.30, 0.54 and 0.85 was determined from 4 K up to about 300 K with a PPMS instrument using the hybrid adiabatic relaxation method. In addition, the heat capacity of $^{239}PuO_2$ end member was also measured and compared with available literature data for $^{242}PuO_2$, observing an indistinguishable match. The obtained heat capacity values of the intermediate compositions are greater than the data obtained from Neumann-Kopp's molar additivity rule based on the ThO_2 and PuO_2 end-members, and a substantial excess capacity is observed for all intermediate compositions, particularly at the lowest temperatures.

This chapter is reprinted with kind permission of Elsevier: *The low-temperature heat capacity of the (Th,Pu)O_2 solid solution. O.S. Vălu, O. Beneš, R.J.M. Konings, J.-C. Griveau, E. Colineau. Journal of Physics and Chemistry of Solids 86 (2015) 194-206.*

6.1. Introduction

In the context of evaluating the prospects of thorium-based fuel for Generation IV nuclear reactors [1], a substantial effort is made in studying the thermal properties of its mixed oxides with the actinide elements uranium and plutonium. Numerous investigations were performed in a wide temperature range to understand the behaviour of this potential nuclear fuel from thermodynamic point of view [2–9].

Heat capacity is one of the key thermodynamic properties as it describes the relation between the heat change and temperature of a material. It also reveals essential information about phase transitions, lattice vibrations, energy excitations and defect structures of a material. It is clear that for any material the heat capacity tends to decrease strongly with decreasing temperature, finally reaching zero at the absolute zero temperature in case of a perfect crystal. When a mixed oxide solid solution is considered, the heat capacity is strongly related to the end-members. However, the substitution of isovalent ions with different size on the cation sublatice is changing the interatomic distances of the first nearest neighbor atoms by compression or expansion of the bonds. Also contributions to the heat capacity that are of electronic origin such as Schottky anomalies, may be affected by the dilution. Therefore the behaviour of solid-solution materials may deviate from the trend suggested by the end members and may show substantial excess contributions.

In one of our previous studies [10] the heat capacity of thorium-plutonium mixed oxides was investigated in the high-temperature range (476-1790 K). In the present work we have extended our investigations of this system to the low-temperature regime. We have measured the heat capacity of (Th,Pu)O_2 solid solutions with 3, 8, 30, 54 and 85 wt.% PuO_2 in the temperature range from a minimum of 3.6 K to about 300 K. This minimum temperature was higher than normally achievable one by the equipment used, due to effects of self-heating resulting from the ^{239}Pu isotope used in our work. Since the literature data for PuO_2 refer to a material containing the ^{242}Pu isotope [11], in which the self-heating is about 15 times lower, we also investigated the $^{239}PuO_2$ end-member in the temperature range of 5.9 K up to about 300 K. The complete data set allows a detailed analysis of the variation of the heat capacity for these solid solutions as a function of the composition.

6.2. Experimental

6.2.1. Sample preparation

The heat capacity measurements performed in this study were done on samples with different PuO_2 concentrations which were produced by the sol-gel technique. For this process the thorium nitrate and plutonium dioxide were used as starting materials. The preparation and characterization of the $(Th_{1-y},Pu_y)O_2$ solid solutions with y = 0.03, 0.08, 0.30, 0.54 and 0.85 is described in detail in our previous work [10] but also by Cozzo *et al.* [9]. The pure PuO_2 sample was a fragment of a pellet made from stock material [9, 10]. In order to avoid build up of radiation damage, our samples were annealed before the measurement. The isotopic composition of the plutonium used was 91.5 % ^{239}Pu, 8.302 % ^{240}Pu, and 0.685 % ^{241}Am as decay product of ^{241}Pu.

6.2.2. The PPMS technique

The low temperature heat capacity measurements were performed using a PPMS-9 instrument (Physical Property Measurement System, Quantum Design) in the temperature range from 7.3 - 291.9 K, 3.6 - 272.2 K, 6.5 - 291.9 K, 7.3 - 297.4 K and 8.1 - 296.6 K for the solid solutions with 3, 8, 30, 54 and 85 wt.% PuO_2, respectively and from 5.9 K to 270.5 K for PuO_2. The instrument installed in our laboratories can determine the specific heat of samples with a relatively small mass (few mg) by a hybrid adiabatic relaxation method. The description of the technique and details of our apparatus and the method of handling radioactive actinide samples can be found in the work of Javorský *et al.* [13]. The measurements of $Th_{0.97}Pu_{0.03}O_2$, $Th_{0.92}Pu_{0.08}O_2$, $Th_{0.70}Pu_{0.30}O_2$, $Th_{0.46}Pu_{0.54}O_2$, $Th_{0.15}Pu_{0.85}O_2$ and PuO_2 were made on small pieces of discs which were wrapped in an appropriate amount of Stycast (2850 FT) low-temperature conductive epoxy. Self-heating correction was taken into consideration and the heat capacity of the corresponding Stycast was measured separately and subtracted, resulting in an uncertainty of the measurements of 3-5 percent, depending on the mass of sample.

Table 6.1: (Th,Pu)O_2 compositions, weights and temperature intervals.

Composition	Temperature [K]	Mass [mg]
$Th_{0.97}Pu_{0.03}O_2$	7.34 - 21.99	27.4
	21.99 - 291.94	27.4
$Th_{0.92}Pu_{0.08}O_2$	3.58 - 22.15	16.8
	22.15 - 272.27	25.7
$Th_{0.70}Pu_{0.30}O_2$	6.55 - 22.22	20.3
	22.22 - 291.91	20.3
$Th_{0.46}Pu_{0.54}O_2$	7.25 - 21.96	10.1
	21.96 - 297.39	21.4
$Th_{0.15}Pu_{0.85}O_2$	8.05 - 22.07	7.4
	21.99 - 296.61	27.4
PuO_2	5.81 - 30.28	5.6
	30.44 - 270.49	16.6

For the current study, measurements of the heat capacity were performed in two temperature ranges in order to reach the lowest temperature possible. For each composition, two samples were selected with different masses. For the very low temperature region a smaller sample, when available, was used in order to obtain the lowest value on the temperature scale in view of the self heating effect of ^{239}Pu. From about 22 K up to 300 K the quantity of used material was almost doubled. In table 6.1 the masses of the samples used for this study are listed together with the temperature range that was covered for each composition.

6.3. Results and Discussion

6.3.1. PuO_2

The results for the heat capacity of $^{239}PuO_2$ end-member are shown in figure 6.1-(a) and are listed in table 6.4. Our results agree very well with the available literature data for $^{242}PuO_2$ by Flotow *et al.* [11] obtained by traditional adiabatic calorimetry on a sample of 22.5 grams. These authors also measured the heat capacity of a $^{244}PuO_2$ sample (3.64 grams) between 4 and 25 K, obtaining very similar results and confirming the absence of anomalies. The radioactivity of ^{239}Pu and also the minor isotope ^{240}Pu that is present in our sample is much higher than that of ^{242}Pu and as a result the self-heating of the sample and rapid build up of radiation-induced defects may affect the measurement. The adiabatic calorimetric measurements on $^{239}PuO_2$ by Sandenaw [12] have clearly demonstrated that this could lead to anomalous and irreproducible results. A comparison of the heat capacity obtained in this study with the above mentioned literature data is shown in figure 6.2 as C_p/T against the squared temperature.

In our measurements the self-heating effect was limited by using very small amounts of samples (5.6 and 16.6 mg), and applying appropriate corrections based on the decay heat. The influence of radiation-induced defects were limited by annealing the sample just before the measurement at T = 1273 K in air for 10 hours. Moreover, in the PPMS equipment the heat capacity of the sample was measured when cooling down from room temperature, starting with a pristine sample, gradually building up radiation defects that more easily survive with decreasing temperature. This is different from adiabatic calorimetry for which the sample is first brought to the lowest cryogenic temperature, where radiation defects immediately build up with a high survival rate, and the complete measurement is performed on more damaged sample.

The experimental heat capacity values in the very low temperature region (<12 K) have been fitted using the following equation:

$$\frac{C_P}{N_A \cdot k_B} = \frac{12 \cdot \pi^4}{5} \cdot \left(\frac{T}{\theta_D}\right)^3 \tag{6.1}$$

Here, T is the temperature, N_A is the Avogadro's number, k_B is Boltzmann's constant and θ_D is the Debye temperature. This equation implies a linear relation between C_p/T and T^2, and as shown in figure 6.2 this is indeed observed for our results for PuO_2. Moreover, C_P/T nicely extrapolates to zero at T = 0 K. Our data are slightly higher than the results of Flotow *et al.* for $^{242}PuO_2$ and $^{244}PuO_2$, well within the uncertainties of the measurements. The results of Sandenaw for $^{239}PuO_2$ are much higher and suggest a non-zero entropy at T = 0 K, probably resulting from radiation-induced disorder. From our data we obtain $\theta_D = 234.3$ K for PuO_2. By extrapolation of the linear relation to 0 K, we obtain for the entropy at 12 K, S° = 0.087 J·K^{-1}·mol^{-1}, whereas Flotow *et al.* [11] obtained S° = 0.051 J·K^{-1}·mol^{-1} at the same temperature.

The absolute entropy at 298.15 K derived from our low-temperature heat capacity data is S°(298.15) = 65.79 J·K^{-1}·mol^{-1}.

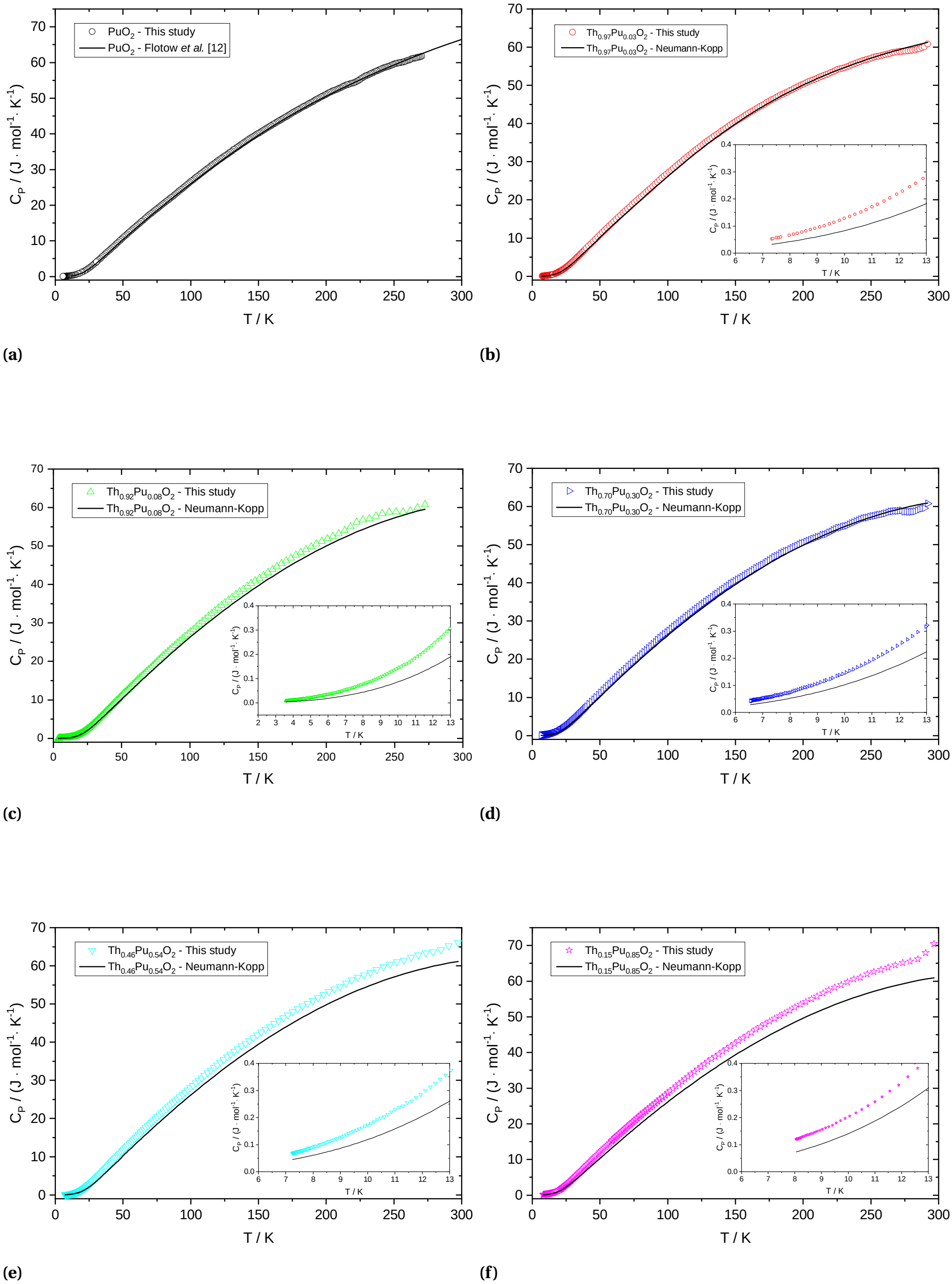

(a) (b) (c) (d) (e) (f)

Figure 6.1: Low-temperature heat capacity of the intermediate compositions (b)-(f). The inset graphs show the very low temperature region, where the Neuman-Kopp data were computed using equation 6.1. (a) shows the comparison of the measured PuO$_2$ heat capacity with literature data published by Flotow *et al.* [11] on ^{242}PuO$_2$ sample.

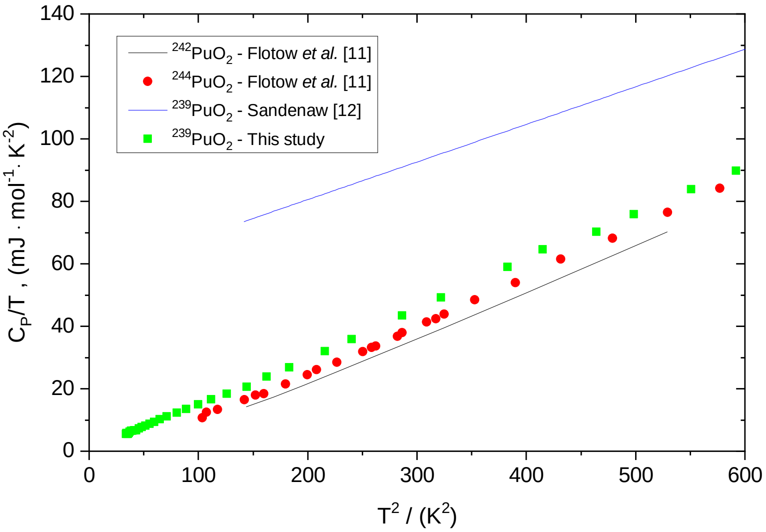

Figure 6.2: Heat capacity over temperature versus squared temperature of the measured $^{239}PuO_2$, together with the literature data of Flotow *et al.* [11] and Sandenaw [12].

6.3.2. The $(Th_{1-y},Pu_y)O_2$ solid solutions

The results for the low-temperature heat capacity of $(Th_{1-y},Pu_y)O_2$ solid solutions for y = 0.03, 0.08, 0.30, 0.54 and 0.85 are shown in figure 6.1 and listed in tables 6.5-6.9. The plots in figure 6.1 show that the heat capacity curves of the samples increase smoothly with increasing temperature and that no phase transitions or other thermal anomalies are present for the measured temperature range.

In this paper the low temperature heat capacity is described as the sum of the lattice and excess components as shown in equation 6.2:

$$C_P = C_{lat} + C_{exs} \tag{6.2}$$

In the actinide oxides, the lattice heat capacity is attributed principally to the lattice vibrations, while the excess heat capacity is mainly due to the contribution of the $5f$ electron excitation caused by the crystal field splitting [14–16], resulting in a Schottky-type anomaly. In the solid solutions, however, the excess heat capacity contains an additional contribution due to the interaction of substitutional atoms on the crystal lattice.

$$C_P = C_{lat} + C_{Sch} + C_{mix} \tag{6.3}$$

In our work the lattice heat capacity is computed from the composition weighted average of the end-members (Neumann-Kopp). The PuO_2 lattice heat capacity was obtained after subtracting C_{Sch} calculated from the crystal field energy levels (0, 992, 1776, 2153 cm^{-1}) for the $^5I_4$ ground state of the $5f^4$ configuration [14]. For ThO_2, which has a $5f^0$

configuration, no electronic contribution needs to be considered. The phonon contribution can be described by the harmonic crystal approximation and additional correction for internal anharmonicity of vibrational modes [17].

For computing the Neumann-Kopp data, the results of ThO_2 previously measured with the same equipment as used in this work [18] and PuO_2 measured in this study were used, respectively. Due to lack of experimental results below 7 K for the considered end-members, we had to extrapolate the heat capacity of ThO_2 and PuO_2 down to 0 K. The Debye model was used to describe this low-temperature region (0-12 K) and the heat capacity function of each individual oxide was obtained.

The low temperature range (0 < (T/K) < 25)

In this temperature range the Schottky contribution from the crystal field splitting of PuO_2 is practically negligible, so any excess heat capacity of the $(Th,Pu)O_2$ compositions is related to cation substitution and disorder on the crystal lattice affecting the phonon frequencies of the solid solution compared to the end members. The substitution of isovalent ions with different size on the cation sublatice, Pu^{4+} (100 pm) and Th^{4+} (108 pm) is changing the interatomic distances of the first nearest neighbor atoms by compression or expansion of the bonds. Small changes in the interatomic distances can lead to significant changes in the interatomic forces [19, 20], particularly at low temperature where the bonds become stiffer, and thus to changes in the phonon density of states [17]. Generally this results in a positive excess heat capacity, as observed in this work.

The inset graphs of figure 6.1 clearly show a positive difference between the measured and calculated lattice heat capacity values, indicating a substantial excess contribution in this temperature interval.

Figure 6.3 shows the measured heat capacity of the intermediate compositions as C_p/T against the squared temperature together with the data of the end-members, the heat capacity of PuO_2 measured in this study and the heat capacity of ThO_2 measured with the same instrument [18]. The experimental heat capacity values in the very low temperature region (< 12 K) have been fitted using equation 6.1 to yield the Debye temperature θ_D, which is characteristic for the phonon dispersion in a solid. Its variation in the $(Th,Pu)O_2$ system is represented in figure 6.4-(a) as $\Delta\theta_D$, showing that the Debye temperatures of the solid solution are systematically lower than the end members, which is thus a clear indication for the substantial impurity-phonon scattering occuring in this system at low temperature.

Table 6.2: The corresponding values for θ_D, $\Delta\theta_D$, $S^0(12K)$ and $\Delta S^0(12K)$ obtained in this study.

Composition	θ_D (K)	$\Delta\theta_D$ (K)	$S^0(12K)$ $(J \cdot mol^{-1} \cdot K^{-1})$	$\Delta S^0(12K)$ $(J \cdot mol^{-1} \cdot K^{-1})$
ThO_2	288.7	0	0.047	0
$Th_{0.97}Pu_{0.03}O_2$	247.5	-39.6	0.074	0.026
$Th_{0.92}Pu_{0.08}O_2$	237.6	-46.7	0.084	0.034
$Th_{0.70}Pu_{0.30}O_2$	236.9	-35.5	0.084	0.025
$Th_{0.46}Pu_{0.54}O_2$	223.5	-35.8	0.100	0.031
$Th_{0.15}Pu_{0.85}O_2$	219.1	-23.4	0.110	0.029
PuO_2	234.3	0	0.087	0

This is also evident from the entropy calculated at 12 K for each individual composition, based on the low-temperature data obtained in this study using the same approach as for the PuO$_2$. Its variation, shown in figure 6.4-(b), reveals a similar deviation from the linear interpolation of the end-members, with composition. The θ_D, $\Delta\theta_D$, $S^0(12K)$ and $\Delta S^0(12K)$ values are given in table 6.2.

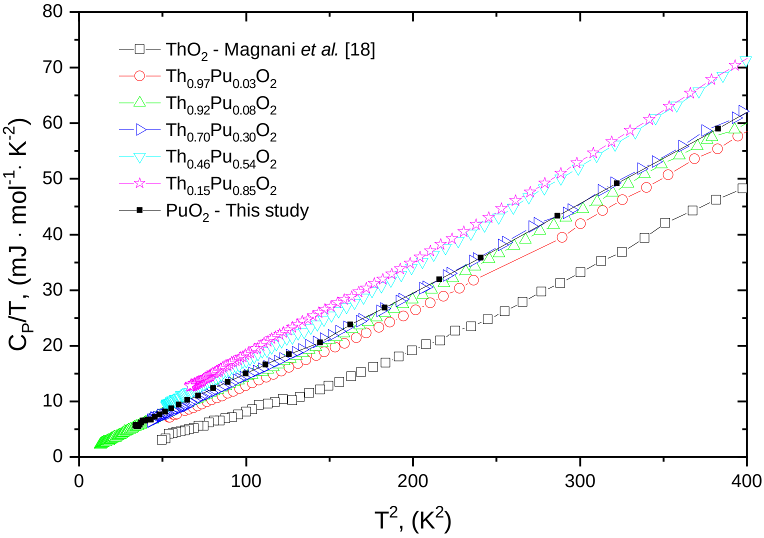

Figure 6.3: Low-temperature heat capacity over temperature versus squared temperature of the measured intermediate compositions, together with the values of the end-members, PuO$_2$ measured in this study and ThO$_2$ from Magnani *et al.* [18].

The intermediate temperature range (25 < (T/K) < 250)

In this temperature range the excess contribution (Schottky) from breaking of the degeneracy of the $^4I_5$ electronic ground state of the Pu^{4+} ion also needs to be considered in the analysis of the heat capacity. It should be realised that towards the end of this temperature range the excess heat capacity represents a small difference between two large numbers, and is thus subjected to increasing uncertainties. Moreover, the samples had to be encapsulated in a significant quantity of Stycast, for contamination reasons [13], and as a result a non-negligible contribution to the measured total signal was due to the encapsulation.

The comparison to the lattice heat capacity (i.e. without considering the Schottky anomaly in PuO$_2$) obtained from the Neumann-Kopp's molar additivity rule is shown in figure 6.1 and the calculated excess heat is shown in figure 6.5 as $\Delta(C_P{}^m - C_{lat}{}^{N-K})$. It can be seen that an excess contribution is present for all compositions, and it becomes more obvious with increasing PuO$_2$ concentration. For the two samples with the highest concentration, Th$_{0.46}$Pu$_{0.54}$O$_2$ and Th$_{0.15}$Pu$_{0.85}$O$_2$, we observe a clear rise in the excess heat capacity above 100 K, at which the effect of the Schottky contribution is expected.

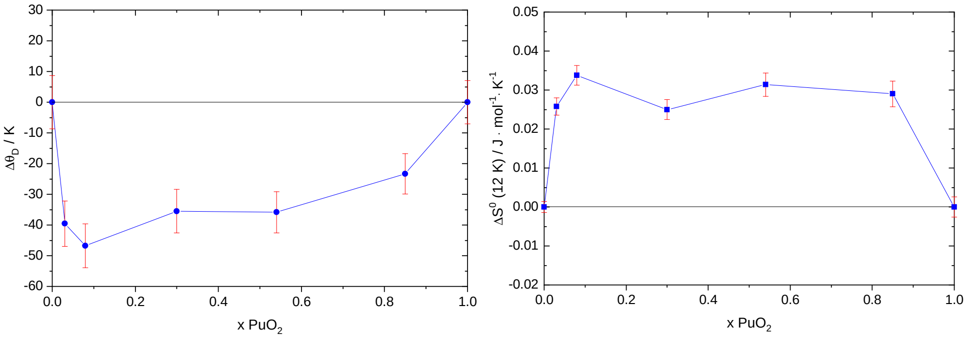

(a) **(b)**

Figure 6.4: (a) Evolution of the Debye temperature (θ_D) with PuO_2 content of the (Th, Pu)O_2 system, represented as deviation from ideality $\Delta\theta_D$. (b) Evolution of the entropy at 12 K with PuO_2 content of the (Th, Pu)O_2 system, represented as deviation from ideality $\Delta S^0(12K)$.

For the $Th_{0.70}Pu_{0.30}O_2$, $Th_{0.92}Pu_{0.08}O_2$ and $Th_{0.97}Pu_{0.03}O_2$ compositions, the excess heat capacity is constant above about 100 K, considering the accuracy in that temperature range.

It is also clear from figure 6.5 that the cation substitution and disorder on the crystal lattice are still prominent in this temperature range. From the results we thus conclude that the increase of the excess heat capacity up to 150 K is mainly due to the effect of cation substitution on the phonon modes and above this temperature the excess arising from the Schottky contribution of the 5f electrons of Pu^{4+} (crystal field splitting) is evident in the samples with high Pu concentration.

Using the low-temperature heat capacity results of the intermediate compositions the relative excess heat capacity has been obtained and is shown in figure 6.6. It indicates that the excess heat capacity can account for more than 50 % of the total at very low temperatures and decreases to about 5 % at 250 K.

Table 6.3: Constants for the polynomial fit equations of the low temperature heat capacity according to $C_P/(J \cdot mol^{-1} \cdot K^{-1}) = A + B \cdot (T/K) + C \cdot (T/K)^2 + D \cdot (T/K)^{-1}$

Solid solution	$C_P(298.15K)$	A	B	C $\cdot 10^{-4}$	D
$Th_{0.97}Pu_{0.03}O_2$	60.72	-11.14913	0.44351	-6.88722	70.4244
$Th_{0.92}Pu_{0.08}O_2$	62.36	-10.58597	0.44119	-6.49330	59.5451
$Th_{0.70}Pu_{0.30}O_2$	62.09	-9.88905	0.43234	-6.58941	48.14442
$Th_{0.46}Pu_{0.54}O_2$	65.42	-9.21239	0.43232	-6.13153	37.40719
$Th_{0.15}Pu_{0.85}O_2$	67.37	-8.2539	0.42443	-5.72083	20.91311

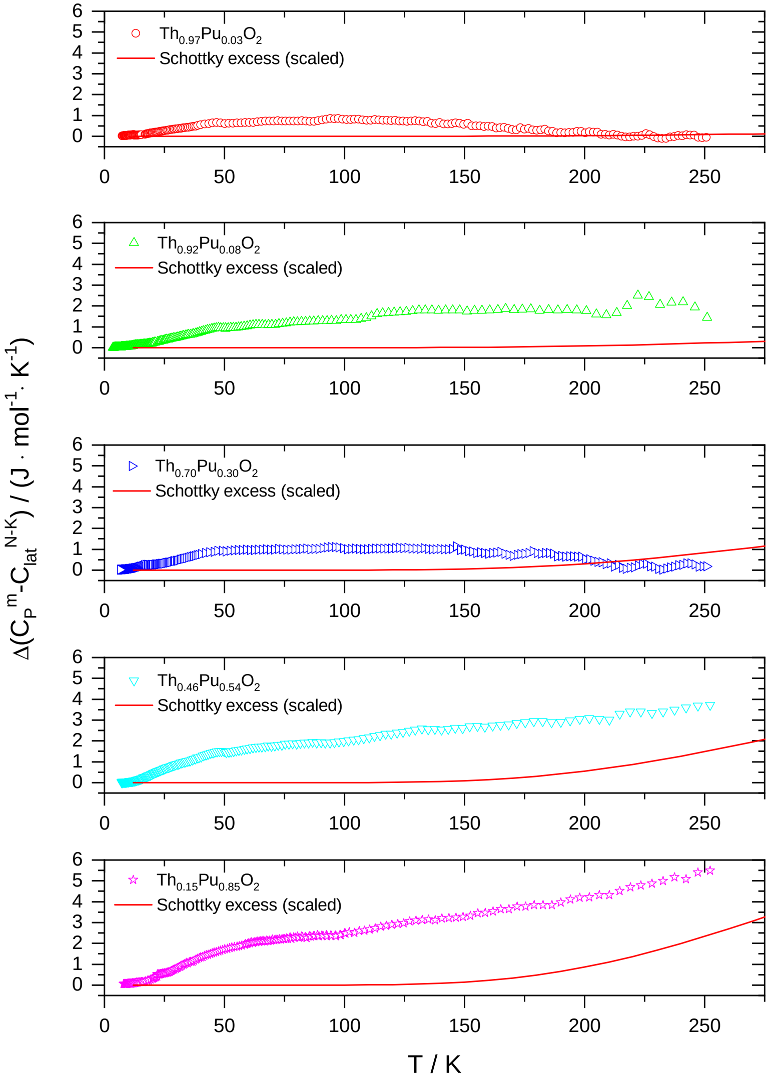

Figure 6.5: Excess heat capacity evolution with temperature for all intermediate compositions. The solid curve shows the Schottky contribution obtained from that calculated pure PuO$_2$ (see text) and scaled to the PuO$_2$ concentration in the solid solution.

The high temperature range ((T/K) > 250)

The irregularities of the heat capacity values above 250 K are the result of limited resolution due to the Stycast encapsulation and lower precision due to the reduced amount of materials. To derive the smoothed values, the studied temperature range was fitted by a polynomial equation together with the enthalpy data measurements (476 < (T/K)

< 1790) of our previous work [10] using the simultaneous linear regression. We thus obtained the heat capacity value at T = 298.15 K corresponding to each intermediate composition. In table 6.3 the $C_P(298.15K)$ values of all intermediate compositions are listed together with the constants for the fit equations of the low temperature heat capacity results obtained in this study [10].

Based on low- and high-temperature heat capacity functions, no excess heat capacity is revealed for the high temperature region, as concluded also before in our previous study.

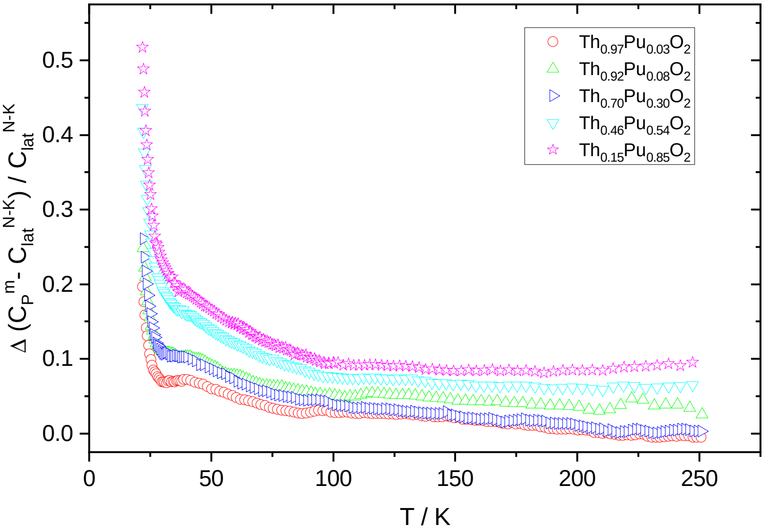

Figure 6.6: The relative excess heat capacity evolution with temperature for the investigated intermediate compositions.

6.4. Summary and Conclusions

The low temperature heat capacity of $(Th_{1-y},Pu_y)O_2$ solid solution with y = 0.03, 0.08, 0.30, 0.54 and 0.85 have been measured from a minimum of 3.6 K up to about 300 K using a Quantum Design PPMS system. The results indicate a non-ideal behaviour of the heat capacity due to the affected phonon frequencies of the solid solution compared to the end members caused by the mass difference and lattice strain (ionic radius difference) of Pu^{4+} and Th^{4+} substitution on the cation sublattice. This effect is the strongest at very low temperatures, and diminishes with increasing temperature. Also the effect of the Schottky contribution caused by breaking of the degeneracy of the $^4I_5$ electronic ground state of the Pu^{4+} ion to the excess heat capacity could be demonstrated, and is evident above T = 100 K for the samples with 54 and 85 wt.% PuO_2.

The heat capacity of $^{239}PuO_2$ has also been measured in this study and the results are indicating a very good agreement with the data published by Flotow *et al.* [11] for $^{242}PuO_2$ and $^{244}PuO_2$ over the entire temperature range, while the data presented by

Sandenaw [12] are considerably higher for the temperature range up to 30 K. Sandenaw shows in his paper that the heat capacity obtained up to 100 K is irreproducible and the peaks observed are mainly caused by the radiation damage. With our results we confirm the absence of anomalies for the measured temperature range. The substantial residual entropy at T = 0 K strongly suggests that his measurements were affected by radiation damage, specially below 20 K. We argue that the lattice disorder is not the source of the anomalies observed in that work, since they were not present in the low-temperature heat capacity of the (U,Am)O_{2-x} system [21] that is strongly affected by the ^{241}Am decay.

Table 6.4: Low-temperature heat capacity values of PuO_2 end-member measured in this study.

T_m / K	$C_P/(J \cdot mol^{-1} \cdot K^{-1})$	T_m / K	$C_P/(J \cdot mol^{-1} \cdot K^{-1})$	T_m / K	$C_P/(J \cdot mol^{-1} \cdot K^{-1})$	T_m / K	$C_P/(J \cdot mol^{-1} \cdot K^{-1})$
5.81	0.0322	60.40	14.2957	131.67	35.5592	203.09	51.6480
5.85	0.0338	61.40	14.6258	132.65	35.7513	204.09	51.8756
5.90	0.0325	62.40	14.9535	133.67	36.0645	205.10	52.0784
5.96	0.0327	63.42	15.2859	134.67	36.3182	206.11	52.1884
6.02	0.0345	64.42	15.6059	135.68	36.5618	207.11	52.3418
6.11	0.0377	65.42	15.9228	136.68	36.8319	208.11	52.5178
6.20	0.0403	66.42	16.2562	137.68	37.1070	209.12	52.6189
6.30	0.0410	67.44	16.5876	138.69	37.3713	210.12	52.8177
6.43	0.0428	68.44	16.9102	139.70	37.6263	211.13	52.9982
6.57	0.0439	69.44	17.2244	140.71	37.8700	212.14	53.2421
6.75	0.0486	70.45	17.5406	141.72	38.1261	213.15	53.4007
6.95	0.0532	71.44	17.8393	142.72	38.3778	214.15	53.5464
7.18	0.0584	72.45	18.1507	143.73	38.6196	215.16	53.7306
7.43	0.0646	73.45	18.4519	144.72	38.8646	216.16	53.7980
7.72	0.0724	74.45	18.7506	145.74	39.1043	217.16	53.9270
8.05	0.0824	75.45	19.0430	146.74	39.3599	218.17	54.0759
8.44	0.0932	76.46	19.3526	147.75	39.5946	219.18	54.1614
8.96	0.1106	77.47	19.6598	148.76	39.8439	220.18	54.2828
9.44	0.1269	78.48	19.9694	149.76	40.0626	221.19	54.4229
10.00	0.1502	79.49	20.2753	150.76	40.2892	222.19	54.5984
10.57	0.1757	80.49	20.5894	151.77	40.5127	223.20	54.7941
11.22	0.2067	81.49	20.8800	152.77	40.7560	224.20	55.0111
12.02	0.2474	82.49	21.1770	153.78	40.9845	225.21	55.2843
12.74	0.3036	83.49	21.4570	154.79	41.2203	226.20	55.5102
13.53	0.3636	84.49	21.7528	155.79	41.4588	227.22	55.8185
14.69	0.4693	85.49	22.0465	156.80	41.6832	228.22	56.0487
15.51	0.5552	86.49	22.3470	157.81	41.9276	229.23	56.2324
16.93	0.7336	87.49	22.6554	158.81	42.1655	230.23	56.3427
17.95	0.8830	88.50	22.9820	159.82	42.3791	231.24	56.5221
19.56	1.1536	89.50	23.3130	160.82	42.6308	232.24	56.7248
20.37	1.3167	90.50	23.6237	161.83	42.8387	233.25	56.8674
21.55	1.5115	91.49	23.9191	162.83	43.0720	234.26	57.0568
22.32	1.6944	92.48	24.2213	163.84	43.3002	235.26	57.2293
23.48	1.9696	93.48	24.5306	164.85	43.5262	236.26	57.4278
24.33	2.1833	94.48	24.8419	165.85	43.7335	237.28	57.6519
25.40	2.4636	95.49	25.1555	166.85	43.9726	238.29	57.7398
26.32	2.7272	96.50	25.4643	167.86	44.1874	239.30	57.9187
27.30	3.0086	97.51	25.7677	168.87	44.4126	240.30	58.0726
28.29	3.3120	98.51	26.0720	169.87	44.6440	241.31	58.2397
29.30	3.6347	99.51	26.3927	170.88	44.8678	242.32	58.4087
30.28	3.9392	100.53	26.7075	171.88	45.0946	243.33	58.5775
30.44	4.0646	101.54	27.0062	172.89	45.3175	244.34	58.6848
31.41	4.3938	102.54	27.3171	173.89	45.5390	245.34	58.8521
32.38	4.7220	103.54	27.6132	174.89	45.7769	246.35	58.9504
33.36	5.0570	104.56	27.9346	175.90	46.0312	247.35	59.1016
34.34	5.3993	105.56	28.2229	176.91	46.2386	248.37	59.2295
35.32	5.7433	106.56	28.5139	177.91	46.4194	249.36	59.3815
36.32	6.0867	107.57	28.8025	178.92	46.6954	250.38	59.5373
37.32	6.4422	108.57	29.1007	179.92	46.8813	251.38	59.7010
38.32	6.7794	109.57	29.3914	180.93	47.1091	252.40	59.7478
39.33	7.1160	110.57	29.6824	181.93	47.3538	253.40	59.8604
40.33	7.4603	111.58	29.9865	182.94	47.5385	254.40	59.9411
41.34	7.8048	112.58	30.2759	183.94	47.7441	255.41	59.9889
42.34	8.1634	113.59	30.5612	184.95	47.9363	256.41	60.0906
43.36	8.5083	114.59	30.8356	185.95	48.1118	257.43	60.1534
44.36	8.8518	115.60	31.1446	186.96	48.3599	258.42	60.2711
45.36	9.2011	116.60	31.4386	187.96	48.5382	259.44	60.4101
46.36	9.5477	117.61	31.7117	188.97	48.7526	260.44	60.5769
47.37	9.9018	118.61	31.9964	189.97	48.9743	261.45	60.7049
48.37	10.2548	119.61	32.2727	190.98	49.2133	262.44	60.8701
49.37	10.6058	120.62	32.5413	191.98	49.4316	263.46	61.0585
50.37	10.9610	121.62	32.8201	193.00	49.6518	264.46	61.1739
51.38	11.2847	122.64	33.0996	194.00	49.8666	265.46	61.1481
52.38	11.6253	123.63	33.3627	195.01	50.0842	266.47	61.3049
53.38	11.9754	124.64	33.6498	196.02	50.2817	267.49	61.3919
54.38	12.3105	125.64	33.9282	197.03	50.4535	268.48	61.5201
55.38	12.6428	126.65	34.1695	198.03	50.6395	269.49	61.5592
56.39	12.9750	127.64	34.4065	199.05	50.9013	270.49	61.6984
57.39	13.3095	128.65	34.6698	200.06	51.0691		
58.39	13.6401	129.66	34.9365	201.07	51.2693		
59.39	13.9643	130.66	35.1853	202.08	51.4946		

Table 6.5: Low-temperature heat capacity values of $Th_{0.97}Pu_{0.03}O_2$ intermediate composition.

T_m / K	$C_P/(J \cdot mol^{-1} \cdot K^{-1})$	T_m / K	$C_P/(J \cdot mol^{-1} \cdot K^{-1})$	T_m / K	$C_P/(J \cdot mol^{-1} \cdot K^{-1})$	T_m / K	$C_P/(J \cdot mol^{-1} \cdot K^{-1})$
7.34	0.0519	24.38	2.1622	97.44	26.2436	195.22	49.4596
7.38	0.0526	24.87	2.2888	99.19	26.7283	196.92	49.7956
7.50	0.0571	25.38	2.4301	100.87	27.2299	198.59	50.0821
7.58	0.0571	25.87	2.5625	102.56	27.7348	200.29	50.3040
7.66	0.0592	26.36	2.6990	104.23	28.2561	201.97	50.6364
7.97	0.0661	26.90	2.8629	105.92	28.7674	203.65	50.8921
8.13	0.0694	27.46	3.0328	107.60	29.2383	205.34	51.1791
8.27	0.0731	28.03	3.2049	109.29	29.7183	207.02	51.3355
8.44	0.0772	28.63	3.3921	110.98	30.2070	208.72	51.6023
8.59	0.0812	29.21	3.5708	112.66	30.7277	210.40	51.8292
8.76	0.0867	29.84	3.7692	114.34	31.2065	212.09	52.1269
8.91	0.0911	30.46	3.9721	116.03	31.6702	213.78	52.3451
9.09	0.0965	31.09	4.1807	117.71	32.1596	215.46	52.5618
9.26	0.1007	31.72	4.3881	119.40	32.6291	217.15	52.7646
9.44	0.1079	32.32	4.6009	121.08	33.1101	218.82	53.0134
9.61	0.1133	33.06	4.8559	122.77	33.5463	220.51	53.2977
9.81	0.1206	33.67	5.0576	124.45	34.0134	222.18	53.5439
9.99	0.1276	34.45	5.3253	126.14	34.4579	223.87	53.8097
10.20	0.1354	35.06	5.5380	127.82	34.9520	225.55	54.1359
10.38	0.1428	35.82	5.8075	129.50	35.4265	227.24	54.3213
10.60	0.1516	36.53	6.0597	131.19	35.8511	228.91	54.4449
10.79	0.1597	37.30	6.3285	132.87	36.2663	230.59	54.5993
11.02	0.1702	38.08	6.5992	134.55	36.7329	232.28	54.8156
11.22	0.1801	38.86	6.8910	136.26	37.0951	233.95	55.0431
11.46	0.1919	40.07	7.3189	137.90	37.5011	235.65	55.323
11.66	0.2030	41.75	7.9091	139.72	38.0213	237.33	55.5652
11.92	0.2173	43.45	8.5015	141.30	38.3499	239.01	55.8313
12.13	0.2287	45.14	9.0941	142.99	38.7822	240.7	56.0162
12.39	0.2446	46.83	9.6908	144.68	39.2136	242.38	56.2859
12.61	0.2576	48.53	10.2706	146.35	39.6748	244.06	56.4578
12.89	0.2756	50.22	10.8478	148.04	40.0576	245.74	56.6633
13.12	0.2924	51.91	11.4435	149.72	40.4204	247.42	56.7555
13.40	0.3123	53.60	12.0222	151.41	40.8784	249.1	56.9498
13.65	0.3304	55.29	12.6005	153.08	41.1588	250.77	57.1464
13.94	0.3531	56.98	13.1710	154.77	41.5533	252.45	57.3761
14.20	0.3751	58.67	13.7456	156.46	41.9333	254.14	57.4984
14.51	0.4013	60.35	14.3033	158.14	42.2907	255.82	57.6173
14.77	0.4271	62.04	14.8540	159.82	42.6837	257.5	57.7489
15.10	0.4581	63.73	15.4312	161.52	43.0533	259.19	57.8771
15.37	0.4887	65.41	15.9994	163.20	43.3582	260.86	58.063
17.02	0.6714	67.07	16.5512	164.88	43.7352	262.54	58.2058
17.33	0.7271	68.76	17.0921	166.56	44.1147	264.22	58.3775
17.71	0.7846	70.47	17.6468	168.25	44.4291	265.9	58.5509
18.05	0.8341	72.16	18.1949	169.93	44.7403	267.58	58.6377
18.43	0.8930	73.86	18.7230	171.62	45.0761	269.26	58.7669
18.79	0.9522	75.53	19.2567	173.30	45.5227	270.94	58.844
19.20	1.0287	77.22	19.7919	174.99	45.8002	272.62	58.9164
19.56	1.0824	78.91	20.3257	176.68	46.1830	274.3	58.9301
19.87	1.1447	80.60	20.8688	178.37	46.4410	275.97	58.9234
20.27	1.2218	82.29	21.4104	180.05	46.7630	277.66	59.0086
20.68	1.3009	83.97	21.9241	181.73	47.0967	279.33	59.0714
21.11	1.3910	85.66	22.4384	183.42	47.4578	281.01	59.1622
21.55	1.4821	87.34	22.9648	185.11	47.6873	282.68	59.2582
22.00	1.5794	89.03	23.5226	186.79	47.9868	284.37	59.4795
22.45	1.6856	90.71	24.0878	188.48	48.2357	286.03	59.5766
22.92	1.7953	92.40	24.6501	190.16	48.5596	287.75	59.8499
23.41	1.9133	94.08	25.2125	191.85	48.8441	289.33	60.1186
23.88	2.0353	95.77	25.7138	193.54	49.1545	291.94	60.8698

Table 6.6: Low-temperature heat capacity values of $Th_{0.92}Pu_{0.08}O_2$ intermediate composition.

T_m / K	$C_P/(J \cdot mol^{-1} \cdot K^{-1})$	T_m / K	$C_P/(J \cdot mol^{-1} \cdot K^{-1})$	T_m / K	$C_P/(J \cdot mol^{-1} \cdot K^{-1})$	T_m / K	$C_P/(J \cdot mol^{-1} \cdot K^{-1})$
3.58	0.0080	6.65	0.0446	17.62	0.8086	68.39	17.4037
3.60	0.0077	6.73	0.0469	17.87	0.8491	69.80	17.8730
3.62	0.0083	6.81	0.0483	18.14	0.8904	71.23	18.3423
3.64	0.0083	6.90	0.0507	18.41	0.9356	72.68	18.8419
3.66	0.0086	6.98	0.0520	18.68	0.9815	74.17	19.3462
3.67	0.0085	7.07	0.0542	18.96	1.0269	75.70	19.8614
3.69	0.0086	7.16	0.0563	19.25	1.0761	77.24	20.3841
3.71	0.0088	7.25	0.0574	19.40	1.1058	78.84	20.9245
3.73	0.0092	7.35	0.0594	19.47	1.1188	80.45	21.4291
3.75	0.0091	7.44	0.0620	19.81	1.1653	82.10	21.9712
3.77	0.0093	7.54	0.0645	20.07	1.2439	83.79	22.5030
3.80	0.0094	7.66	0.0679	20.46	1.3210	85.50	23.0600
3.82	0.0096	7.68	0.0681	20.88	1.4108	87.25	23.6000
3.84	0.0099	7.78	0.0711	21.29	1.5000	89.04	24.1747
3.87	0.0097	7.88	0.0740	21.69	1.5917	90.86	24.7372
3.89	0.0103	7.99	0.0764	22.15	1.6950	92.72	25.3003
3.92	0.0104	8.09	0.0781	22.61	1.8010	94.63	25.9060
3.94	0.0104	8.20	0.0820	23.05	1.9173	96.56	26.4722
3.97	0.0105	8.31	0.0847	23.53	2.0373	98.55	27.1214
4.00	0.0104	8.42	0.0875	23.99	2.1578	100.56	27.7218
4.03	0.0106	8.53	0.0907	24.48	2.2898	102.62	28.3346
4.05	0.0107	8.65	0.0950	24.96	2.4243	104.73	28.9451
4.08	0.0114	8.77	0.0980	25.47	2.5643	106.90	29.6310
4.11	0.0117	8.89	0.1023	25.97	2.7099	109.07	30.3004
4.14	0.0117	9.00	0.1060	26.51	2.8676	111.32	31.0234
4.17	0.0118	9.13	0.1097	27.03	3.0257	113.61	31.7747
4.20	0.0124	9.25	0.1151	27.59	3.1981	115.93	32.4629
4.24	0.0120	9.38	0.1192	28.12	3.3658	118.32	33.1464
4.27	0.0128	9.51	0.1245	28.72	3.5558	120.74	33.8299
4.31	0.0133	9.64	0.1294	29.29	3.7400	123.22	34.5232
4.34	0.0132	9.78	0.1343	29.90	3.9404	125.76	35.2136
4.38	0.0140	9.91	0.1397	30.49	4.1401	128.34	35.9482
4.41	0.0139	10.05	0.1452	31.13	4.3573	130.98	36.6778
4.45	0.0147	10.19	0.1505	31.73	4.5667	133.67	37.3781
4.49	0.0150	10.33	0.1577	32.39	4.7952	136.42	38.0745
4.53	0.0150	10.49	0.1595	33.06	5.0279	139.22	38.7763
4.57	0.0157	10.64	0.1667	33.73	5.2637	142.08	39.4978
4.61	0.0166	10.79	0.1736	34.39	5.5000	145.00	40.2289
4.65	0.0158	10.94	0.1817	35.09	5.7414	147.98	40.9359
4.69	0.0160	11.09	0.1904	35.78	5.9778	151.01	41.6236
4.73	0.0173	11.25	0.1980	36.50	6.2361	154.12	42.3802
4.78	0.0173	11.41	0.2065	37.27	6.5005	157.29	43.1199
4.83	0.0178	11.57	0.2157	38.05	6.7952	160.53	43.8794
4.87	0.0184	11.74	0.2252	38.83	7.0786	163.82	44.6220
4.92	0.0190	11.91	0.2346	39.62	7.3717	167.18	45.4194
4.97	0.0195	12.08	0.2463	40.42	7.6667	170.62	46.1055
5.02	0.0202	12.25	0.2568	41.24	7.9701	174.12	46.8621
5.07	0.0207	12.43	0.2677	42.09	8.2649	177.70	47.6265
5.12	0.0217	12.60	0.2797	42.95	8.5773	181.34	48.2925
5.17	0.0225	12.79	0.2928	43.83	8.8987	185.07	49.0606
5.23	0.0237	12.97	0.3059	44.72	9.2258	188.88	49.7760
5.28	0.0238	13.16	0.3190	45.63	9.5533	192.76	50.5167
5.34	0.0245	13.35	0.3352	46.56	9.8892	196.72	51.2409
5.39	0.0253	13.54	0.3492	47.51	10.2231	200.77	51.9253
5.45	0.0262	13.74	0.3653	48.48	10.5601	204.88	52.4762
5.51	0.0268	13.93	0.3820	49.47	10.9134	209.08	53.1446
5.57	0.0278	14.13	0.3990	50.49	11.2663	213.39	53.9642
5.64	0.0281	14.35	0.4181	51.52	11.6283	217.78	54.9925
5.70	0.0293	14.54	0.4368	52.57	11.9926	222.25	56.1606
5.77	0.0308	14.78	0.4613	53.65	12.3551	226.81	56.7593
5.83	0.0317	14.96	0.4804	54.74	12.7259	231.47	57.0422
5.90	0.0324	15.22	0.5079	55.87	13.1147	236.22	57.7815
5.97	0.0330	15.41	0.5265	57.01	13.5177	241.07	58.4294
6.04	0.0348	15.67	0.5577	58.17	13.9244	246.01	58.7994
6.11	0.0352	15.87	0.5799	59.36	14.3531	251.06	58.8857
6.18	0.0367	16.14	0.6125	60.58	14.7893	256.21	58.7838
6.26	0.0384	16.35	0.6386	61.81	15.2175	261.45	59.0914
6.33	0.0397	16.61	0.6745	63.08	15.6514	266.81	59.8998
6.41	0.0409	16.86	0.7020	64.37	16.0823	272.27	60.7518
6.49	0.0422	17.08	0.7337	65.68	16.5141		
6.57	0.0439	17.37	0.7729	67.03	16.9526		

Table 6.7: Low-temperature heat capacity values of $Th_{0.70}Pu_{0.30}O_2$ intermediate composition.

T_m / K	C_P/($J \cdot mol^{-1} \cdot K^{-1}$)	T_m / K	C_P/($J \cdot mol^{-1} \cdot K^{-1}$)	T_m / K	C_P/($J \cdot mol^{-1} \cdot K^{-1}$)	T_m / K	C_P/($J \cdot mol^{-1} \cdot K^{-1}$)
6.55	0.0418	10.60	0.1720	43.61	8.8348	170.01	44.7386
6.56	0.0429	10.75	0.1798	45.45	9.4697	171.69	45.1402
6.57	0.0439	10.90	0.1873	46.99	10.0356	173.38	45.5412
6.58	0.0423	11.06	0.1959	48.84	10.6823	175.06	45.9120
6.59	0.0425	11.23	0.2056	50.53	11.2745	176.75	46.2929
6.60	0.0417	11.39	0.2140	52.21	11.8649	178.43	46.7177
6.61	0.0432	11.56	0.2231	53.89	12.4441	180.11	46.9741
6.62	0.0436	11.74	0.2351	55.58	13.0409	181.80	47.2700
6.63	0.0437	11.92	0.2460	57.27	13.6068	183.48	47.6493
6.65	0.0440	12.10	0.2566	58.94	14.1818	185.16	47.9663
6.66	0.0450	12.30	0.2691	60.63	14.7180	186.85	48.2661
6.67	0.0445	12.48	0.2817	62.31	15.2824	188.53	48.4596
6.69	0.0468	12.67	0.2962	63.94	15.8370	190.22	48.7991
6.70	0.0452	12.96	0.3161	65.67	16.4043	191.91	49.0856
6.72	0.0460	13.02	0.3213	67.35	16.9680	193.60	49.4066
6.73	0.0470	13.42	0.3524	69.03	17.5134	195.28	49.7234
6.75	0.0458	13.51	0.3599	70.72	18.0579	196.97	50.0092
6.77	0.0465	13.85	0.3886	72.40	18.6314	198.65	50.3012
6.79	0.0472	13.91	0.3947	74.05	19.1586	200.33	50.4865
6.81	0.0460	14.35	0.4351	75.73	19.6823	202.02	50.7744
6.83	0.0485	14.42	0.4410	77.42	20.2242	203.73	51.0040
6.85	0.0480	14.83	0.4839	79.10	20.7806	205.41	51.2368
6.87	0.0477	14.91	0.4921	80.79	21.3115	207.09	51.4995
6.89	0.0487	15.36	0.5406	82.47	21.8602	208.77	51.6956
6.92	0.0486	15.43	0.5495	84.15	22.3917	210.45	52.0050
6.94	0.0502	15.90	0.6054	85.83	22.8937	212.15	52.1227
6.97	0.0502	15.99	0.6172	87.51	23.4243	213.83	52.4846
6.99	0.0525	16.48	0.6825	89.19	23.9486	215.51	52.6139
7.02	0.0514	16.57	0.6951	90.87	24.4964	217.20	52.8172
7.05	0.0514	17.08	0.7496	92.55	25.0347	218.87	53.1351
7.08	0.0533	17.17	0.7626	94.23	25.5689	220.56	53.4110
7.11	0.0538	17.69	0.8471	95.92	26.0741	222.24	53.7528
7.14	0.0539	17.90	0.8819	97.59	26.5691	223.94	54.0721
7.18	0.0554	18.34	0.9499	99.34	27.0358	225.62	54.3354
7.22	0.0547	18.58	0.9867	101.02	27.4935	227.30	54.4551
7.25	0.0566	19.00	1.0618	102.70	28.0016	228.98	54.6698
7.29	0.0573	19.36	1.1363	104.37	28.5089	230.66	54.8001
7.33	0.0568	19.83	1.2082	106.05	28.9814	232.34	54.9913
7.37	0.0585	19.93	1.2377	107.73	29.4462	234.03	55.2820
7.41	0.0591	20.59	1.3733	109.42	29.9209	235.71	55.5648
7.46	0.0624	20.98	1.4615	111.10	30.4190	237.40	55.8137
7.51	0.0626	21.38	1.5486	112.79	30.9146	239.08	56.1027
7.55	0.0631	21.80	1.6408	114.47	31.3804	240.77	56.3339
7.61	0.0640	22.22	1.7398	116.16	31.8523	242.44	56.6139
7.66	0.0655	22.65	1.8422	117.83	32.3192	244.12	56.8149
7.71	0.0659	23.09	1.9548	119.52	32.7774	245.80	56.9695
7.77	0.0679	23.54	2.0695	121.20	33.2672	247.49	57.0664
7.83	0.0704	24.00	2.1922	122.88	33.7317	249.17	57.2869
7.89	0.0710	24.47	2.3161	124.57	34.1732	250.84	57.4727
7.95	0.0722	24.95	2.4508	126.25	34.6386	252.52	57.5628
8.01	0.0734	25.44	2.5860	127.93	35.0476	254.20	57.7017
8.08	0.0767	25.94	2.7330	129.62	35.4854	255.88	57.8328
8.15	0.0798	26.42	2.8666	131.30	35.9145	257.56	57.9381
8.22	0.0802	26.87	3.0066	132.98	36.3760	259.24	58.0830
8.29	0.0836	27.47	3.1847	134.67	36.7730	260.93	58.2112
8.37	0.0867	27.95	3.3382	136.35	37.1904	262.60	58.4331
8.45	0.0887	28.51	3.5217	138.03	37.6179	264.29	58.6235
8.53	0.0922	29.08	3.7021	139.72	38.0584	265.96	58.7650
8.61	0.0936	29.71	3.9076	141.40	38.4487	267.63	58.8229
8.70	0.0974	30.24	4.0790	143.09	38.8784	269.33	58.8046
8.79	0.0988	30.88	4.2973	144.77	39.3084	271.00	58.8430
8.88	0.1029	31.47	4.5073	146.45	39.8307	272.68	58.9322
9.00	0.1061	32.09	4.7308	148.13	40.0654	274.35	58.6594
9.12	0.1107	32.75	4.9517	149.81	40.4784	276.03	58.6243
9.26	0.1158	33.40	5.1676	151.50	40.8168	277.71	58.5529
9.33	0.1185	34.08	5.4111	153.17	41.1773	279.39	58.5596
9.48	0.1230	34.76	5.6541	154.86	41.5046	281.05	58.6305
9.56	0.1269	35.47	5.9146	156.54	41.9326	282.73	58.7453
9.72	0.1341	36.19	6.1733	158.22	42.2863	284.40	58.9684
9.80	0.1374	36.93	6.4395	159.90	42.6243	286.08	59.2600
9.92	0.1421	37.68	6.6992	161.59	43.0412	287.77	59.4593
10.05	0.1475	38.47	6.9933	163.27	43.4307	289.39	59.5632
10.18	0.1534	39.19	7.2543	164.96	43.8305	291.91	60.7324
10.32	0.1589	40.23	7.6321	166.64	44.1244		
10.46	0.1659	41.91	8.2305	168.32	44.4363		

Table 6.8: Low-temperature heat capacity values of $Th_{0.46}Pu_{0.54}O_2$ intermediate composition.

T_m / K	$C_P/(J \cdot mol^{-1} \cdot K^{-1})$	T_m / K	$C_P/(J \cdot mol^{-1} \cdot K^{-1})$	T_m / K	$C_P/(J \cdot mol^{-1} \cdot K^{-1})$	T_m / K	$C_P/(J \cdot mol^{-1} \cdot K^{-1})$
7.25	0.0678	9.40	0.1452	24.81	2.6814	84.98	23.5440
7.26	0.0702	9.48	0.1487	25.22	2.7968	86.70	24.0960
7.27	0.0682	9.60	0.1545	25.69	2.9416	88.45	24.6120
7.28	0.0680	9.70	0.1587	26.14	3.0759	90.23	25.1600
7.29	0.0694	9.80	0.1620	26.63	3.2257	92.05	25.6970
7.29	0.0696	9.90	0.1698	27.11	3.3780	93.91	26.2680
7.30	0.0707	10.01	0.1730	27.61	3.5442	95.81	26.8470
7.31	0.0701	10.12	0.1788	28.11	3.6997	97.75	27.4630
7.32	0.0701	10.24	0.1848	28.64	3.8846	99.73	28.0770
7.33	0.0701	10.36	0.1923	29.16	4.0599	101.75	28.7060
7.34	0.0716	10.48	0.1994	29.69	4.2434	103.81	29.3280
7.35	0.0695	10.61	0.2031	30.25	4.4295	105.92	29.9690
7.36	0.0710	10.73	0.2120	30.81	4.6315	108.07	30.6250
7.37	0.0714	10.87	0.2207	31.39	4.8361	110.27	31.2920
7.39	0.0727	11.01	0.2298	31.99	5.0506	112.51	31.9990
7.40	0.0719	11.15	0.2377	32.59	5.2625	114.79	32.6600
7.41	0.0725	11.30	0.2434	33.21	5.4814	117.13	33.3830
7.43	0.0749	11.45	0.2552	33.83	5.7086	119.50	34.0360
7.44	0.0739	11.62	0.2614	34.48	5.9399	121.94	34.7470
7.46	0.0740	11.78	0.2740	35.14	6.1825	124.42	35.4530
7.47	0.0742	11.95	0.2847	35.82	6.4275	126.95	36.1780
7.49	0.0766	12.12	0.2990	36.51	6.6893	129.54	36.9020
7.50	0.0745	12.29	0.3131	37.21	6.9587	132.18	37.6420
7.52	0.0752	12.47	0.3274	37.94	7.2144	134.87	38.2920
7.54	0.0767	12.66	0.3420	38.67	7.5111	137.62	39.0150
7.56	0.0774	12.85	0.3567	39.41	7.7693	140.42	39.6790
7.58	0.0795	13.05	0.3746	40.21	8.0712	143.28	40.4080
7.60	0.0767	13.25	0.3955	41.00	8.3747	146.20	41.1690
7.62	0.0795	13.46	0.4139	41.77	8.6657	149.18	41.8670
7.64	0.0797	13.67	0.4345	42.61	8.9748	152.22	42.6750
7.67	0.0802	13.89	0.4553	43.44	9.2766	155.33	43.4190
7.69	0.0805	14.11	0.4798	44.30	9.5899	158.51	44.1140
7.72	0.0817	14.34	0.5035	45.17	9.9116	161.74	44.8850
7.74	0.0825	14.58	0.5310	46.05	10.2380	165.03	45.6460
7.77	0.0833	14.82	0.5571	46.96	10.5700	168.40	46.4000
7.80	0.0832	15.07	0.5851	47.88	10.8990	171.83	47.1910
7.83	0.0873	15.32	0.6164	48.83	11.2380	175.36	47.9690
7.86	0.0879	15.59	0.6496	49.78	11.5880	178.93	48.7510
7.90	0.0879	15.85	0.6835	50.77	11.9440	182.59	49.4780
7.93	0.0880	16.13	0.7232	51.78	12.3000	186.31	50.1540
7.97	0.0887	16.41	0.7665	52.80	12.6730	190.12	50.9020
8.00	0.0910	16.70	0.8076	53.84	13.0360	194.01	51.6880
8.04	0.0935	16.99	0.8512	54.92	13.4270	197.97	52.4750
8.08	0.0942	17.29	0.8973	56.01	13.8080	202.02	53.2200
8.12	0.0949	17.61	0.9545	57.13	14.2110	206.14	53.8930
8.17	0.0959	17.92	1.0079	58.26	14.6070	210.35	54.5680
8.21	0.0965	18.25	1.0664	59.42	15.0240	214.64	55.5330
8.26	0.1003	18.58	1.1319	60.61	15.4350	219.02	56.3290
8.31	0.1011	18.92	1.1965	61.82	15.8610	223.48	56.9990
8.36	0.1029	19.27	1.2680	63.06	16.2880	228.04	57.5860
8.41	0.1054	19.63	1.3464	64.31	16.7220	232.69	58.2930
8.47	0.1073	19.99	1.4260	65.60	17.1500	237.45	59.0320
8.53	0.1093	20.23	1.4872	66.91	17.6010	242.30	59.7520
8.59	0.1124	20.55	1.5588	68.25	18.0620	247.23	60.4390
8.64	0.1135	20.90	1.6406	69.63	18.5020	252.27	61.0470
8.71	0.1162	21.24	1.7175	71.02	18.9660	257.41	61.5100
8.77	0.1186	21.61	1.8066	72.44	19.4550	262.68	62.2700
8.84	0.1213	21.96	1.8934	73.90	19.9360	268.04	62.8740
8.91	0.1240	22.35	1.9959	75.39	20.4650	273.50	63.3900
8.99	0.1264	22.72	2.0873	76.91	20.9430	279.09	63.6940
9.06	0.1290	23.13	2.2026	78.46	21.4490	284.78	64.2500
9.14	0.1323	23.51	2.3054	80.04	21.9390	290.58	65.2380
9.22	0.1367	23.95	2.4307	81.65	22.4870	297.39	66.1110
9.31	0.1427	24.35	2.5433	83.30	23.0140		

Table 6.9: Low-temperature heat capacity values of $Th_{0.15}Pu_{0.85}O_2$ intermediate composition.

T_m / K	$C_P/(J \cdot mol^{-1} \cdot K^{-1})$	T_m / K	$C_P/(J \cdot mol^{-1} \cdot K^{-1})$	T_m / K	$C_P/(J \cdot mol^{-1} \cdot K^{-1})$	T_m / K	$C_P/(J \cdot mol^{-1} \cdot K^{-1})$
8.05	0.1210	22.98	2.2877	61.87	16.2530	119.76	34.5750
8.07	0.1220	23.34	2.3832	62.31	16.4360	122.19	35.2650
8.09	0.1201	23.68	2.4839	63.07	16.6710	124.66	35.9670
8.11	0.1211	24.06	2.5936	63.54	16.8590	127.19	36.7200
8.13	0.1231	24.43	2.7028	64.28	17.0980	129.77	37.4230
8.16	0.1239	24.83	2.8215	64.78	17.2910	132.40	38.1340
8.19	0.1241	25.21	2.9384	65.52	17.5090	135.09	38.8440
8.22	0.1254	25.63	3.0564	66.06	17.7210	137.83	39.4920
8.26	0.1284	26.03	3.1885	66.79	17.9350	140.63	40.2690
8.29	0.1290	26.47	3.3246	67.37	18.1480	143.48	40.9890
8.33	0.1303	26.89	3.4446	68.09	18.3750	146.39	41.7190
8.38	0.1321	27.36	3.5984	68.70	18.5860	149.36	42.4540
8.43	0.1339	27.80	3.7597	69.41	18.8090	152.40	43.2270
8.48	0.1361	28.27	3.9268	70.06	19.0690	155.50	44.0610
8.54	0.1374	28.73	4.0831	70.76	19.2600	158.67	44.7920
8.61	0.1407	29.23	4.2569	71.45	19.5280	161.90	45.5860
8.68	0.1422	29.73	4.4345	72.14	19.7260	165.18	46.4200
8.76	0.1455	30.25	4.6198	72.87	19.9960	168.55	47.1370
8.84	0.1493	30.77	4.8067	73.54	20.2040	171.96	47.9740
8.94	0.1523	31.29	4.9970	74.32	20.4780	175.47	48.7170
9.04	0.1570	31.84	5.1995	74.98	20.6690	179.04	49.5060
9.15	0.1619	32.40	5.3968	75.80	20.9660	182.69	50.2310
9.28	0.1665	32.98	5.6075	76.44	21.1510	186.41	50.9450
9.41	0.1719	33.56	5.8216	77.32	21.4940	190.20	51.7940
9.56	0.1802	34.15	6.0614	77.94	21.6320	194.08	52.6570
9.72	0.1885	34.76	6.2616	78.86	21.9880	198.04	53.4670
9.89	0.1970	35.39	6.5060	79.47	22.1640	202.08	54.1830
10.06	0.2056	36.03	6.7366	80.43	22.5170	206.20	54.9890
10.29	0.2168	36.69	6.9528	81.03	22.6450	210.40	55.6920
10.51	0.2295	37.36	7.2408	82.04	23.0140	214.68	56.5850
10.75	0.2434	38.05	7.5079	82.61	23.1800	219.06	57.4320
11.00	0.2581	38.74	7.7845	83.68	23.5140	223.51	58.1830
11.27	0.2758	39.45	8.0528	84.23	23.6250	228.07	58.9330
11.57	0.2971	40.20	8.3261	85.36	24.0670	232.72	59.7050
11.89	0.3199	40.92	8.5955	85.88	24.2110	237.46	60.5250
12.23	0.3506	41.70	8.8994	87.06	24.5920	242.31	61.0460
12.60	0.3817	42.47	9.1899	87.57	24.7480	247.24	61.9640
12.99	0.4174	43.26	9.4895	88.81	25.1680	252.27	62.6390
13.41	0.4656	44.07	9.7843	89.28	25.2610	257.41	63.1600
13.85	0.4981	44.90	10.1030	90.58	25.6890	262.66	63.8510
14.32	0.5484	45.74	10.4140	91.03	25.8180	268.01	64.4840
14.83	0.5990	46.60	10.7310	92.39	26.2580	273.48	65.1170
15.36	0.6478	47.47	11.0450	92.82	26.3400	279.04	65.5150
15.93	0.7157	48.38	11.3960	94.25	26.8060	284.73	66.1450
16.53	0.7990	49.29	11.7340	94.64	26.8910	290.53	67.9420
17.17	0.8945	50.22	12.0740	96.14	27.3610	296.61	70.4100
17.85	1.0057	51.17	12.4200	96.51	27.4350		
18.55	1.1311	52.15	12.7650	98.08	27.9770		
19.31	1.2795	53.13	13.1320	98.41	28.0490		
20.09	1.4420	54.15	13.4880	100.05	28.6130		
20.16	1.4682	55.18	13.8630	100.46	28.7250		
20.54	1.5530	56.24	14.2360	102.06	29.2640		
20.90	1.6401	57.32	14.6240	104.12	29.8140		
21.29	1.7343	58.42	15.0180	106.22	30.5130		
21.65	1.8255	58.77	15.1750	108.37	31.1410		
22.07	1.9301	59.55	15.4310	110.55	31.8120		
21.99	2.0216	59.93	15.5950	112.79	32.4970		
22.31	2.1068	60.70	15.8490	115.06	33.2040		
22.64	2.1937	61.10	16.0270	117.39	33.8910		

References

[1] C. Ganguly, Development of plutonium-based advanced LMFBR fuels and thoria-based PHWR fuels in India, IAEA-TECDOC 352 (1985) 107-127.

[2] J.K. Fink, International Journal of Thermophysics, Vol. 3, No. 2 (1982) 165-200.

[3] R. Agarwal, R. Prasad, V. Venugopal, J. Nucl. Mater. 322 (2003) 98-110.

[4] S. Hubert, J. Purans, G. Heisbourg, P. Moisy, N. Dacheux, Inorg. Chem. 45 (2006) 3887-3894.

[5] S. Anthonysamy, J. Joseph, P.R. Vasudeva Rao, J. Alloy Compd. 299 (2000) 112-117.

[6] R. Kandan, R. Babu, P. Manikandan, R. Venkata Krishnan, K. Nagarajan, J. Nucl. Mater. 384 (2009) 231-235.

[7] K. Bakker, E.H.P. Cordfunke, R.J.M. Konings, R.P.C. Schram, J. Nucl. Mater. 250 (1997) 1-12.

[8] M.D. Freshley, H.M. Mattys, General Electric Report HW-76449, 1962.

[9] C. Cozzo, D. Staicu, J. Somers, A. Fernandez, R.J.M. Konings, J. Nucl. Mater. 416 (2011) 135-141.

[10] O.S. Vălu, O. Beneš, R.J.M. Konings, H. Hein, J. Chem. Thermodynamics 68 (2014) 122-127.

[11] H.E. Flotow, D.W. Osborne, S.M. Fried and J.G. Malm, J. Chem. Phys. 65, 3 (1976) 1124-1129.

[12] Th. A. Sandenaw, J. Nucl. Mater. 10 (1963) 165-172.

[13] P. Javorský, F. Wastin, E. Colineau, J. Rebizant, P. Boulet, G. Stewart, J. Nucl. Mater. 344 (2005) 50-55.

[14] R.J.M. Konings, J. Chem. Thermodynamics 36 (2004) 121-126.

[15] R.J.M. Konings, J. Nucl. Mater. 295 (2001) 57-63.

[16] R.J.M. Konings, A. Kovács, Handbook on the Physics and Chemistry of Rare Earths (K.A. Gschneidner Jr., J.C. Bünzli, V.K. Pecharsky (Eds.)), vol. 33 North-Holland, Amsterdam (2003), pp. 147–247 (Chapter 213).

[17] J. Leitner, P. Voňka, D. Sedmidubský, P. Svoboda, Thermochim. Acta 497 (2010) 7-13.

[18] N. Magnani, P. Santini, G. Amoretti, R. Caciuffo, P. Javorský, F. Wastin, J. Rebizant, G.H. Lander, Physica B 359-361 (2005) 1087-1089.

[19] B. Fultz, Progress in Materials Science 55 (2010) 247-352.

[20] A. Benisek and E. Dachs, Phys. Chem. Minerals (2011) 185-191.

[21] O.S. Vălu, O. Beneš, R.J.M. Konings, J.C. Griveau, E. Colineau, in progress.

[22] D.W. Osborne and E.F. Westrum, J. Chem. Phys. 21, 10 (1953) 1884-1887.

[23] H. Serizawa, Y. Arai, Y. Suzuki, J. Nucl. Mater. 280 (2000) 99-105.

[24] M.H. Rand, A.C. Fox and R.S. Street, Nature (London) 195 (1962) 567.

7

The effect of lattice disorder on the low-temperature heat capacity of $(U_{1-y}Th_y)O_2$ and ^{238}Pu-doped UO_2

The low-temperature heat capacity of $(U_{1-y}Th_y)O_2$ and ^{238}Pu-doped UO_2 samples were determined using hybrid adiabatic relaxation calorimetry. Results of the investigated systems revealed the presence of the magnetic transition specific for UO_2 in all three intermediate compositions of the uranium-thorium dioxide ($y = 0.05, 0.09$ and 0.12) and in the ^{238}Pu-doped UO_2 around 25 K. The magnetic behaviour of UO_2 exposed to the high alpha dose from the ^{238}Pu isotope was studied over time and it was found that 1.6 % ^{238}Pu affects the magnetic transition substantially, even after short period of time after annealing.

In both systems the antiferromagnetic transition changes intensity, shape and Néel temperature with increasing Th-content and radiation dose, respectively, related to the increasing disorder on the crystal lattice resulting from substitution and defect creation.

This chapter is reprinted with kind permission of Nature Research: *The effect of lattice disorder on the low-temperature heat capacity of* $(U_{1-y}Th_y)O_2$ *and* ^{238}*Pu-doped* UO_2*. O.S. Vălu, E. De Bona, K. Popa, J.-C. Griveau, E. Colineau, R.J.M. Konings. Scientific Reports 9, 15082 (2019).*

7.1. Introduction

The regular substitution of one or more atoms in the crystal lattice of solid solution phases can affect their thermodynamic properties significantly. Since a substitutional atom has different characteristics compared to the original one, substitution can lead to lattice adjustment and strain, lattice disorder, breaking of magnetic order, etc., which all can affect the phonon states and their dispersion in the material and thus the thermal capacity and the thermal transport. Effects on the thermal capacity are generally observed at low temperature, well below the limit of $3R$ per mole as established by Einstein and Debye, and can be studied with low-temperature calorimetric techniques.

All tetravalent actinide ions can be hosted in the AnO_2 dioxide close-packed fluorite structure and complete solid solution series exists between all end members. Low-temperature calorimetric measurements of $(Th_{1-y}Pu_y)O_2$ [1] showed that there is a substantial composition effect and the excess heat capacity was explained by the strain resulting from the substitution of isovalent ions of significantly different size on the cation sublattice, 96 pm for Pu^{4+} and 105 pm for Th^{4+}. Similar measurements on $(U_{1-y}Am_y)O_{2-x}$ with $y = 0.08$ and 0.20 yielded less obvious results [2]. Again a substantial excess heat capacity was observed at very low temperature but also the complete absence of the magnetic transition due to the antiferromagnetic ordering of the U^{4+} ions even at a minor extent of dilution. However, the $(U_{1-y}Am_y)O_{2-x}$ solid solution is complicated by the fact that a charge transfer takes place and that americium becomes trivalent, compensated by a equimolar amount of pentavalent uranium. This results in a more complex $(U^{4+},U^{5+},Am^{3+})O_2$ composition, and thus a higher "dilution" effect than formally. Moreover, americium is a highly radioactive material (half life 432.2 years) and radiation effects due to alpha decay of ^{241}Am create disorder that also may affect the phonon states and dynamics.

In order to obtain information on the separate effects of dilution-induced disorder and radiation-induced disorder on the heat capacity of actinide oxides and particularly on the magnetic transition in uranium-based fluorite dioxide systems we have performed studies on two highly different materials. Firstly, we measured the low-temperature heat capacity of $(U_{1-y}Th_y)O_2$ with $y = 0.05, 0.09$ and 0.12. In this material the non-magnetic Th^{4+} acts as diluent for the magnetic U^{4+} ions (no charge transfer), whereas the additional effect of distortion in the lattice due to the mismatch of the ionic radii (103 pm for U^{4+} and 108 pm for Th^{4+}) is expected to be relatively small. Both elements are only mildly radioactive, and their handling allows to obtain heat capacity data of the highest quality and accuracy with the instrument employed, and radiation-induced disorder is negligible. Secondly, we measured the low-temperature heat capacity of uranium dioxide doped with the highly radioactive ^{238}Pu isotope (half life 87.7 years) as a function of aging time to assess the effect of alpha decay and the concomitant lattice disorder in the fluorite structure.

7.2. Results and discussion

7.2.1. $(U_{1-y}Th_y)O_2$: effect of matrix dilution and lattice strain

The heat capacity of $(U_{1-y},Th_y)O_2$ solid solution with y = 0.05, 0.09 and 0.12 is shown in figure 7.1 together with the heat capacity of UO_2 [3] and ThO_2 [4, 5]. λ-type anomalies are observed around 27.2 K, 25.1 K and 21.8 K, respectively for the intermediate compositions Th5, Th9 and Th12 with a maximum C_P ($J{\cdot}K^{-1}{\cdot}mol^{-1}$) of 33.3, 23.3 and 20.5, respectively. This heat capacity anomaly is related to the long range antiferromagnetic ordering of the spins of the U^{4+} ions in UO_2 at low temperature, which was first observed by Jones *et al.* [6] and analysed in detail later by Huntzicker and Westrum [3]. The nature of the transition has been further analyzed by neutron diffraction [7, 8] and NMR studies [9]. These studies showed that at low temperature the oxygen cage of the UO_2 unit cell shows a Jahn-Teller distortion. The physics of the transition is very complex and is still subject of investigations. It is beyond the scope of this work and for details the readers are referred to the review by Lander and Caciuffo [10].

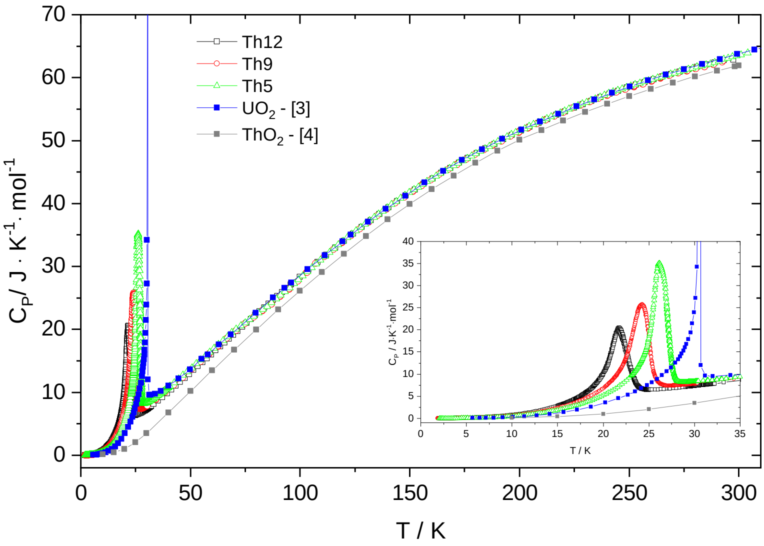

Figure 7.1: The low-temperature heat capacity of the Th5, Th9 and Th12 samples studied in this work.

This peak amplitude could be due to the fact that Huntziker and Westrum made a very detailed scan through the transition region (temperature step < 0.01 K) whereas we made a standard scan (> 0.1 K). On the other hand it is a known weak point of our technique that it cannot accurately fit the time dependent relaxation data in case of a large heat capacity dependence near T_N, as in the case of UO_2. This should be taken into account when discussing the entropy values.

The current results clearly show that with increasing thorium concentration in the solid solution the antiferromagnetic peak shifts towards lower temperature, its intensity is reduced and area broadens. This is consistent with earlier studies of the $(U,Th)O_2$

solid solution. Both Comly [11] and Hinatsu and Fujino [12] studied the magnetic transition by magnetic susceptibility measurements and found a linear dependence of T_N (see figure 7.2). White and Sheard [13] found that T_N derived from thermal expansion decreases linear up to 30 % ThO_2 and extrapolates to a similar value. However, the experimental data suggest that above 30 % ThO_2 the slope of dependence changes.

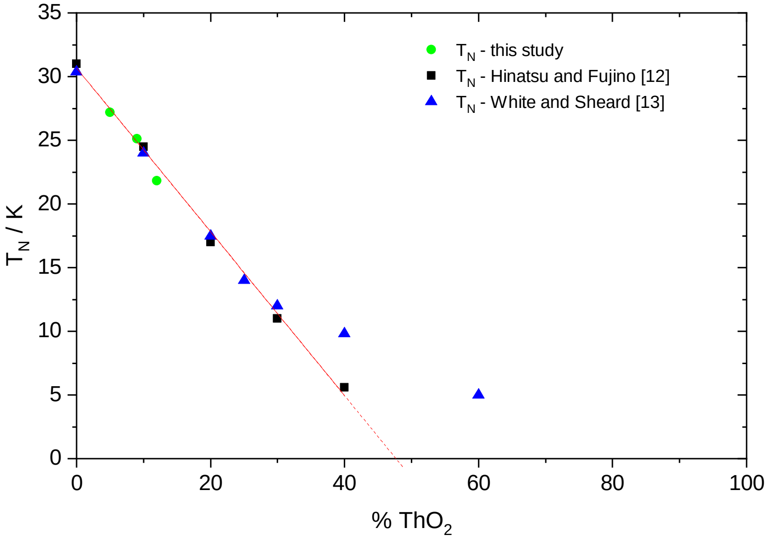

Figure 7.2: The Néel temperature of the (U,Th)O_2 solid solution as function of composition.

When plotting C_P/T over the squared temperature, as shown in figure 7.3, it can be observed that the heat capacity reaches zero at 0 K absolute temperature, which is the situation of a perfect crystal implied by the third law of thermodynamics. For all compositions the nearly linear curve is in good agreement with the Debye theory. However, the low-temperature values for the $(U_{1-y}Th_y)O_2$ solid solutions are well above those of the end members, UO_2 and ThO_2, revealing the significant excess heat capacity.

For a further analysis of the magnetic anomalies, the "ideal" heat capacity (Neumann-Kopp) of the mixed oxides was estimated by interpolation based on the low-temperature literature data of UO_2 [3] and ThO_2 [4] end-members, and by neglecting the magnetic transition for UO_2 using the lattice heat capacity suggested by Huntzicker and Westrum [3]. The experimental results of $(U_{1-y}Th_y)O_2$ solid solution are in a good agreement with the computed values from the Neumann-Kopp rule and no significant difference for the measured temperature interval is observed, except the low-temperature range below the characteristic antiferromagnetic transition. Further, we have calculated the difference between the two heat capacity curves (measured and computed) and will refer to it as the excess heat capacity (${C_P}^{exs}$), which is shown in figure 7.4 and defined as:

$$ {C_P}^{exs} = {C_P}^{m} - {C_P}^{NK} \tag{7.1} $$

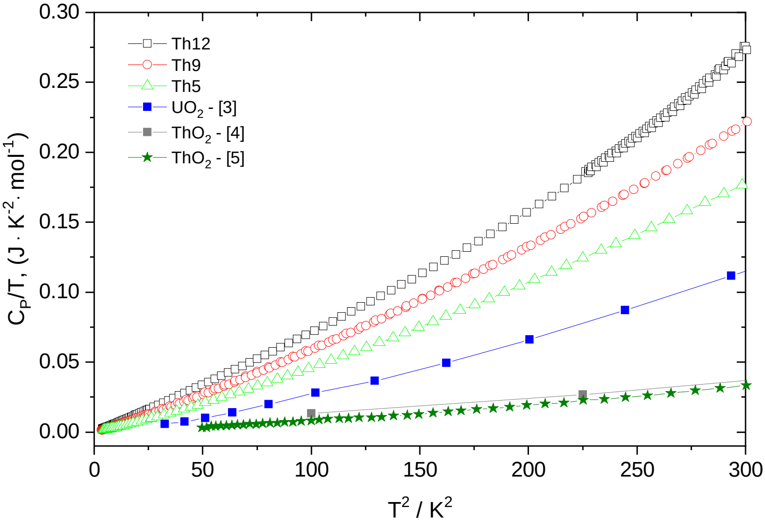

Figure 7.3: Low-temperature heat capacity of the Th5, Th9 and Th12 samples, together with the heat capacity data of UO_2 obtained by Huntzicker and Westrum [3], ThO_2 of Osborne *et al.* [4] and Magnani *et al.* [5].

where ${C_P}^m$ is the measured heat capacity and ${C_P}^{NK}$ is the computed heat capacity by Neumann-Kopp's rule disregarding the anomaly of the UO_2. This excess heat capacity primarily reflects the effect of magnetic fluctuation of the metal sublattice substitution on the phonon dynamics. Moreover, a weak Jahn-Teller distortion or CF transitions play a role in UO_2 up to temperatures well beyond 200 K [14], but it is not obvious whether this effect is influenced by dilution in the (U,Th)O_2 solid solution. Overall, the N-K approximation is providing a straightforward approach to assess this and thus the ${C_P}^{exs}$ will include all these effects.

Each individual peak has been been integrated using Origin Software (version 8.1) and the results are shown in table 7.1 and compared to similar analysis done for literature data of UO_2. The expected entropy of the triplet Γ_5 ground state of the $^3H_4$ multiplet of U^{4+} in pure UO_2 is $R\ln(3) = 9.1$ J·K^{-1}·mol^{-1}. Huntzicker and Westrum [3] reported 8.4 J·K^{-1}·mol^{-1} for the total anomaly and ~ 6.3 J·K^{-1}·mol^{-1} at the Néel temperature. The latter becomes 7.24 J·K^{-1}·mol^{-1} using the same analysis as for our measurements.

Table 7.1: Data of peak analysis of $(U_{1-y},Th_y)O_2$ solid solution with y = 0.05, 0.09 and 0.12 together with the one of UO_2 [3].

sample	T_{peak} (K)	S_{AF} (J·K^{-1}·mol^{-1})	Peak height (J·K^{-1}·mol^{-1})
UO_2	30.44	7.24	1635.9
Th5	27.2	4.64	33.3
Th9	25.1	4.26	23.3
Th12	21.8	3.74	20.5

The entropy values associated to the magnetic transition of $(U_{0.95}Th_{0.05})O_2$, $(U_{0.91}Th_{0.09})O_2$ and $(U_{0.88}Th_{0.12})O_2$ at the Néel temperature were found to be 4.64, 4.26

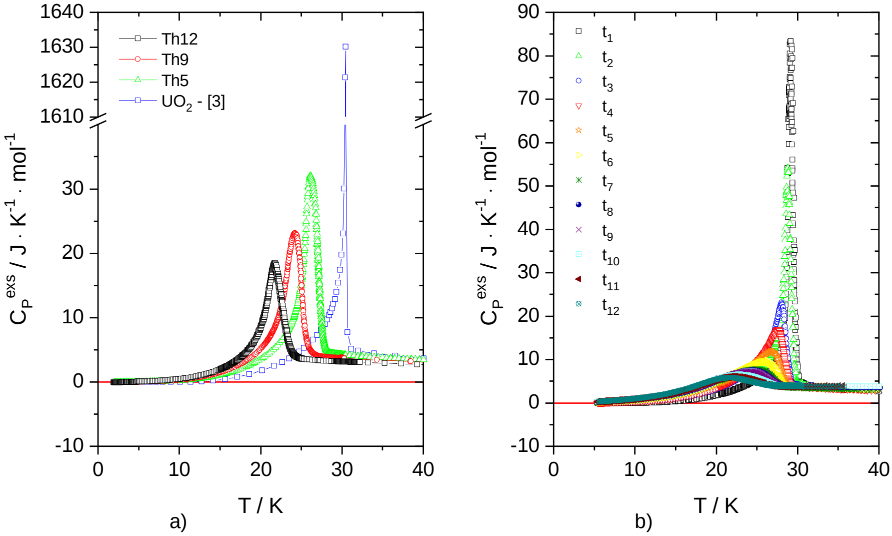

a) b)

Figure 7.4: The low-temperature magnetic transition observed in this work plotted as ${C_P}^{exs}$ for a) $(U_{1-y},Th_y)O_2$ solid solution (Th5, Th9, Th12 and literature data of UO_2 [3]) and b) $(U,^{238}Pu)O_2$ as a function of storage time.

and 3.74 J·K^{-1}·mol^{-1}, respectively (corresponding to 4.7, 4.7 and 4.3 J·K^{-1}·mol(U)$^{-1}$). These values should not be compared to the values for pure UO2 by Huntziker and Westrum because of the different calorimetric techniques. As stated earlier, Huntziker and Westrum made a very detailed scan through the transition region (temperature step < 0.01 K) resulting in a very sharp peakw, which our measurement technique does not capture fully. It is also a known weak point of the PPMS technique that it cannot accurately fit the time dependent relaxation data in case of a large heat capacity dependence near TN [15], as in the case of UO_2.

Linear extrapolation of the values for the entropy of transition derived from our measurements indicates that the anomaly disappears at about 44 % of thorium in the mixed solid solution, which means when five of the twelve second-nearest U neighbours in the UO_2 fluorite lattice are substituted by Th, breaking the long-range magnetic order of U^{4+}. This is close to the value 42 % found by Comly [11] and about 45 % Th by Hinatsu and Fujino [12] by magnetic susceptibility measurements.

7.2.2. $(U,^{238}Pu)O_2$: effect of radiation damage

The results of the series low-temperature heat capacity measurements of the $(U,^{238}Pu)O_2$ sample in the temperature interval from 5 to 50 K for different storage times after annealing of the sample are presented in figure 7.5, together with the low-temperature heat capacity data of the end-members. It is evident that the λ transition rapidly changes shape and position with the aging time, c.q. accumulated dose.

The excess heat capacity peak of the measured sample has been derived as a function of the accumulated α dose up to 277 days. Using again the Origin Software (version 8.1), the peak evaluation has been performed and the related thermodynamic data are given in table 7.2. Applying the estimated heat capacity of UO_2 based on the same corrections made by Huntzicker and Westrum [3] the excess entropies at the Néel temperature of the magnetic transition are found to decrease with time (table 7.2). Integrating over the full temperature range to T= 50 K, we found an excess entropy of about 6 J·K^{-1}·mol^{-1} for all measurements as shown in figure 7.6, which means that even if the anomaly vanishes the corresponding entropy per mole is largely distributed over much wider temperature interval. The inset graph from figure 7.5 shows that when C_P/T is plotted over the squared temperature, the heat capacity data does not become zero at 0 K, which indicates the presence of lattice disorder and residual entropy typical for a non-equilibrium state.

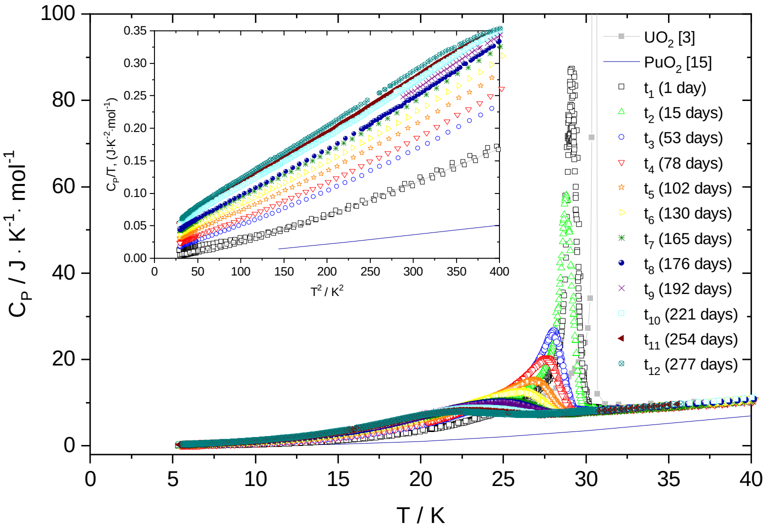

Figure 7.5: The low-temperature heat capacity of the $(U,^{238}Pu)O_2$ sample studied in this work together with PuO_2 obtained by Flotow *et al.* [16] and UO_2 previously measured in house.

As shown in figure 7.7a the peak height of the magnetic transition decreases significantly with a accumulated dose (time) and the area broadens, similar to the composition dependence observed for the $(U_{1-y}Th_y)O_2$ solid solution. Moreover, the maximum of the peak (shown as Néel temperature in figure 7.7b) is shifting towards lower temperatures and the corresponding entropy at the Néel temperature decreases linearly as well (figure 7.7c). Note that we do not have a value for t_0 because the heat capacity of damage-free $(U,Pu)O_2$ with about 2 % Pu_{total}, used in this work, has not been measured. Pure UO_2 cannot serve as reference, as our results for $(U_{1-y},Th_y)O_2$ show that the heat capacity is already affected at low concentrations.

Our results show that the antiferromagnetic ordering of the spins of the U^{4+} ions in uranium dioxide is dramatically affected by the continuous self-irradiation from the high α activity of ^{238}Pu, which leads to atomic displacements in the lattice and the subsequent formation of point defects and extended defects. Each α-decay produces about

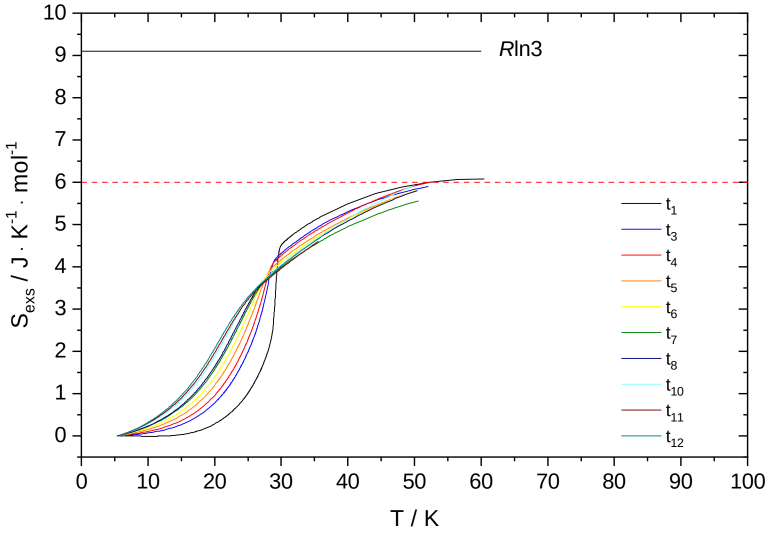

Figure 7.6: Excess entropy of ^{238}Pu-doped UO_2 sample. Different coloured curves of S_{exs} indicate the specific time (and accumulated radiation damage) at which the measurements took place. Some of the curves are not shown because their measurements have not been extended to the considered temperature interval.

1500-2000 displacements, which accumulate over time in substantial lattice disorder. In about 24 hours after annealing the intensity of the heat capacity peak specific to UO_2 has diminished to about 5 % from its original intensity, and further flattening of the peak occurs with increasing alpha-decays per mole of material. Since the change in the entropy is minimal, it must be concluded that the antiferromagnetic transition gradually changes into a Schottky-type anomaly with a significant part of the residual entropy redistributed over the entire temperature interval. This can be understood from the changes in the phonon dynamics and anharmonicity due to radiation induced disorder created by the strong ^{238}Pu alpha emitter and magnetoelastic interaction between the magnetic moments in the uranium atoms and lattice distortions.

7.3. Conclusions

The heat capacity of a fluorite-structured mixed dioxide is strongly driven by the interaction of the phonons with the metal atoms of the end-members of the solid solution. Taking into account that both uranium and thorium have long half lives, lattice disorder (displacements and vacancies) resulting from α self-irradiation in $(U_{1-y}Th_y)O_2$ is limited in this system, and the principal disorder mechanism is substitution on the metal sublattice. Our analysis of the antiferromagnetic transition in $(U_{1-y}Th_y)O_2$ shows that the substitution of five of the twelve uranium atoms in the unit cell by thorium suppresses the long-range magnetic ordering in the solid solution. The cation size difference between U^{4+} (100 pm) and Th^{4+} (105 pm) is smaller than between Pu^{4+} (96 pm) and Th^{4+}, but the excess heat capacity at low temperature (< 20 K) is substantially larger

Table 7.2: Peak analysis data of (U,^{238}Pu)O$_2$ solid solution obtained on different stages of radiation damage accumulation.

Notation	Center (K)	S_{AF} ($J \cdot K^{-1} \cdot mol^{-1}$)	Peak height ($J \cdot K^{-1} \cdot mol^{-1}$)
1 day	29.3	4.58	87.3
15 days	28.8	-[a]	58.0
53 days	28.1	4.25	26.7
78 days	27.6	4.19	20.5
102 days	26.9	4.04	15.2
130 days	26.1	3.92	12.5
165 days	25.2	3.80	10.5
176 days	24.9	3.77	10.2
192 days	24.9	3.65	9.9
221 days	23.4	3.61	8.8
254 days	22.7	3.38	8.2
277 days	22.3	3.28	7.9

[a] *The excess entropy at t_2, corresponding for the measurement after 15 days, could not be calculated due to the minimal temperature interval of the considered measurement;*

than for a similar extent of substitution in ($Th_{1-y}Pu_y$)O_2 samples measured previously [1], as shown in figure 7.8 the plot of C_P/T vs T^2. We attribute this to the broadening of the λ-transition and its shift and extension to lower temperatures with increasing extent of substitution; the excess heat capacity due to lattice strain being masked in the tail of the transition, which changes from a sharp λ-type peak to a more broad and diffuse transition. This phenomenon is known from other antiferromagnetic materials such as $Zn_2VO(PO_4)_2$ doped with Ti^{4+} [17], doped $LaSr_2Mn_2O_7$ [18], or Mg(Al,Cr)$_2$O$_4$ [19].

The heat capacity of both ($U_{1-y}Th_y$)O_2 and ($Th_{1-y}Pu_y$)O_2 extrapolate to zero at 0 K, indicating perfect crystal properties and no effect of substitution on the metal sublattice. In contrast the heat capacity of (U,^{238}Pu)O$_2$ sample shows a significant residual heat capacity at 0 K which can be attributed to disorder caused by self-radiation, since the residual value clearly increases with time/dose. We conclude that the principal causes for this are the creation of uranium Frenkel pairs and oxygen Frenkel pairs in the crystal lattice, and extended defects at high doses. With increasing dose (c.q. concentration of defects) the antiferromagnetic transition in this sample transforms from a sharp peak to a broad anomaly. According to X-ray diffraction measurements, the lattice expansion due to accumulated dose (time) reaches saturation (E. De Bona, personal communication) in this sample after about 300 days and results in a disordered quasi-equilibrium state in which defect creation and recombination balance each other. Staicu *et al.* [20] concluded from thermal annealing experiments of ^{238}Pu-doped UO_2 that both oxygen and uranium interstitials are present in the material. Moreover, defects that escape from the recombination can concentrate into loops and voids [21]. Molecular dynamics simulations of alpha decay in UO_2 by Van Brutzel and Rarivomanantsoa [22] showed that the number of oxygen Frenkel pairs is twice as high as the uranium Frenkel pairs, and that the number of displaced atoms in stable point defects at the end of the cascade is 13 % for uranium and about 2 % for oxygen. Thus it can be concluded that the

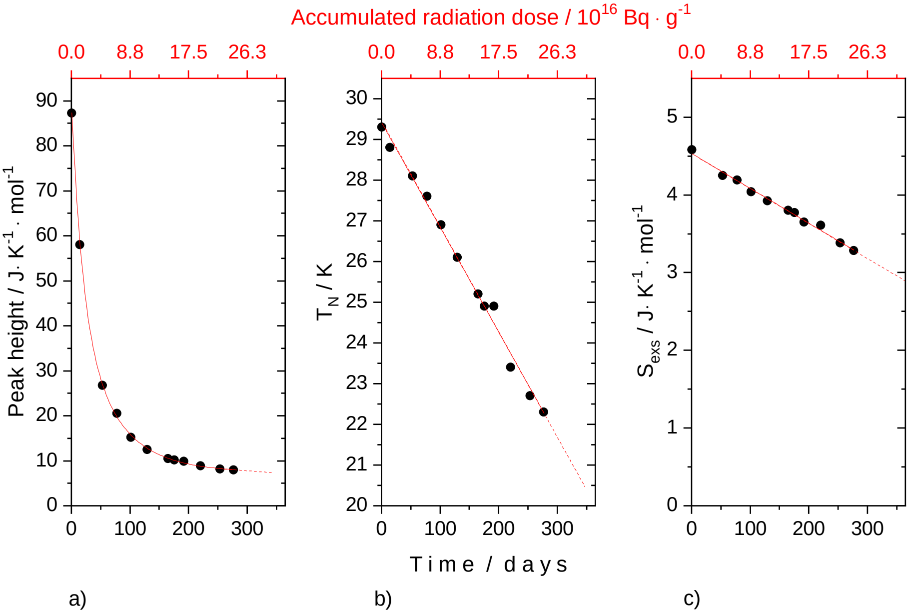

Figure 7.7: Thermodynamic characteristics of the low-temperature heat capacity antiferromagnetic anomaly of the $(U,^{238}Pu)O_2$ sample studied in this work. a) The height of the anomaly at the maximum; b) the Néel temperature and c) the entropy of transition at the Néel temperature.

disordered quasi-equilibrium state has not yet been achieved in our experiments after 277 days and further change in the transition thermodynamics can be expected.

It is interesting to hypothesise how the radiation affects the electronic states of U^{4+} in the damaged material. The crystal field splitting of the U^{4+} ground state multiplet in paramagnetic UO_2 results in a Γ_5 triplet ground state, with a Γ_3 doublet as first excited state at 150 meV (Magnani *et al.*[23]). Considering that both Uranium Frenkel Pairs (UFP) and Oxygen Frenkel Pairs (OFP) are formed in the damaged crystal lattice, the Néel transition in the $(U,^{238}Pu)O_2$ sample will no longer correspond to a disorder-order transformation, but to a transition between two disordered states with reduced long-range magnetic ordering. The strong lattice disorder in the material with formation of UFPs and OFPs will lead to changes in the dynamics between the U^{4+} and the surrounding O neighbours and likely results in a splitting of the Γ_5 ground state leading to two low-lying electronic states in the disordered material. As result the sharp transition changes to a Schottky-like anomaly.

In figure 7.9 we aligned the results for the magnetic transition in both systems at the peak center by using T - T_N as temperature axis (the reason for negative values). Although, the overall change in peak shape of the two investigated systems is comparable, the strong asymmetry of the ^{238}Pu-doped system evidences that disorder on the metal and oxygen sublattice may lead to similar magnetoelastic effects.

In conclusion we can state that the antiferromagnetic heat capacity anomaly in UO_2 is highly sensitive to disorder in the crystal lattice, as discussed by Huntzicker and

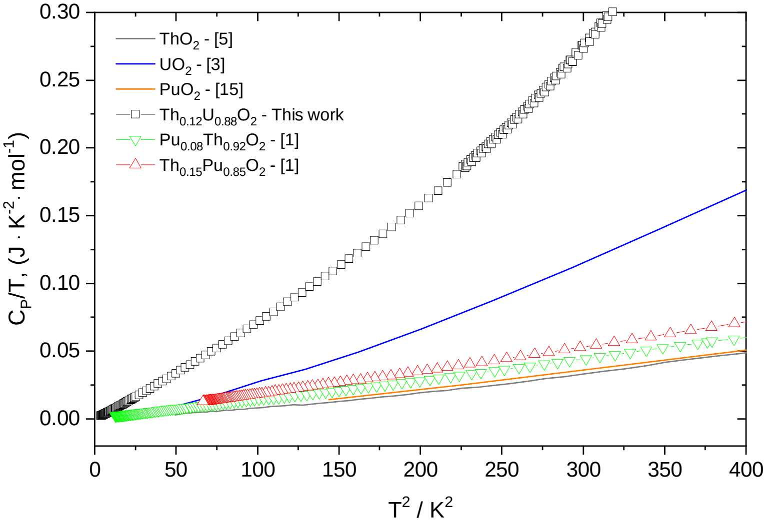

Figure 7.8: The low-temperature heat capacity of the $Th_{0.12}Pu_{0.88}O_2$ (Th12) sample studied in this work, together with the end-members UO_2, ThO_2 and PuO_2 and $Th_{1-y}Pu_yO_2$ (y= 0.08 and 0.85) plotted as Cp/T vs T^2.

Westrum [3] in their seminal paper. They explained the difference between their results and those by Jones *et al.* [6], that revealed a much less pronounced anomaly at a lower temperature, by the presence of oxygen interstitials as a result of a hyperstoichiometric composition of the $UO_{2.01}$ sample. We, here, have shown that lattice disorder caused by metal ion dilution and radiation damage has a similar effect on the transition characteristics, with a measurable impact at already low concentrations and moderate doses.

7.4. Material and methods

7.4.1. Sample preparation and characterisation

(U,Th)O_2 samples with three Th concentrations (5, 9 and 12 mol%) were prepared using a hydrothermal method [24, 25]. The synthesis was conducted under argon and in the presence of minute amounts of hydrazine in order to limit the oxidation of the U^{4+}. As starting materials we have used solutions of Th^{4+} (1.9 M in 8 M HNO_3) and U^{4+} (0.47 M, obtained by electroreduction of $UO_2(NO_2)_2$ solution in 4 M HNO_3 containing 0.5 M of hydrazine). The other reagents (NH_4OH 25 %, hydrazine hydrate) were of analytical grade and used as supplied by Merck.

The hydroxides were firstly produced by direct coprecipitation of the An^{4+} solutions in nitric acid with ammonium hydroxide (10-20 % excess). The obtained coprecipitates were washed several times with distilled water in order to remove any trace of nitrate, which may induces the oxidation of U^{4+} to soluble U^{6+} under the working temperature conditions. The decomposition was conducted under hot compressed water for 5 h at 250 °C in teflon autoclaves. The resulting nanocrystals (circa 3.5 nm) were

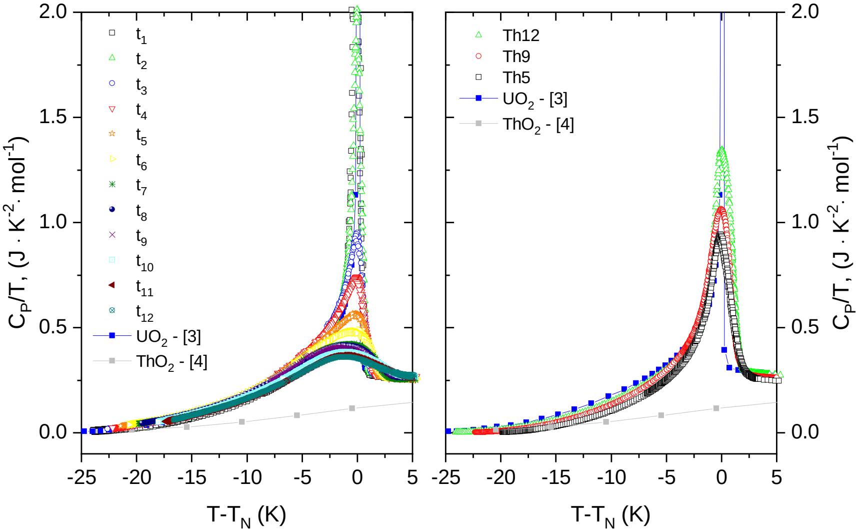

Figure 7.9: The low-temperature magnetic transition aligned at peak center as Cp/T vs T-T_N for a) (U,^{238}Pu)O_2 as a function of time and b) $(U_{1-y},Th_y)O_2$ solid solution (Th5, Th9, Th12 and literature data of UO_2 [3]).

washed with water, ethanol and acetone, in order to gradually decrease the polarity of the solution. Pellets of 3.5 mm diameter and several mm in height were produced by pressing and heated for 5 h at 1000 °C (1st step) and 24 h at 1650 °C (2nd step) under Ar-H_2(4 %).

The real U and Th concentration in the samples was measured by Inductively Coupled Plasma Mass Spectrometry (ICP-MS) using a A ThermoFinnigan Element instrument with auto-sampler, according to an appropriate standardisation method. The results are summarized in table 7.3.

The UO_2-$^{238}PuO_2$ sample was obtained by pressing and sintering of a powder produced via liquid route, guaranteeing a homogeneous and intimate mixing. The metal content of the $^{238}PuO_2$ was 87 wt.% Pu, 73 wt.% being ^{238}Pu, the remaining 13 % being the decay product uranium 234. The composition was chosen considering the activity of the dopant powder and tuning the dopant concentration to fit the aging of the sample to a reasonable period of time. The Pu dopant powder was dissolved as received using HNO_3 and dropwise addition of HF, and then added to the corresponding amount of uranyl solution. Precipitation was achieved by adding ammonia to the solution, and the resulting precipitate was washed with distilled water several times and then filtered on paper filters. The paper filters were burnt away during a pre-calcination step (6 h at 400 °C) under air and then the powder was calcined at 700 °C for first 2 h in air (N_2 + 20 % O_2) to remove any remaining paper and finally for 2 h under Ar-H_2 (4 %). This powder was then pressed in 5 mm disks of roughly 80 mg each with a force of 14.5 kN (738 MPa) and sintered for 6 h under Ar-H_2 at 1650 °C. Based on elemental and isotopic composition analysis done in March 2016 by ICPMS the actual composition of the investigated sample is $(^{234}U_{0.0037}{}^{235}U_{0.0070}{}^{238}U_{0.9680}{}^{238}Pu_{0.0156}{}^{239}Pu_{0.0047}{}^{240}Pu_{0.0008})O_2$ and represents 99.98

%. The diference of 0.02 % is given by the sum of the isotopes ^{241}Am, ^{233}U and ^{236}U. From chemical point of view the sample contains just uranium and plutonium being virtually free of americium and other impurities. We will refer to this composition as (U,^{238}Pu)O_2. Table 7.3 lists the fabrication data.

Table 7.3: Notation, composition and fabrication data of the studied samples.

Notation	Composition^a Th/(U+Th)(mol%)	Heat treatment Ar/H_2	Sintering Ar/H_2	cell parameter (Å)
Th5	4.78 ± 0.02	1000 °C, 5 h	1650 °C, 24 h	5.4745(1)
Th9	8.76 ± 0.04	1000 °C, 5 h	1650 °C, 24 h	5.4800(1)
Th12	12.30 ± 0.05	1000 °C, 5 h	1650 °C, 24 h	5.4853(2)
Notation	Composition^a ^{238}Pu (wt.%)	Calcination (Ar/H_2)	Sintering (Ar/H_2)	cell parameter (Å)
(U,^{238}Pu)O_2	1.6	700 °C, 2h	1650 °C, 6h	5.4688

^{a} *Composition measured ICPMS, k=2;*

7.4.2. X-ray analysis

During and after the production, samples were characterized by XRD using a Bruker D8 (Bruker AXS GmbH, Karlsruhe, Germany) diffractometer mounted in a Bragg–Brentano configuration with a curved Ge (1,1,1) monochromator and a ceramic copper tube (40 kV, 40 mA) and supplied with a LinxEye position sensitive detector. The cell parameters of the investigated compositions derived from a Rietveld analysis, are listed in table 7.3. The resulting values for the (U,Th)O_2 samples agree excellently with the cell parameters derived from Vegard's law. Also the value for the (U,^{238}Pu)O_2 sample corresponds well to the lattice parameter derived Vegard's law considering the actual composition. This confirms that all our samples are homogeneous solid solutions of stoichiometric composition. Homogeneity of the mixtures is evident also in the SEM images (figure 7.10) that have been taken after production.

7.4.3. Calorimetry

The heat capacity of $(U_{1-y}Th_y)O_2$ with y = 0.05, 0.09 and 0.12 was measured using a low-temperature vacuum calorimeter based on a hybrid adiabatic relaxation method (PPMS, Quantum Design Inc.) as described in our previous paper [2]. The measurements of the Th5, Th9 and Th12 samples were carried out using small solid pieces with the masses of 47.4 mg, 37.1 mg and 57.1 mg, respectively, in the temperature intervals of 2.05 to 304.10 K, 1.86 to 292.93 K and from 1.94 to 297.50 K. Different from our measurements of other actinide oxide solid solutions [1, 2], these samples have been measured without protective encapsulation into Stycast (for radioprotection purposes) which results in a high accuracy of the PPMS apparatus with estimated uncertainties for the heat capacities of about 1 to 2 % as reported by Lashley *et al.* [15].

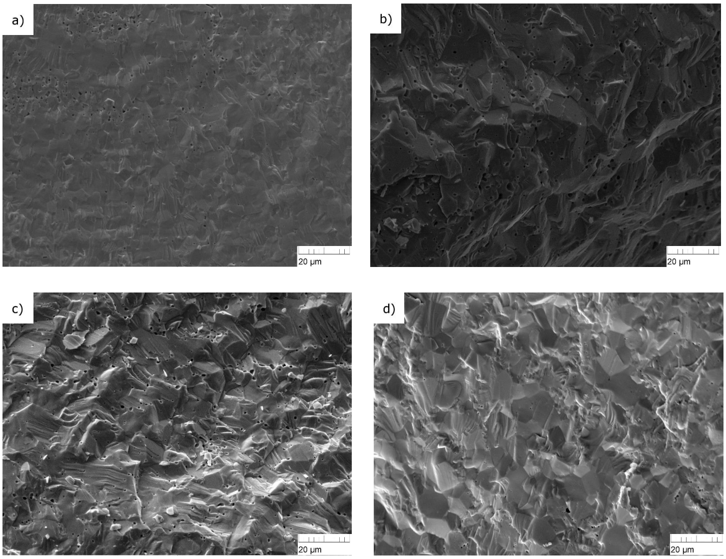

Figure 7.10: Scanning electron microscopic (SEM) images of the $(U_{1-y}Th_y)O_2$ samples: a) Th5, b) Th9 and c) Th12 and $(U,^{238}Pu)O_2$ sample in d).

In the case of $(U,^{238}Pu)O_2$ sample, the same instrument has been used for measuring the heat capacity as a function of aging time. Since the main objective of this study was to study the behavior of the magnetic peak, we have focused our investigation in the interested temperature region and measurements have been performed in the temperature interval from about 5 K to 50 K. The sample consisted of one small solid piece with mass of 1.4 mg and for radiation protection reason it was wrapped in Stycast [26] which increased the uncertainty to about 4 to 5 % after the corresponding heat capacity was subtracted. Before the first measurement, the sample was annealed for 4 hours into Ar/H_2 atmosphere (1L/min.) at 1650 °C to eliminate the self-radiation damage in the lattice accumulated during the storage at room temperature in the period between fabrication and measurement. After annealing and Stycast encapsulation the first measurements have been carried out after about 24 hours and we consider this moment as being the reference time point (t_1) with minimum radiation damage. The subsequent measurements have been performed after different time intervals, 15 days (t_2), 53 days (t_3), 78 days (t_4), 102 days (t_5), 130 days (t_6), 165 days (t_7), 176 days (t_8), 192 days (t_9), 221 days (t_{10}), 254 days (t_{11}) and 277 days (t_{12}) for better understanding the influence of the cumulative radiation dose on the thermal properties of the mixed oxide. In between the measurements the sample was stored at room temperature.

References

[1] O.S. Vălu, O. Beneš, R.J.M. Konings, J.-C. Griveau, E. Colineau, J. Phys. Chem. Solids 86 (2015) 194-206.

[2] O.S. Vălu, O. Beneš, E. Colineau, J.-C. Griveau, R.J.M. Konings, J. Nucl. Mater. 507 (2018) 126-134.

[3] J. Huntzicker, E. Westrum, J. Chem. Thermodyn. 3 (1971) 61–67.

[4] D.W. Osborne, E.F. Westrum, J. Chem. Phys. 21 (1953) 1884-1887.

[5] N. Magnani, P. Santini, G. Amoretti, R. Caciuffo, P. Javorský, F. Wastin, J. Rebizant, G.H. Lander, Phys. B 359–361 (2005) 1087-1089.

[6] W.M. Jones, J. Gordon, E.A. Long, J. Chem. Phys. 20 (1952) 695.

[7] B.C. Frazer, G. Shirane, D.C. Cox, C.E. Olsen, J. Appl. Phys. 37 (1965) 1386.

[8] B.T. Willis, R.I. Taylor, Phys. Lett. 17 (1965) 188–190.

[9] K. Ikushima, S. Tsutsui, Y. Haga, R.E. Yasuoka, H.and Walstedt, Phys. Rev. B 63 (2001) 104404.

[10] G.H. Lander, R. Caciuffo, J. Phys.: Condens. Matter 00, DOI: http://iopscience.iop.org/10.1088/1361-648X/ab1dc5 (2019).

[11] J.B. Comly, J. Appl. Phys. 39 (1968) 716.

[12] Y. Hinatsu, T. Fujino, J. Solid State Chem. 60 (1985) 195–202.

[13] G.K. White, F.W.J Sheard, J. Low. Temp. Phys. 14 (1974) 445.

[14] R. Caciuffo, G. Amoretti, P. Santini, G.H. Lander, J. Kulda, P. de V. Du Plessis, Phys. Rev. B 59 (1999) 13892.

[15] J.C. Lashley, M.F. Hundley, A. Migliori, J.L. Sarrao, P.G. Pagliuso, T.W. Darling, M. Jaime, J.C. Cooley, W.L. Hults, L. Morales, D.J. Thoma, J.L. Smith, J. Boerio-Goates, B.F. Woodfield, G.R. Stewart, R.A. Fisher, N.E. Phillips, Cryogenics 43 (6) (2003), pp. 369-378.

[16] H.E. Flotow, D.W. Osborne, S.M. Fried, J.G. Malm, J.Chem.Phys.65(3)(1976) 1124–1129.

[17] A. Yogi, N. Ahmed and R. Nath, Phys. Rev. B 91, 024413 (2015) 1-12.

[18] S. Nair and A. Banerjee, Phys. Rev. B 70, 104428 (2004) 1-6.

[19] S. Klemme and M. Ahrens, Phys. Chem. Minerals 34 (2007) 59-72.

[20] D. Staicu, T. Wiss, V.V. Rondinella, J.P. Hiernaut, R.J.M. Konings, C. Ronchi, J. Nucl. Mater. 297 (2010) 8-18.

[21] T. Wiss, O. Dieste-Blanco, A. Tacu, A. Janssen, Z. Talip, J.-Y. Colle, P. Martin, R.J.M. Konings, J. Mater. Res. 30 (2015) 1544-1554.

[22] L. Van Brutzel, M. Rarivomanantsoa, J. Nucl. Mater. 358 (2006) 209-216.

[23] N. Magnani, P. Santini, G. Amoretti, R. Caciuffo, Phys. Rev. B 71 (2005) 054405.

[24] L. Balice, D. Bouëxière, M. Cologna, A. Cambriani, J.-F. Vigier, E. De Bona, G. D. Sorarù, C. Kübel, O. Walter, K. Popa, J. Nucl. Mater. 498 (2018) 307-313.

[25] K. Popa, O. Walter, O. D. Blanco, A. Guiot, D. Bouëxière, J.-Y. Colle, L. Martel, M. Naji, D. Manara, Cryst. Eng. Comm. 20 (2018) 4614-4622.

[26] P. Javorský, F. Wastin, E. Colineau, J. Rebizant, P. Boulet, G. Stewart, J. Nucl. Mater. 344 (2005) 50-55.

8

Conclusions and Outlook

I would rather have questions that can't be answered
than answers that can't be questioned.

Richard P. Feynman

Uranium, plutonium and americium are present in the nuclear fuel cycle in a large diversity of forms and isotopic compositions; Thorium offers advantages of an alternative fuel cycle. The understanding of the fuel behaviour requires scientific research for a better understanding of chemical and physical evolution of these radioactive materials from the fuel fabrication stage into the fission process to separation for recycling up to the waste disposal.

Investigating the thermodynamic properties of the actinide oxide and their solid solutions is very important for calculating and predicting the thermal behaviour of oxide-type nuclear materials under reactor conditions and in beyond-design-base accidents. For this reason, the measurements carried out in this thesis were achieved by the motivation of bringing my contribution in this wide and complicated area of nuclear research.

From the experimental point of view, heat capacity of solids can be a relatively easy property to measure from nearly 0 K up to about 2000 K, using calorimetric techniques, and the dioxides of thorium, uranium and plutonium have been studied extensively. Yet, when a binary oxide mixture is considered, such thermodynamic data are not available for a large number of them. One of the simplest approaches for the estimation of heat capacity of mixtures is the Neumann-Kopp rule. This rule assumes simple additivity of the end-members, implying that the phonon kinetics are hardly affected by substitution. At low temperature the lattice dynamics may of the end-members may be very different. Above room temperature where the contribution of harmonic lattice vibrations approaches the 3NR limit, the NK rule is a reasonable assumption. At high temperature the dynamics in fluorite dioxide crystals can lead to formation of thermal defects, such as oxygen Frenkel pairs (OFP) in which an oxygen atom is displaced into vacant position. This affects the lattice vibrations substantially. When it comes to nuclear materials, also the interaction of high energy radiation in the structure creates defects, resulting in significant changes in their thermal properties. It is thus questionable whether the Neumann-Kopp additivity rule can be applied.

Trying to establish an order of presenting the main findings of the performed investigations for the mixed oxides of the actinides, $(Th,Pu)O_2$, $(U,Pu)O_2$, $(Th,U)O_2$, $(U,Am)O_2$, we have to distinguish between three temperature ranges: very low-temperature (< 50 K), low-temperature (50 K - 300 K), high-temperature (300 K - 1800 K).

In conclusion one can generalize the observation from two perspectives the temperature range (low and high) and material composition.

8.1. Temperature range

- **Low-temperature region**

At low temperatures the heat capacity variation is attributed mainly to the vibrations in the crystal lattice and is described by the Debye-Einstein model. Below the limit established by this model (3R per mole) some phase changes can occur, as in the case of UO_2, visible as a large anomaly in the heat capacity curve at a specific temperature known as antiferomagnetic transition. Nevertheless, the heat capacity variation with temperature of the actinide oxides can be affected by various crystal defects (vacancies, interstitials, Schottky defects, Frenkel pair formation) as well as displacements and substitutions resulting from the α induced radiation damage of such materials. In some cases, these contributions can be negligible but, in general, they have to be experimentally investigated and their impact assessed, as in this thesis.

In this context, four binary systems were considered of which two of them meant to observe the high alpha decay influence over the systems and the other two were composition related aspects.

The very low-temperature and low-temperature heat capacity data have been obtained. The specific heat is determined by measuring relatively small samples with a mass of few miligrams (2.3 - 27.4 mg). The accuracy of the apparatus installed at JRC Karlsruhe was verified e.g. with 7 and 40 mg gold samples (NBS/NIST purity), and the results were in agreement with the literature. Low-temperature specific heat measurements of actinide compounds are more complex due to the safety aspects when handling such radioactive materials and the self-heating generated by the decay of these isotopes. Due to the selfheating effect, the lowest measurable temperature can be up to several Kelvin higher than the instrumental limits depending on the isotopic composition of the sample and the mass. Regarding the other aspect, of handling radioactive materials, the samples had to be enclosed in a Stycast (2850 FT) low-temperature conductive epoxy and then the heat capacity of the measured amount of Stycast is subtracted.

The main findings of the above described research can be summarised as follows: up to about 50 K an excess contribution is present in the heat capacity. In the case of $(U,Am)O_2$ and $(U,{}^{238}Pu)O_2$ the thermal substitution and the radiation damage compete resulting in a higher deviation from ideal behaviour than for the

(Th,Pu)O_2 system, where the anomaly is mainly associated to cation substitution, or the (U,Th)O_2 system for which the effect of matrix dilution is responsible for the excess. We conclude that in this temperature range the cation substitution and matrix dilution are obscured by the self-irradiation effect, when present. Above 50 K the results show an excess heat capacity that is assigned to the Schottky contribution correlated with mass difference and lattice strain.

- **High-temperature region**

Heat capacity data have been obtained for several mixed actinide dioxides based on enthalpy increments results obtained by a Setaram Multi Detector High Temperature Calorimeter (MDHTC - 96 type) operated in drop mode. The self-heating effect of the samples was negligible for this type of measurements, but the handling of highly radioactive materials had to be done in a safe mode for the analyst and for this reason the calorimeter was adapted for glove-box use. Samples weight ranged from about 20 mg to 180 mg depending on material.

When compared with the end-members we conclude that our results show no excess contribution for the measured enthalpy and derived heat capacity but obey the molar additivity rule, with respect to the experimental uncertainty.

For the thermal conductivity and thermal diffusivity investigations only one system was considered, (U,Am)O_{2-x}. For the two available intermediate compositions thermal diffusivity was measured from 500 to 1550 K using the laser flash technique and thermal conductivity was calculated. The samples were heated to the measurement temperature under a static atmosphere of nitrogen that initially contained 0.1% of oxygen and thermogram were recorded for each temperature interval.

Overall, four different binary oxide systems have been investigated in the high-temperature domain and their thermal behaviour was evaluated. In order to validate our results we had to work with limited existing literature data and incorporate results from modelling in some cases. **Based on this, the obtained thermal conductivity decreases with further addition of americium into the system and found to have a stronger impact than the comparable addition of plutonium due to the higher radiotoxicity of americium. This is in agreement with the theoretical studies for (U,Pu)O_2 of Nichenko and Staicu** [1]**.**

8.2. Material composition

- **(Th,Pu)O_2 system**

For this system both low-and high-temperature heat capacity were obtained for the first time and thermal behaviour was related to the Neuman-Kopp's additivity rule. Having the case of a multicomponent oxide in which the ionic radius of the two tetravalent actinides creates the largest difference in size on the cation sublattice no excess contribution was observed for the heat capacity extrapolating towards 0 at 0 K and behaving ideally when going in the high-temperature domain. Apparently, the radioactive decay plays no role in this case and the fluorite-type structure acts impassive on different mixture steps of the two components. **This system behaves ideally except the very low temperature where influences of the ionic radius become evident.** The presented data have been already cited in few publications [2–6] where authors have used it for comparison and validation of similar studies. Their work confirm the present results.

- **$(Th,U)O_2$ and $(U,Pu)O_2$ systems**

A review of the available heat capacity data was done for the two solid solutions and additional new experimental enthalpies were used for a better understanding of the heat capacity behaviour over a wide temperature range (300 - 3000 K). Using very small quantities of material, a lot of effort has been done in measuring each sample especially due to the samples sensitivity on oxygen stoichiometry. The importance of such experiments rely also in the comparison with the molecular dynamics calculations of some actinide oxides. As expected, our results for the $(Th,U)O_2$ and $(U,Pu)O_2$ solid solutions are in fair agreement with the additivity rule for the measured temperature interval. **Additionally, a model to analyse the defect contribution to the high-temperature heat capacity has been applied and we conclude that the energetics of formation and/or annihilation of OFP's in these compounds change with the concentration of the oxygen vacancies in the structure.**

- **$(U,Am)O_{2-x}$ and $(U,^{238}Pu)O_2$ systems**

High-temperature heat capacity values have been derived from the measured enthalpy increments over the considered temperature intervals indicating no presence of excess heat capacity, as described in chapter 4 of this thesis. Equivalent thermodynamic data have been experimentally obtained for the low-temperature region (chapter 5) where non typical behavior was observed. The magnetic disorder associated to uranium dioxide is totally altered by the strong α activity specific to ^{241}Am and the corresponding entropy per mole is largely distributed over the temperature interval. **The present results for 10% and 20% americium in $(U,Am)O_{2-x}$ system lead to the conclusion that is is impossible to derive reliable data for the AmO_2 end-member with current available techniques.**

- **Matrix dilution and lattice strain effect versus radiation damage in the uranium containing solid solutions**

Similar to the other actinide systems, low-temperature heat capacity was measured for uranium-thorium dioxide (low thorium concentrations) and uranium dioxide doped with plutonium isotope 238. Results have shown that the characteristic magnetic transition of UO_2, visible in the low-temperature heat capacity around 30 K, is significantly affected on one hand by the increasing concentration in thorium content and on the other hand by the radiation damage of the high powerful alpha emitter of plutonium 238 isotope. The radiation affects the long-range magnetic ordering of the U^{4+} ions, and the corresponding magnetic peak shifts to lower temperature and its amplitude decreases until it vanishes but residual heat capacity is revealed at 0 K, which we assign it to the displacements and vacancies created in the alpha radiation cascades.

The result for $(U,^{238}Pu)O_2$ can be compared to the $(U_{1-y}Am_y)O_{2-x}$ solid solution, for which we observed the absence of the antiferromagnetic transition as well as high residual and excess heat capacity at low temperature for y = 0.08 and 0.20. Considering the more complex $(U^{4+},U^{5+},Am^{3+})O_2$ composition with equimolar amounts of trivalent americium and pentavalent uranium as a result of charge transfer, the formal "dilution" is twice as high. For the sample with the highest Am concentration the extent of dilution (Am^{3+}+U^{5+}) is thus larger than the 33% found as limit beyond which the long-range magnetic ordering in the solid solution has disappeared. In that material both radiation effects and dilution must be considered.

The very regular change of the magnetic transition with addition of thorium in the system, confirms that also dilution on the cation sublattice affects the long range magnetic order of the U^{4+} ions and we conclude that when 4 out of 12 nearest neighbors are replaced, the magnetic ordering disappears.

8.3. Outlook

- **High-temperature properties**

As is the case in the present work, most studies on the heat capacity of nuclear fuels are restricted to about 1500 °C due to commercial equipment limitations. It would certainly be beneficial to extend measurements to higher temperatures that are of relevance to fuel behaviour under abnormal or accidental conditions. Recently, Pavlov *et. al* [7, 8] have reported high-temperature results of thermal conductivity, specific heat and thermal diffusivity of UO_2 and ThO_2 obtained using a laser heating technique combined with a numerical inverse method [9]. This technique could also be employed to investigate the mixed solid solutions considered in this thesis up to higher temperatures to get more insight of the role OFP formation in more complex mixed oxides. As the model suggest a smooth maximum in specific heat in the pre-melting region and molecular dynamics simulations (MD) [10] indicate an sharp anomaly that is related to diffuse Bredig transition, which is not shown by any experimental data or OFP model, this could help to get a better understanding of the sources of the discrepancies.

- **Low-temperature**

In the context of low-temperature measurements of the heat capacity of mixed actinide oxides, further investigations will help clarify aspects related to the substitution in the metal sublattice, the self-irradiation and the resulting disorder mechanism, and the possible implications for their thermodynamic properties. An area that deserves a closer look is that of the low-temperature heat capacity of strong α-emitters, such as Am. However, the substantial self-heating resulting from their high alpha activity complicates or even precludes measurements at the lowest temperatures, that may be interesting for detecting anomalous behaviour. Therefore, a more promising investigation route would be to study actinide oxide mixtures, such as $(U,Am)O_2$, $(Th,Am)O_2$, with a concentration of alpha emitter low enough to permit a measurement. Or even mixtures with some surrogates [11, 12] to learn more about the substitution and charge transfer and get the ultimate resolution of the concurring effects.

- **Atomistic calculations**

With constant advances still being made on many levels, including theory, simulation and algorithms, modeling of nuclear materials represents a promising and reliable science-based approach for nuclear fuel characterisation [10, 13, 14].

Recently, systematic investigations of the lattice parameters, elastic constants and bulk moduli, as well as mixing enthalpies of $(U,Pu)O_2$ as a function of plutonium content have been made using electronic structure calculations in the framework of the density functional theory (DFT) [15]. The calculated properties show good agreement with experimental data, whenever available, and demonstrate

Modeling and simulation are powerful tools that complement experiments by providing microscopic insights for experimental results, which ultimately lead to a deeper understanding of the underlying mechanisms for a particular phenomenon. Applying DFT to mixed actinide oxides is difficult because a mixture is a complex statistical object for which a certain chemical composition must be realized with many possible and representative atomic configurations. In the case of strong α-emitters the consequences of the interaction with crystalline materials is the formation of lattice defects resulting from the energy transfer to the atoms. The study of the effect of individual defects is still within the capabilities of DFT, but for high defect concentrations as occur in the measurement presented here, other techniques such as MD are needed.

References

[1] S. Nichenko, D. Staicu, Journal of Nuclear Materials 439 (2013) 93-98.

[2] R.V. Pai, M. Sahu, M.R. Pai, D. Jain, Jagannath, S.K. Mukerjee, Thermochimica Acta 654 (2017) 8-17.

[3] V. Saltas, A. Chroneos, M. W. D. Cooper, M.E. Fitzpatrick, F. Vallianatos, RSC Advances 6 (2016) 103641-103649.

[4] A. Bergeron, D. Manara, O. Beneš, R. Eloirdi, M.H.A. Piro, E.C. Corcoran, Journal of Nuclear Materials 512 (2018) 324-348.

[5] C.O.T. Galvin, M.W.D. Cooper, M.J.D. Rushton, R.W. Grimes, Scientific Reports 6 (2016) 36024.

[6] P.S. Ghosh, N. Kuganathan, C.O.T. Galvin, A. Arya, G.K. Dey, B.K. Dutta, R.W. Grimes, Journal of Nuclear Materials 479 (2016) 112-122.

[7] T.R. Pavlov, M.R. Wenman, L. Vlahovic, D. Robba, R.J.M. Konings, P. Van Uffelen, R.W. Grimes, Acta Materialia, 139 (2017) 138-154.

[8] T.R. Pavlov, T. Wangle, M.R. Wenman, V. Tyrpekl, L. Vlahovic, D. Robba, P. Van Uffelen, R.J.M. Konings, R.W. Grimes, Scientific Reports, 8 (2017) 1-14.

[9] T.R. Pavlov, L. Vlahovic, D. Staicu, R.J.M. Konings, M.R. Wenman, P. Van Uffelen and R.W. Grimes, Thermochim. Acta 652 (2017) 39-52.

[10] M.W.D. Cooper, M.J.D. Rushton, and R.W. Grimes, J. Phys.: Condens. Matter 26 (2014) 105401.

[11] C. Yablinsky, R. Devanathan, J. Pakarinen, J. Gan, D. Severin, C. Trautmann, T. Allen, Journal of Materials Research, 30 (2015) 1473-1484.

[12] A. Navrotsky, J. Mater. Chem., 20 (2010) 10577-10587.

[13] R. Devanathan, L. Van Brutzel, A. Chartier, C. Guéneau, A.E. Mattsson, V. Tikare, T. Bartel, T. Besmann, M. Stan, P. Van Uffelen, Energy Environ. Sci., 3 (2010) 1406-1426.

[14] M. Stan, Nucl. Eng. Technol., 41 (2009), 39-52.

[15] I. Ceik Njifon, M. Bertolus, R. Hayn, M. Freyss, Inorg. Chem. 57 (2018) 10974-10983.

Summary

The work presented in this thesis provides new data on the behaviour of the binary mixed actinide oxides of the following systems: (Th,Pu)O_2, (U,Pu)O_2, (Th,U)O_2, (U,Am)O_2. The results were obtained by performing measurements in a large temperature interval, for some compounds the thermodynamic properties were studied in the range from about 2 to 2400 K, from cryogenic to sub-melting state. The goal of the thesis was extending the knowledge of the thermophysical behaviour of the oxides containing different mixture of actinides in various ratios by performing analysis and use the results for providing and improving the foundational knowledge of such materials.

Enthalpy, heat capacity, thermal diffusivity and thermal conductivity of the investigated mixed oxides were determined. In addition, the effect of dilution and radiation damage on the magnetic transition present in uranium dioxide-based solid solutions was studied. Since most of the studied samples are highly radioactive, they were prepared in limited quantities in glove boxes, and techniques suitable for measuring thermal properties of small samples (< 100 mg) were used.

Experiments have been performed in the low- and high-temperature regimes. Heat capacity was either measured directly or indirectly by measuring the enthalpy increments using different calorimeter types. Thermal diffusivity was measured in the temperature range from 500 to 1550 K, with a laser flash instrument, and thermal conductivity was determined from this.

Chapters 2, 3 and 4 present a series of systematic high-temperature thermodynamic results relevant to the safety aspects of potential mixed oxides nuclear fuels at reactor operating temperature, as well as at higher temperatures that can occur during thermal transients in off-normal operating situations. Experiments on thermal diffusivity of (U,Am)O_{2-x} showed a strong impact of a highly radioactive material (americium) on the thermal conductivity. Enthalpy increments measurements revealed no excess heat capacity for the measured intermediate compositions of the mixed actinide oxides up to about 1800 K, while on temperatures above 2000 K the presented model predicts an excess enthalpy (heat capacity) based on the formation energetics of Oxygen Frenkel Pair in the compounds structure.

Experimental data presented in chapters 5, 6 and 7 offer new perspectives on how radioactive decay and cation substitution, both resulting in disorder on the crystal lattice, influence the low-temperature heat capacity. It was found that matrix dilution, lattice strain and radiation damage create anomalies which lead to excess contribution in the heat capacity. For temperatures below 50 K, self-irradiation has a considerable larger effect on damage creation, monopolizing the overall excess contribution, while above 50 K the excess heat capacity is assigned mainly to the Schottky anomaly and lattice strain.

Chapter 8 gives an overview of the whole thesis. Here, the reported results are discussed in an integrated way and conclusions are drawn. Considerations for extending

the research are presented.

Samenvatting

Het in dit proefschrift gepresenteerde werk heeft nieuwe gegevens opgeleverd over het gedrag van de binaire gemengde actinideoxiden voor de volgende systemen: $(Th,Pu)O_2$, $(U,Pu)O_2$, $(Th,U)O_2$, $(U,Am)O_2$. De resultaten werden verkregen door metingen uit te voeren over een groot temperatuurinterval, voor sommige verbindingen werden de thermodynamische eigenschappen bestudeerd in het bereik van ongeveer 2 tot 2400 K, van cryogene tot vlakbij de gesmolten toestand. Het doel van het proefschrift was het uitbreiden van de kennis van het thermofysische gedrag van de oxiden met verschillende mengsels van actiniden in verschillende verhoudingen door analyse uit te voeren en met de resultaten de fundamentele kennis van dergelijke materialen te verbeteren.

Enthalpie, warmtecapaciteit, thermische diffusiviteit en thermische geleidbaarheid van de onderzochte mengoxiden werden bepaald. Bovendien werd het effect van verdunning en stralingsschade op de magnetische overgang in vaste oplossingen op basis van uraniumdioxide onderzocht. Omdat de meeste onderzochte monsters zeer radioactief zijn, werden ze in beperkte hoeveelheden in handschoenkasten bereid en werden technieken gebruikt die geschikt zijn voor het meten van thermische eigenschappen van kleine monsters (<100 mg).

Er zijn experimenten uitgevoerd in het lage en hoge temperatuurbereik. Warmtecapaciteit werd ofwel direct gemeten of indirect door de enthalpie-incrementen te meten waarbij verschillende calorimetertypen werden gebruikt. Warmtediffusiviteit werd gemeten in de temperatuurbereik van 500 tot 1550 K, met een laserflitsinstrument, en thermische geleidbaarheid werd hieruit bepaald.

In hoofdstukken 2, 3 en 4 worden een reeks van hoge-temperatuur thermodynamische resultaten gepresenteerd die van belang zijn voor de veiligheidsaspecten van mogelijk mengoxide nucleaire brandstoffen bij de bedrijfstemperatuur van de reactor, maar ook bij hogere temperaturen die bij thermische transiënten bij incidenten kunnen optreden. De thermische diffusiviteitsmetingen van $(U,Am)O_{2-x}$ lieten een sterke invloed van het radioactive materiaal (americium) op de de warmtegeleiding zien. Enthalpie-increment metingen toonden geen extra soortelijke warmte voor de gemeten mengsels van de actinide oxiden tot 1800 K, terwijl voor temperaturen boven 2000 K het gepresenteerde model een extra enthalpie (soortelijke warmte) voorspelt op basis van de vormingsenergie van zuurstof Frenkel paren.

Experimentele gegevens in de hoofdstukken 5, 6 en 7 bieden nieuwe inzichten hoe radioactiviteit en kationvervanging, die beide resulteren in wanorde in de kristalrooster, de lage temperatuur warmtecapaciteit beïnvloeden. Het werd aangetoond dat matrixverdunning, roosterspanning and stralingsschade afwijkingen veroorzaken die in een extra soortelijke warmte resulteren. Voor temperaturen lager dan 50 K heeft de zelfbestraling een aanzienlijk groter effect op het onstaan van schade, en domineert de totale extra bijdrage, terwijl boven 50 K de extra soortelijke warmte voornamelijk aan

Schottky anomalieën en roosterspanning toegeschreven kan worden.

Hoofdstuk 8 geeft een samenvatting van het proefschrift. De resultaten worden in brede samenhang besproken en conclusies worden gepresenteerd. Verdere overwegingen voor vervolgonderzoek worden besproken.

Acknowledgements

As it is the year 2020, I'm looking back and reflecting on the research that was made and the effort that was put in order to complete this work. And I'm not talking only about me. I had on my shoulders the trust and the respect of people that believed that this milestone could be reached. There was a time when I was about to quit but it is thanks to all of those I'm about to mention that I did not.

I am especially indebted to my supervisor, Prof. Dr. Rudy Konings, for giving me the opportunity to work in his unit. I thank him for his assistance during the time in which I performed the scientific work as well as during the writing phase of this thesis.

I am grateful to Delft University of Technology (TU Delft) and Prof. Dr. Bert Wolterbeek for their collaboration in this PhD project.

I address very special thanks to Karin Popa for his constructive advice during my PhD and his endless encouragement. He had an essential part in the completion of this work. I am thankful to Ondrej Beneš for his guidance and help in performing the drop calorimetric measurements and the analysis of the data.

Important contribution in writing the thesis was made through many fruitful discussions that have been carried out with my good friend and colleague, Konstantinos Boboridis (Dinos), thanks a lot for all your time, support and encouragement.

During the time spent at ITU (Institute for Transuranium Elements), today known as JRC Karlsruhe, many people supported my work and me. I would like to thank all people of the former "Materials Research" unit that contributed to the successful completion of this work: Dragoș Staicu, Dario Manara, Philippe Raison, Jean-Yves Colle, Alessandro Zappia, Luka Vlahovic and Mark Sierig. Their cooperation and contribution was very important in performing all the experimental work.

A special thanks goes to Petra Strube, the secretary of the "Materials Research" unit, for her kind support and help with the administrative arrangements.

I received many useful suggestions and good advice also from my fellow colleagues: Markus Beilmann, Mike Welland, Robert Böhler, Frank de Bruycker, Petronela Gotcu, Cedric Cozzo, Marco Klipfel, Valentino Di Marcelo, Ana Smith, Raquel Jovani-Abril, Denis Bykov, Sergei Nichenko, Zeynep Talip, Elisa Capelli, Luca Capriotti, Fidelma Di Lemma, Pelin Çakir, Tsvetoslav Pavlov, Philipp Pöml, Emanuele De Bona, Daniel Freis and Roland Meier. All my appreciation for their solidarity and collaboration.

I wish to acknowledge the support of Joe Somers and his unit for providing the samples. Many thanks to Co Boshoven, Herwin Hein, Daniel Bouëxière and Rachel Eloirdi for their technical support. I am thankful also to the calorimetry group, Jean-Christophe Griveau and Eric Colineau, for their effort in measuring the samples and for their constructive comments. As well, I would like to acknowledge the scientific discussions with Roberto Caciuffo and his valuable advices.

Further, I would like to thank all my colleagues from my actual unit "Nuclear Safeguards and Forensics" of the Directorate for Nuclear Safety and Security at the

JRC Karlsruhe for their encouragement and understanding. To my head of unit, Klaus Lützenkirchen, the whole analytical service and the NDA group, a big thank you!

I am also thankful to my Romanian colleagues at the institute: Claudia Andor, Loredana Rendiuc, Magdalena Toma, Gabi Toma, Răzvan Buda, Mihaela Bragea, Andreea Panache, Steliana Popa, Monica Sela, Robert Neagoe and Radu Stanca. With you guys, Romania did not feel so far away.

All of this would not have been possible without the generous support of my family, thank you mom, dad and my dear sister! And above all, the greatest appreciation goes to the most important people in my life, to my wife Oana and our son, Vlad!

Curriculum Vitæ

Sorin-Octavian Vălu

15.05.1985 Born in Huși, Romania.

Education

2020
Ph.D. Materials Science
Technical University of Delft
Faculty of Applied Sciences

Thesis: Thermodynamic properties of the actinide oxides solid solutions
Promotor: Prof. dr. H.T. Wolterbeek
Prof. dr. R.J.M. Konings

2010
MSc.
Alexandru Ioan Cuza University of Iași, Romania
Thesis: Fuels for Molten salt type Generation IV nuclear reactors

2008
BSc.
Alexandru Ioan Cuza University of Iași, Romania
Thesis: Radiations and life

Professional experience

2014 - present
Project Assistant - Scientific/Technical
European Commission, JRC Karlsruhe Site, Germany
Directorate G - Nuclear Safety and Security

2010 - 2013
Grantholder
European Commission, Joint Research Centre
Institute for Transuranium Elements, Karlsruhe, Germany

2009 - 2010
Trainee
European Commission, Joint Research Centre
Institute for Transuranium Elements, Karlsruhe, Germany

List of Publications

10. **O.S. Vălu**, E. De Bona, K. Popa, J.-C. Griveau, E. Colineau, R.J.M. Konings, *The effect of lattice disorder on the low-temperature heat capacity of* $(U_{1-y}Th_y)O_2$ *and* ^{238}*Pu-doped* UO_2, Scientific Reports **9**, 15082 (2019).
9. **O.S. Vălu**, O. Beneš, J.-C. Griveau, E. Colineau, R.J.M. Konings, *The low-temperature heat capacity of* $(U_{1-y}Am_y)O_{2-x}$ *for y = 0.08 and 0.20.*, Journal of Nuclear Materials **507** (2018) 126-134.
8. **O.S. Vălu**, O. Beneš, D. Manara, R.J.M. Konings, M.W.D. Cooper, R.W. Grimes, C. Guéneau, *The high-temperature heat capacity of the* $(Th,U)O_2$ *and* $(U,Pu)O_2$ *solid solutions*, Journal of Nuclear Materials **484** (2017) 1-6.
7. E. Epifano, O. Beneš, **O.S. Vălu**, J. Zappey, F. Lebreton, P.M. Martin, C. Guéneau, R.J.M. Konings, *High temperature heat capacity of* $(U, Am)O_{2\pm x}$, Journal of Nuclear Materials **494** (2017) 95-102.
6. K. Popa, O. Beneš, D. Staicu, J.-C. Griveau, E. Colineau, P.E. Raison, J.-F. Vigier, G. Pagliosa, M. Sierig, **O.S. Vălu**, J. Somers, R.J.M. Konings, *Thermal properties of* $PbUO_4$ *and* Pb_3UO_6, Journal of Nuclear Materials **479** (2016) 189-194.
5. **O.S. Vălu**, O. Beneš, R.J.M. Konings, J.-C. Griveau, E. Colineau, *The low-temperature heat capacity of the* $(Th,Pu)O_2$ *solid solution*, Journal of Physics and Chemistry of Solids **86** (2015) 194-206.
4. **O.S. Vălu**, O. Beneš, R.J.M. Konings, H. Hein, *The high temperature heat capacity of the* $(Th,Pu)O_2$ *system*, Journal of Chemical Thermodynamics **68** (2014) 122-127.
3. **O.S. Vălu**, D. Staicu, O. Beneš, R.J.M. Konings, P. Lajarge, *Heat capacity, thermal conductivity and thermal diffusivity of uranium-americium mixed oxides*, Journal of Alloys and Compounds **614** (2014) 144-150.
2. O. Beneš, R.J.M. Konings, D. Sedmidubský, M. Beilmann, **O.S. Vălu**, E. Capelli, M. Salanne, S. Nichenko, *A comprehensive study of the heat capacity of CsF from T=5K to T=1400K*, Journal of Chemical Thermodynamics **57** (2013) 92-100.
1. R. Grădinaru, **O.S. Vălu**, S. Postolache, C.C. Pavel, I. Sandu and K. Popa, *On the influence of ETS-10 porosity and surface properties in retention of some nanoions and nanomolecules*, Environmental Engineering and Management Journal, **8** (2009) 901–905.

9 789463 841405